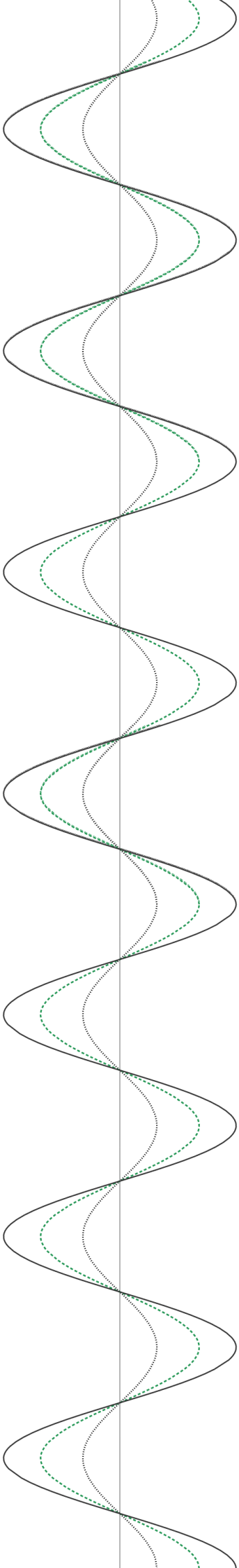

UNIVERSITY OF TWENTE.

Faculty of Engineering Technology

Extensions and simulations of numerical model for picosecond laser-material interaction in bulk sapphire

M. Huizingh

MSc. Thesis

January 28, 2021

Supervisors:
prof. dr. ir. G. R. B. E. Römer
dr. L. Capuano MSc.

Chair of Laser Processing,
Department of Mechanics of Solids,
Surfaces and Systems (MS^3),
Faculty of Engineering Technology,
University of Twente
P.O. Box 217
7500 AE Enschede
The Netherlands

Preface

I am as excited as the electrons under the influence of a high energy pulse, because my thesis is finally complete! The $82(!)$ pages seem excessive, however in Chapters 5 and 6 a lot of pages are filled with large figures, increasing the page count.

Before starting this assignment I visited several research groups, having my first meeting with G.R.B.E. Römer, on the 8th of November. I was captivated by the assignment, out of my interest for modelling (it was quite some modelling, as run time would take up to $72(!)$ hours), further exchanging emails with my soon-to-be day-to-day supervisor, L. Capuano, convinced me, starting my thesis on the 1st of March.

I got to know all about sapphire and its potential, got familiar with light theory and got to work with COMSOL Multiphysics® almost every day. Fun and frustration came together, as I attempted to implement the improvements step by step. Again learning that, selecting what is relevant is most important, as the theory seems endless, bordering quantum physics.

I would like to thank G.R.B.E. Römer and L. Capuano, for their critical thinking and support; Linda Grafen and Lars van der Woude for their friendship and support from the first to the last day at the University of Twente; special thanks to my family, who have supported me before, during and after my academic career; thanks to Niveditha Kumar for frequently reading my thesis and accompanying me during the *corona* pandemic and finally to all other people that have helped me complete my thesis.

Mark Huizingh
Enschede, January 2021

Summary

An existing numerical model for picosecond laser-material interaction in bulk sapphire consisting of four partial differential equations is summarized, providing a description of physical behavior in relation to the mathematical description. The limitations of the model are presented, selecting three features to be improved.

Firstly, the current collimated beam is modified to a focused beam, Gaussian in space and time. Secondly, boundary conditions are implemented representing interaction with the bulk material. Thirdly, convergence issues are reduced by implementing improvements in the model, mesh and solver configurations.

Several simulations are presented to analyze the effects of input parameters and interaction between phenomena of the improved model. Classified in three groups: low pulse energy, heating the material, high pulse energy, generating plasma causing a complex interaction of phenomena, and higher pulse energy, showing stronger behavior and time extended study results.

An addition to the model is the implementation of thermal stress. The temperature output from the simulations are used to determine material expansion and resulting stress in separate studies to predict crack formation observed during experiments.

The improvements and extension of the model was successful in describing subsurface laser-sapphire interaction and stress concentrations. An improved understanding of model behaviour and the significance of each variable and phenomena was identified. Furthermore, recommendations are given to improve model accuracy. The inclusion of electromagnetic or wave optics, plasma physics for high pulse energy modelling and the implementation of accurate material parameters are the next steps leading to a comprehensive model for laser-sapphire interaction.

Contents

List of abbreviations

HF	Hydrofluoric
PDE	Partial differential equation
FWHM	Full Width Half Maximum
VB	Valence band
CB	Conduction band
PK2	Second Piola-Kirchhoff
w.r.t.	with respect to

Nomenclature

Roman symbols I

Symbol	Description	Unit
$\mathcal{B}$	Magnetic flux density vector	Wb/m^2
c	Speed of light in sapphire	m/s
c_0	Speed of light vacuum	m/s
C_p	Heat capacity	J/K
$\boldsymbol{C}$	Elasticity tensor	Pa
d	Layer thickness	m
$\mathcal{D}$	Electric flux density vector	C/m^2
e	Electron charge ($1.60217662 \cdot 10^{-19}$)	C
E	Young's modulus	GPa
E_g	Band gap energy	J
E_{ph}	Photon energy	J
E_p	Pulse energy	J
$\mathcal{E}$	Electric field vector	V/m
$\boldsymbol{F}$	Volume forces	N
G_{TTM}	Electron-phonon coupling coefficient	W/m^3 K
h	Planck constant ($6.62607004 \cdot 10^{-34}$)	m^{2}kg/s
$\mathcal{H}$	Magnetic field vector	A/m
I	Intensity	W/m^2
k	Thermal conductivity	W/mK
k_b	Boltzmann constant	m^{2}kg/s^{2}K
k_0	Reference wave number	1/m
K_e	Electron-thermal diffusion coefficient	W/m K
m_e^*	Effective electron mass	kg
$\mathcal{M}$	Magnetization density vector	A/m
n	Refractive index sapphire	-
n_{at}	Initial VBelectron density	1/m^3
n_e	CB electron density	1/m^3
n_{e_init}	Initial CB electron density	1/m^3
$N_{0,1,tot}$	Free, bounded and total electron density	1/m^3
P	Power	W
$\mathcal{P}$	Electric polarization density vector	C/m^2
$\boldsymbol{S}$	Second Piola-Kirchhoff (PK2) stress tensor	Pa
$\mathcal{S}$	Poynting vector	W/m^2

Roman symbols II

Symbol	Description	Unit
T_e	Free electron temperature	K
T_l	Lattice temperature	K
T_{ref}	Volume reference temperature	K
T_{tl}	Initial layer temperature	K
T_0	Initial temperature	K
$\boldsymbol{u}$	Displacement field vector	m
w_0	Beam waist	m
W_{mpi}	Multiphoton ionization production rate	1/m^{3}s
W_{pi}	Keldysh ionization production rate	1/m^{3}s
z_f	Focal point	m
z_R	Rayleigh length	m

Greek symbols I

Symbol	Description	Unit
α	Thermal expansion coefficient	1/K
γ	Damping factor	-
ϵ	Strain	-
ϵ	Electric permittivity of sapphire	F/m
ϵ_0	Vacuum permittivity ($8.854187817 \cdot 10^{12}$)	F/m
$\boldsymbol{\epsilon}$	Strain tensor	-
ϵ_∞	High frequency permittivity	F/m
θ	Beam divergence	rad
κ	Electric-polarization field coupling factor	1/m^3
λ	Wavelength	m
μ	Magnetic permeability of sapphire	H/m
μ_e	Electron mobility	m^2/V s
μ_0	Vacuum magnetic permeability ($1.256637061 \cdot 10^{-6}$)	H/m
ν	Poisson's ratio	-
ρ	Density	kg/m^3
σ	Standard Deviation	s
σ_{ab}	Free electron cross-section	m^2
$\sigma_{t,c,f}$	Tensile, compressive and flexural strength	Pa
$\boldsymbol{\sigma}$	Stress tensor	Pa

Greek symbols II

Symbol	Description	Unit
τ_c	Mean electron collision time	s
τ_{rec}	Recombination time	s
τ_{rel}	Electron-lattice relaxation time	s
$\chi_{e,m}$	Electric and magnetic susceptibility	-
ω	Frequency of light	rad/s
$\omega_{p,0}$	Plasma and resonance frequency	rad/s

Math operations

Symbol	Description
$\frac{d}{dx}, \frac{\partial}{\partial x}$	Derivative and partial derivative w.r.t. x
$\int_a^b f(x)dx$	Integral w.r.t. x
∇	Differential operator
$\nabla\cdot$	Divergence
$\nabla\times$	Curl
$\mid x \mid$	Absolute value of x
:	Double-dot product

Chapter 1

Introduction

1.1 Background

Synthetic sapphire has been produced for over a century, relatively cheap and with low environmental impact, using a range of crystal growth methods [1]. Crystalline sapphire is considered a high performance and durable material, even under extreme conditions, due to high chemical inertness, corrosion and radiation resistance. It is one of the hardest materials and has a higher biocompatibility than metals and polymers. These unique properties result in usage for a wide range of applications, e.g. light emitting diodes (LEDs), optical waveguides, microfluidic devices and medical implants [2–4].

Several of these applications rely on micro-machining to fabricate small features, for which a number of techniques are available. Abrasive jet machining or powder blasting is a low cost, high speed etch technique for brittle materials, such as glass and sapphire. Furthermore, mechanical micro-machining uses conventional tools to mill and drill surface features, yet both techniques are limited by micrometer feature size [5]. Photolithography, the most used lithography technique, uses ultraviolet (UV) light to generate surface patterns onto a substrate up to nanometer feature size, yet is a complex, multistep process [6–8].

A two-step manufacturing process consisting of laser irradiation and subsequent selective etching, see Figure 1.1, is promising for precision manufacturing of sapphire components [5,9]. Due to absorption of ultrashort laser pulses (in the pico- to femtosecond timescale) laser micro-machining of transparent materials, like sapphire, is possible. The laser radiation amorphizes the crystalline sapphire, see Figure 1.2, modifying micro- and nanosized regions on or below the surface, allowing for fabrication of complex structures in the bulk material.

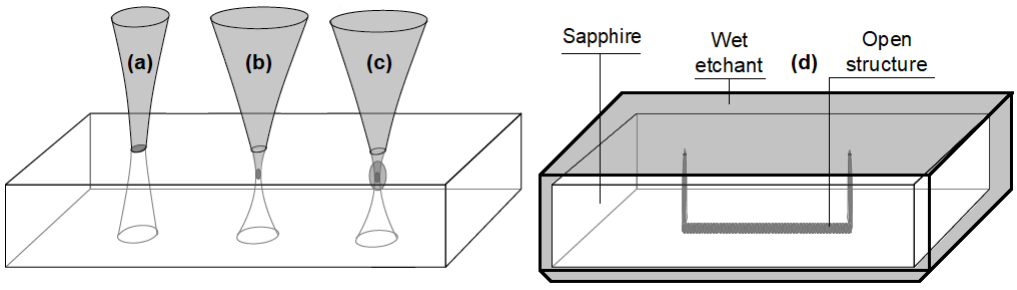

Figure 1.1: Two-step manufacturing process: Laser surface (a), subsurface (b) or extended volume (c) irradiation, followed by chemical etching (d) of the amorphous sapphire (adapted from [10,11]).

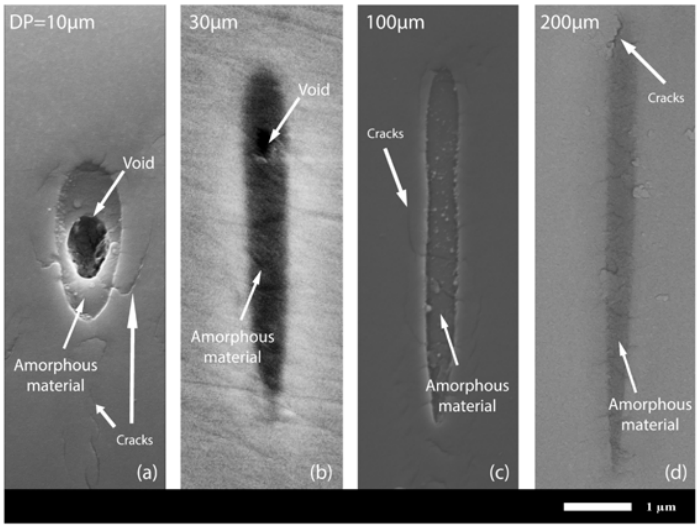

Figure 1.2: Typical subsurface modifications showing the amorphous material, voids and cracks post-laser processing (DP = depth of processing) [12].

The amorphous sapphire can be removed using selective etching, such as hydrofluoric (HF) etching, as the etch rate of amorphous sapphire is extremely high (10^5) compared to crystalline sapphire, see Figure 1.4 [11–14].

The interaction between the laser and material is complex due to a variety of process parameters and occurrence of nonlinear phenomena at different timescales. A numerical model of the phenomena increases understanding of the process and allows for efficient, cost-effective optimization of the manufacturing technique [9,15].

Sundaram and Mazur [16] have identified and divided the different phenomena of laser-material interaction into four major categories: 1) electron excitation, 2) thermalization, 3) electron removal and 4) thermal and structural effects, see Figure 1.3. Within these categories different processes take place simultaneously or in sequence, i.e. photoionization, electron ionization, electron recombination, electron-electron and electron-phonon interaction, and electron and thermal diffusion.

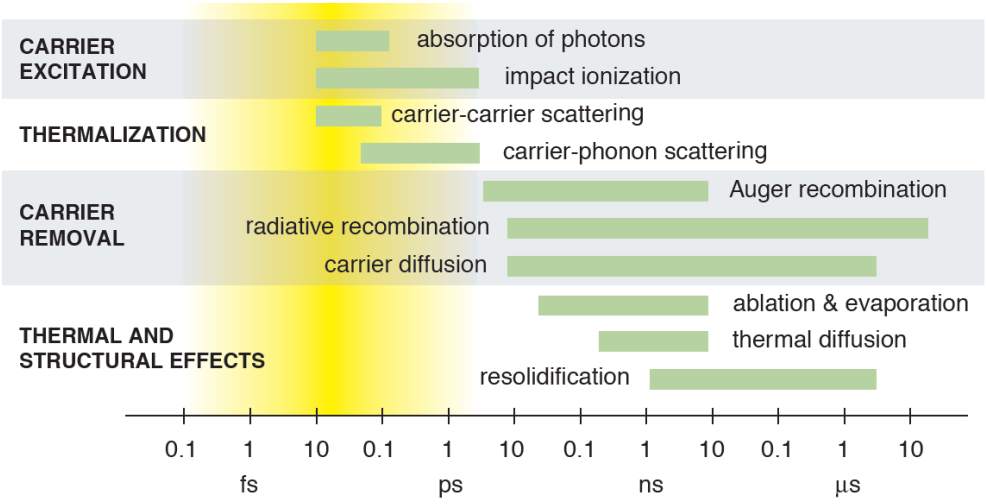

Figure 1.3: Overview of laser-material interaction phenomena and relevant timescales [16].

Several studies [15,17–20] have attempted to simulate these processes and create a comprehensive numerical model studying ultrashort laser processing. A first model suitable for sapphire was presented by Capuano, de Zeeuw and Römer [21], implemented in COMSOL Multiphysics®, used to simulate a number of cases with various input parameters.

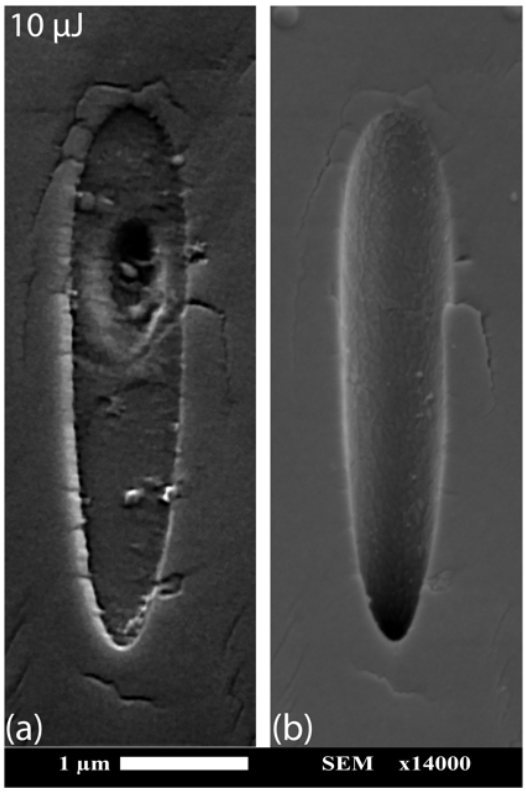

Figure 1.4: Subsurface structure in crystalline sapphire before (a) and after (b) HF etching [12].

1.2 Problem definition

Several aspects of the model by Capuano et al. [21] need to be developed further, based on various suggestions by de Zeeuw [22]. Firstly, the equations, assumptions and recommendations are reevaluated to select improvements that result in a more comprehensive model. Therefore, in this thesis, after an accurate review of options for improvement and expansion of the base model (see Section 2.4), the following primary objectives are defined:

1. Improve existing model through removing assumptions, by implementing a focusing laser beam profile, instead of a collimated laser beam and proper boundary conditions;

2. Run several simulation scenarios using the improved model, in order to study the influence of parameters, i.e. pulse energy, on the interaction of phenomena occurring during laser-material interaction;

3. Extend the model by adding thermally induced stress calculations. That is, due to observations in experimental studies [12,13,23] consistently show cracking due to laser irradiation in the picosecond regime, see Figure 1.5.

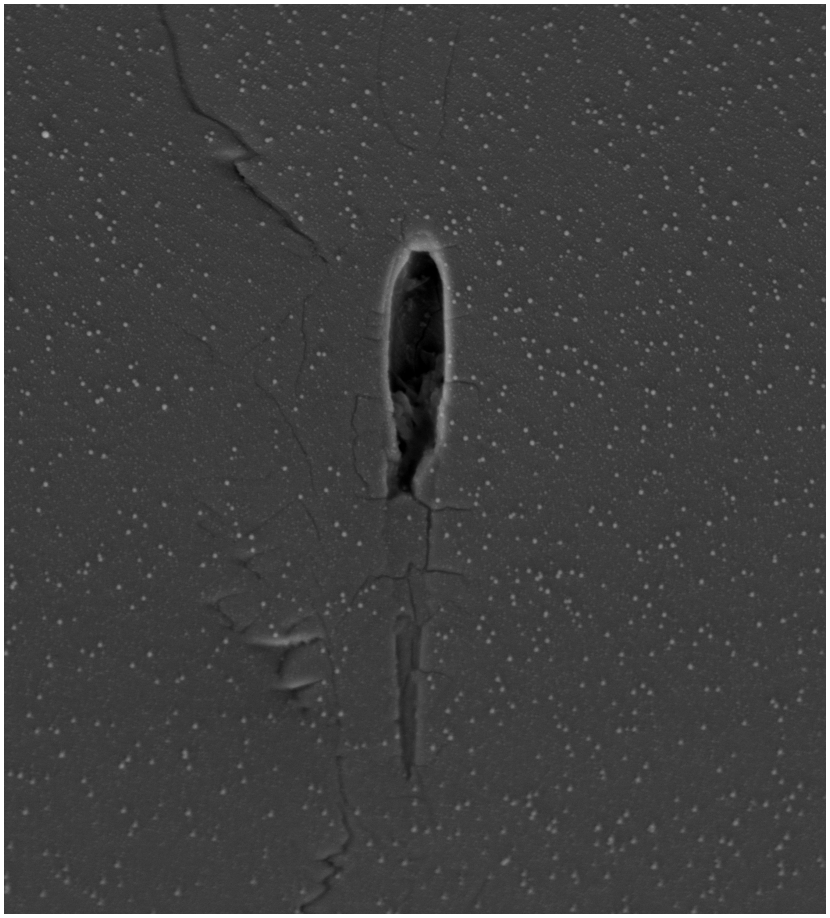

Figure 1.5: Cracks in crystalline sapphire surrounding the amorphized region.

The secondary objective of this thesis is resolving convergence problems of the model. The existing model of de Zeeuw [22] has failed to converge under certain simulation conditions, attributed to steep gradients and approaching critical numerical values of variables.

1.3 Structure of thesis

In Chapter 2 the model as developed by de Zeeuw and Capuano et al. [21,22] is presented briefly. That is, a description to clarify the material assumptions, a summary of the physical and mathematical description of the laser-sapphire behaviour, followed by the identification of the limitations of the model and the selection of the steps for improvement, as briefly mentioned in Section 1.2. This is followed by Chapter 3, which will discuss the theoretical framework of the selected improvements. Chapter 4 describes the implementation in COMSOL Multiphysics®. In Chapter 5 the results of several simulation scenarios of the improved model are given and discussed, describing model behaviour. The results of stress modelling are presented and discussed in Chapter 6, as it is a separate extension of the model. Finally, Chapter 7 draws conclusions and provides suggestions for future work.

The total number of pages in this thesis is excessive due to several pages of Chapter 5 and 6 containing only figures and graphs.

Chapter 2

Base model of laser-sapphire interaction

2.1 Introduction

The model presented by Capuano, de Zeeuw and Römer [21] describes, for isotropic sapphire, the laser-material interaction in a 2D axisymmetric domain via a system of equations, allowing for numerical calculations. The system is a set of four Partial Differential Equations (PDEs), implemented in COMSOL Multiphysics® [22,24] and determines the (local) material response of sapphire to a single, high intensity laser pulse.

Firstly, the assumptions leading to an isotropic material made by de Zeeuw [22] are rigorous yet unclear, therefore in Section 2.2 the implemented simplifications are clarified. Secondly, an overview of the laser-sapphire interaction is given, presenting the PDEs and describing the physical phenomena expressed by each equation. The physical interpretation of each term is summarized, stating the implemented frameworks, as further details are found in de Zeeuw [22]. Finally, the limitations of the model are discussed, selecting several for improvement in this thesis.

2.2 Sapphire

Crystalline sapphire (α-Al_2O_3) is the bulk material considered for laser processing, as the simplification by de Zeeuw [22] are not elaborated upon, recapitulation is appropriate.

A single sapphire crystal consists of Al^{3+} and O^{2-} ions arranged as a rhombohedron, forming a hexagonal crystal lattice, see Figures 2.1a and 2.1b. The crystalline field has no symmetric center due to crystal lattice distortions, consequently crystallographic planes are defined to determine properties of the bulk material, see Figures 2.1c and 2.1d.

Table 2.1: Mechanical parameters of sapphire.

Symbol	Description	Value	Unit	Source
ρ	Density	3970	kg/m^3	[2,25]
HV	Hardness Vickers	16–22.5	GPa	[2,25]
E	Young's Modulus	345–470	GPa	[2,25]
σ_t	Tensile strength	0.4–2.25	GPa	[2,25]
σ_c	Compressive strength	2–2.94	GPa	[2,25]
σ_f	Flexural strength	0.69–1.54	GPa	[2,25]
ν	Poisson's ratio	0.27–0.30	-	[2]

The crystalline bulk material is characterized parallel and perpendicular to the C-axis, where directional differences in parametric values are 10 to 20%. However, suppliers offer a wider range of values for mechanical properties, see Table 2.1. Nevertheless, for processing anisotropy is neglected, assuming isotropy for the optical, electrical and thermal parameters relevant to laser-sapphire interaction.

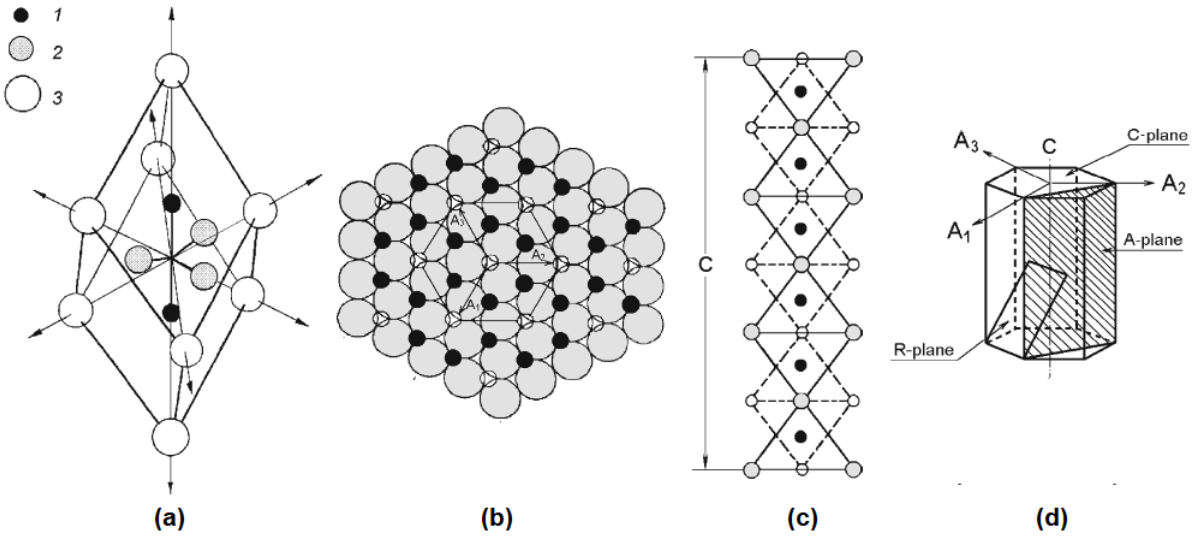

Figure 2.1: Crystal structure sapphire: single crystals (a) containing Al^{3+} (black), O^{2-} (grey) ions and octahedral holes (white) arrange in hexagonal cells, shown schematically in the basal plane (b) and along the C-axis perpendicular to the plane (c) shows the location of the main crystallographic places (d) in relation to the ions (adapted from [2]).

2.3 Overview laser-sapphire interaction

The model of de Zeeuw [22] consists of four PDEs, using the following variables, as the mathematical description of the laser-sapphire interaction:

1. Intensity (I), describing the propagation of the laser pulse energy;
2. Free electron density (n_e), describing the (local) production rate of free electrons;
3. Free electron temperature (T_e), describing the total kinetic energy of free electrons;
4. Lattice temperature (T_l), describing the classical material temperature.

These quantities determine the numerical values of terms in other PDEs, leading to a complex network of interaction, see Figure 2.2. As each of the four terms affects one or more physical phenomena occurring in the material (solid lines), the phenomena subsequently affect one or more of the variables (dashed lines).

The incident laser pulse description determines the intensity profile and consequent excitation of electrons, known as (charge) carriers, in the electron cloud of the Al^{3+} and O^{2-} ions. The physical phenomena and their effects occur on various timescales, see Figure 1.3, divided into four major regimes. The mathematical and physical description of the laser pulse, four PDEs and interaction phenomena presented briefly, for full details refer to de Zeeuw and Capuano et al. [21,22].

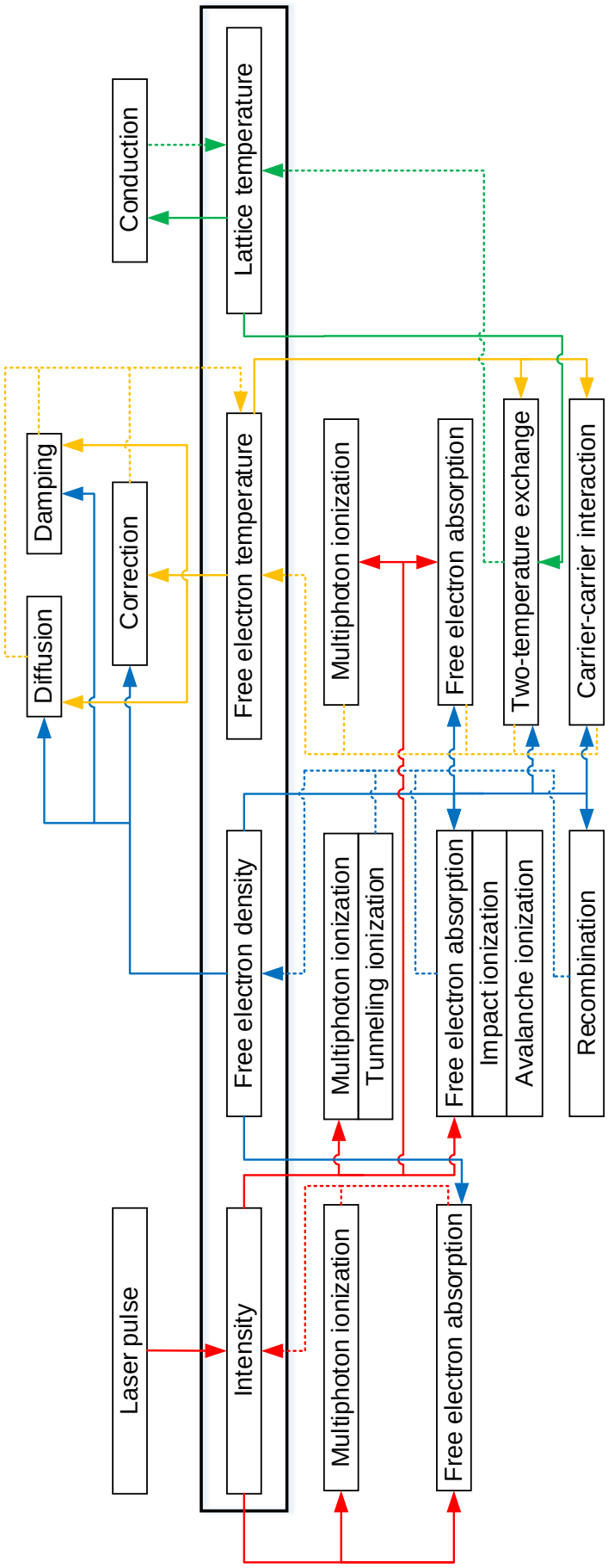

Figure 2.2: Base model relations and variable interaction.

2.3.1 Laser pulse configuration and propagation

The properties of a laser beam, related to the electromagnetic wave phenomenon, allow for focusing of the beam. When combined with ultrashort pulse times and high pulse energy, described by the temporal and spatial pulse profile respectively, high intensities are obtained in the focal point [26,27].

The temporal power profile describes the pulse power in time, dependent on the pulse energy (E_p) and pulse time (t_p). Commonly for lasing sources the temporal profile of a pulse is Gaussian, see Figure 2.3, giving the power output as a function of time [28]. The pulse time is defined as the time between 50% of the maximum power before and after the peak of the pulse ($t = 0$), known as the Full Width Half Maximum (FWHM) pulse time.

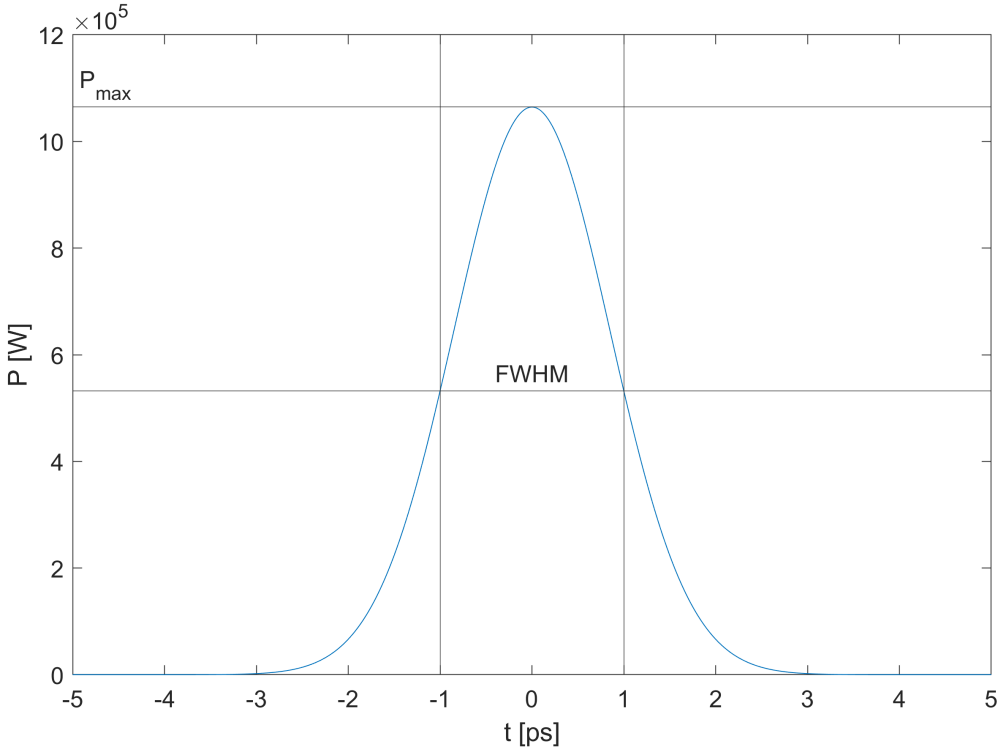

Figure 2.3: Example of typical Gaussian temporal ultra short laser pulse for processing sapphire, (FWHM) pulse time (t_p) is 2[ps].

The temporal power profile is determined using the following equations [29]:

$$P(t) = \frac{E_p}{\sigma\sqrt{2\pi}}\exp\left[-\left(\frac{t}{\sqrt{2}\sigma}\right)^2\right], \tag{2.1}$$

where

$$\sigma = \frac{t_p}{2\sqrt{2\ln(2)}}, \tag{2.2}$$

is the standard deviation of the pulse time.

Typically, in laser processing of sapphire, the power density distribution or spatial profile is also Gaussian, see Figure 2.4. Here, the intensity distribution at the focal plane, is defined

as [30]:

$$I_0(r,t) = \frac{2P(t)}{\pi w_0^2}\exp\left[-\left(\frac{r}{w_0^2}\right)^2\right], \tag{2.3}$$

where w_0 and r are the beam waist and the radial coordinate respectively, describing the incident pulse energy for the model and $P(t)$ is the temporal power profile.

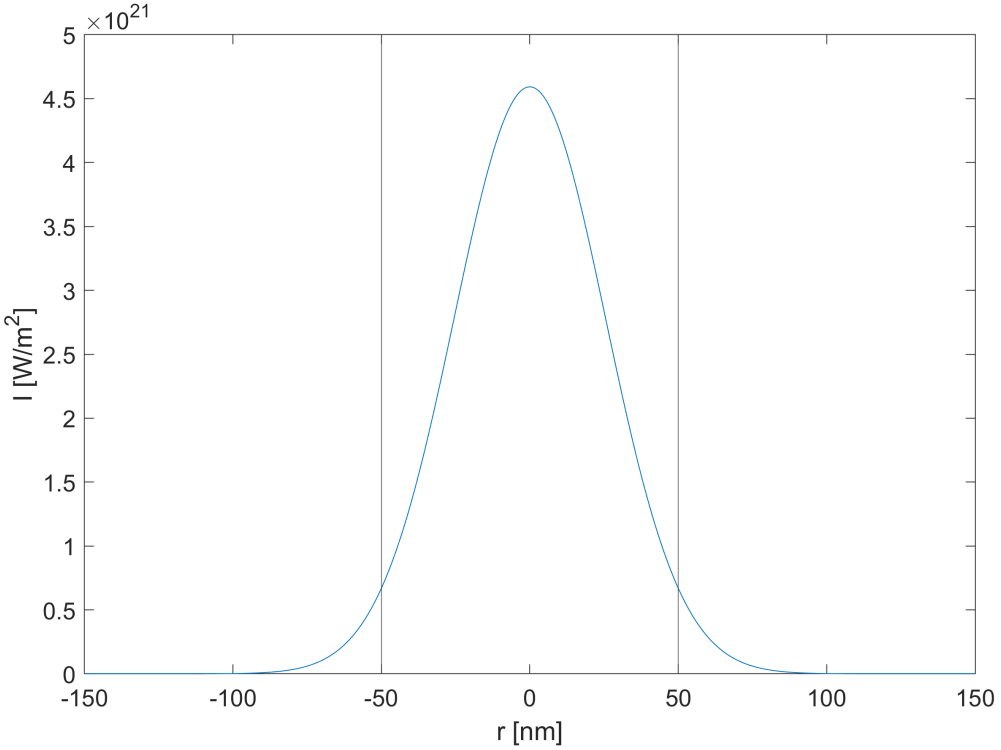

Figure 2.4: Example of typical Gaussian spatial laser pulse profile for processing sapphire, beam waist (w_0) is 100[nm].

In the model the temporal and spatial profile are implemented as a boundary condition at the top surface of the domain. The pulse propagation throughout the domain is calculated as a spatial derivative w.r.t. z, the propagation direction [21,22]:

$$\frac{\partial I}{\partial z} = -L_{mpi}(I) - L_{abs}(I, n_e), \tag{2.4}$$

where, depending on the (local) intensity and free electron density, the pulse energy is absorbed through multiphoton ionization (L_{mpi}) and free electron absorption (L_{abs}), explained in Section 2.3.2, expressed as two loss terms, see Section 2.3.5 for the full expressions.

2.3.2 Free electron density

The absorption of pulse energy generates free electrons, resulting in a free electron density. However, before excitation the electrons are in an initial configuration. The simplification to a discrete atomic band structure, see Figure 2.5, is deemed sufficient to describe electron behaviour, as the complete electron configuration is complex. The simplified structure consists of an outer and inner energy band, known as the valence band (VB) and conduction band (CB), governing the material response and interaction properties [31].

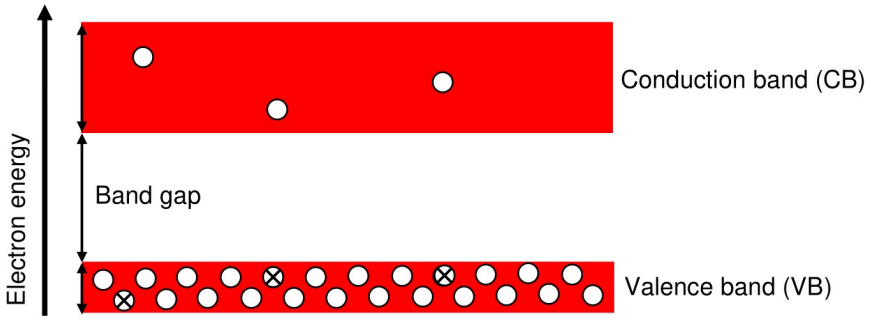

Figure 2.5: Simplified energy band structure, electrons (◯) occupy the bands, leaving holes (⊗) after excitation (adapted from [31]).

When sufficiently excited, electrons from the VB are promoted to the CB, crossing the energy gap, known as the band gap, become free electrons, able to move freely through the material. An electron cannot obtain an energy level which is in the band gap, therefore it is also known as the forbidden band.

The promoted electron leaves a hole (or empty state) in the VB, available for a low energy electron. Holes, albeit not physical particles, represent empty states as a positive charge, frequently used to significantly simplify the density states in bands [31].

The density states and electron behaviour in the model is dependent on the intensity and existing free electron density. The free electron generation and relaxation is determined using the following equation [21,22]:

$$\frac{\partial n_e}{\partial t} = P_{pi}(I) + P_{abs}(I, n_e) - L_{rec}(n_e), \tag{2.5}$$

where two production terms on the right hand side promote free electrons, the first (P_{pi}) via multiphoton and tunneling ionization and the second (P_{abs}) via free electron absorption, in conjunction with impact and avalanche ionization. The loss term (L_{rec}) reduces the free electron density by means of Auger recombination, i.e. recombination of an electron and hole, see Section 2.3.5 for the full expressions.

Single, multiphoton and tunneling ionization

Single- and multiphoton ionization, see Figures 2.7a and 2.7b, is the absorption of photon energy by a low energy electron, promoting the electron and ionizing the material. For certain wavelengths sapphire is transparent for incident light, requiring multiple photons to promote an electron to the CB. At high intensities multiphoton ionization is triggered. That is, electrons are excited to occupy an intermediate energy state, e.g. provided by doping (intentional introduction of impurities), from which they are further promoted to the CB [32].

Additionally, high intensity distorts the band structure of atoms and molecules, reducing the size of the band gap. This leads to the VB and CB to overlap, enabling tunneling ionization, meaning the electrons are free to move from the VB to the CB without gaining kinetic energy, increasing the free electron density.

The so-called Keldysh ionization framework [33] can be used to mathematically describe multiphoton and tunneling ionization behaviour in a single term (P_{pi}) at the right hand side of Equation (2.5), generating free electrons, see Figure 2.6. At low intensity multiphoton ionization is dominant, prior to the transition period between $1.5{\cdot}10^{16}$[W/m^2] and $6{\cdot}10^{16}$[W/m^2], over which tunneling ionization is dominant and multiphoton ionization diminishes.

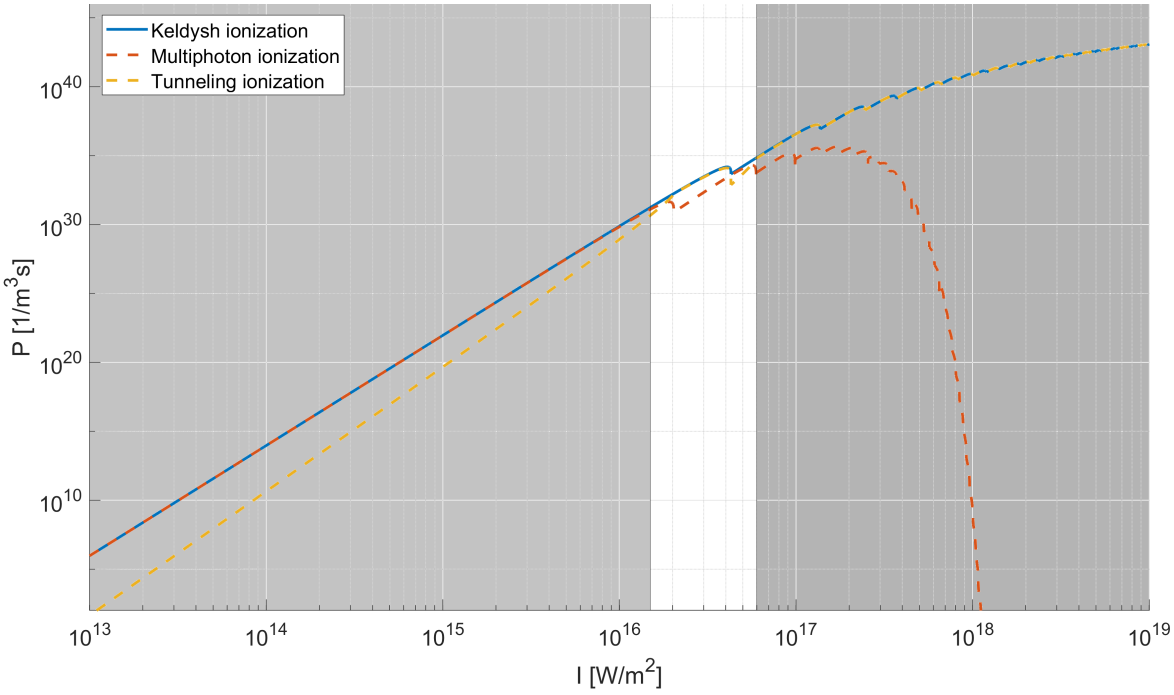

Figure 2.6: Keldysh ionization (solid line), describing multiphoton ionization behaviour (light grey region), before transitioning to tunneling ionization behaviour (dark grey region) [22].

Free electron absorption, impact and avalanche ionization

Free electron absorption, see Figure 2.7c, is a consequence of initial electron excitation, the free electrons absorb the incoming photons, gaining additional kinetic energy. High energy free electrons have an increased probability of exchanging energy with bounded electrons in the VB, leading to impact and subsequent avalanche ionization, see Figure 2.8.

High energy free electrons scatter through the material, where interaction, known as collisions or impact ionization, see Figure 2.7d, with bonded electrons in the VB can occur. Sufficient energy is exchanged to promote the bonded electron to the CB, creating an electron-hole pair reducing the high energy electrons kinetic energy, i.e. the reduction of free electron temperature.

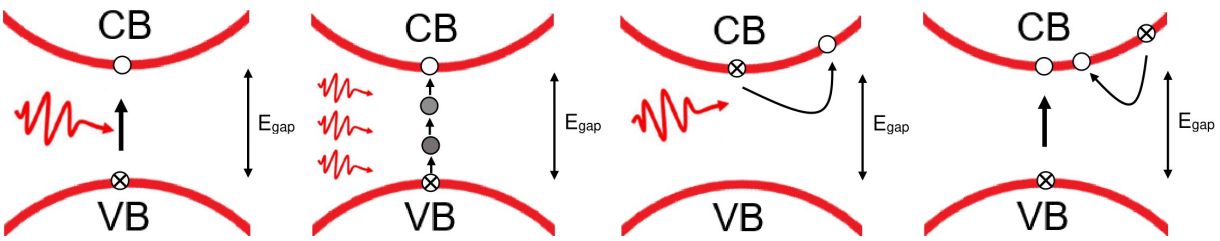

(a) Single photon ionization. *(b)* Multi-photon ionization. *(c)* Free electron absorption. *(d)* Impact ionization.

Figure 2.7: Electron excitation processes, promoting a single electron from the valence band to the conduction band (adopted from [32]).

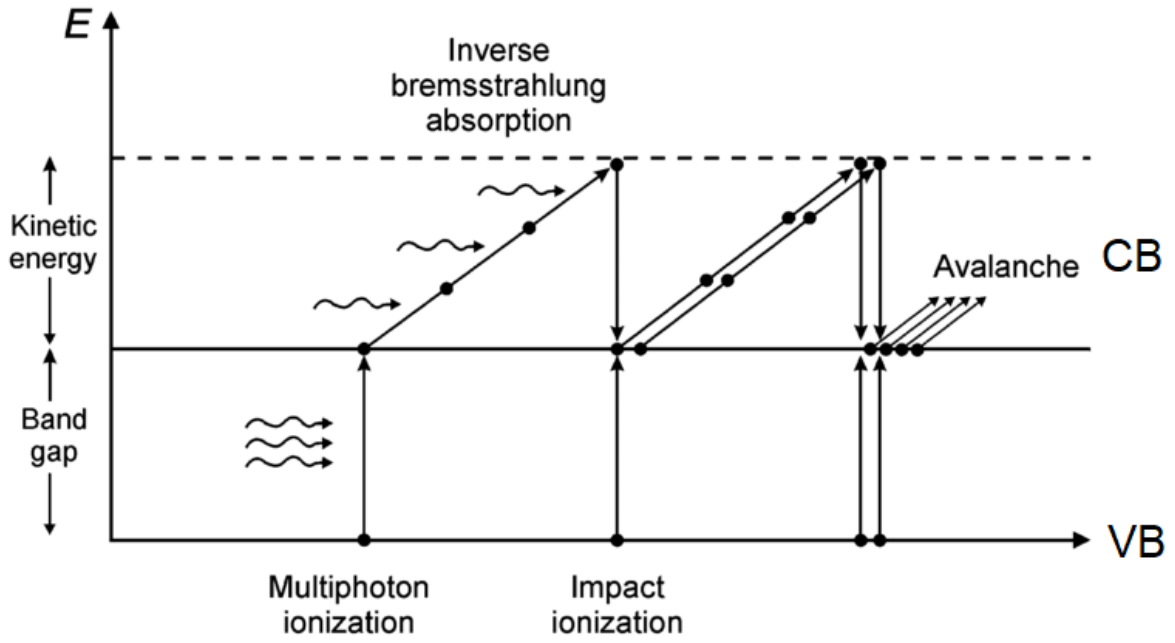

Figure 2.8: Multi-photon ionization promoting the initial electron, gaining kinetic energy through free electron absorption (known as inverse Bremsstrahlung), causing initial impact events resulting in avalanche ionization (adopted from [34]).

As more electrons are promoted, more photons are absorbed by free electrons, leading to more impact events. The production rate of free electrons, due to collisions with bounded electrons in the VB, increases significantly and becomes the dominating effect of electron generation, known as avalanche ionization [32].

The Drude model [35] is implemented in the model, due to applicability for various processing conditions and availability of the required material parameters, using a single term (P_{abs}) at the right hand side of Equation (2.5). At low intensity and free electron density it describes free electron absorption, yet when free electron density increase, the mean electron collision time decreases, inducing impact and subsequent avalanche ionization, rapidly promoting electrons to the CB.

Auger recombination

The loss term (L_{rec}) in Equation (2.5) is Auger recombination, a non-radiative process reducing the free electron density by recombination of an electron and a hole. As a result, the kinetic energy difference between the recombined electron and hole is transferred to an other free electron in the CB, the inverse process of impact ionization, see Figure 2.7d. The occurrences of recombination events increases with increasing free electron density, dependent on the mean recombination time of the medium, assumed to be constant [16].

2.3.3 Free electron temperature

The total kinetic energy of the free electron is described by the free electron temperature, dependent on all four variables (I,n_e,T_e,T_l):

$$d_a \frac{\partial T_e}{\partial t} + \nabla \cdot (-K_e \nabla T_e) = S_{mpi}(I) + S_{abs}(I, n_e) - L_{TTM}(T_e, T_l) - CC(n_e, T_e) + C(n_e, T_e), \tag{2.6}$$

where the two source terms (S_{mpi},S_{abs}) are equivalent to the loss terms of Equation (2.4), explained in Section 2.3.2. The loss term (L_{TTM}) describes carrier-phonon collisions, corresponding with the source term of Equation (2.7). The other terms are the internal effects of damping ($d_a \frac{\partial T_e}{\partial t}$), diffusion ($\nabla \cdot (-K_e \nabla)$) and carrier-carrier collisions (CC), plus an axisymmetry correction term (C) explained below. See Section 2.3.5 for the full expressions.

Carrier-phonon interaction

The loss term (L_{TTM}) of carrier-phonon interaction transfers energy from the free electrons to the lattice of sapphire. That is, collisions between free electrons and phonons, a quantum mechanical description of vibrational motion of the lattice, dissipates kinetic energy into the medium.

The transfer of thermal energy is assumed to occur according to the classical Fourier law, validated due to the duration of temperature increase as compared to the relaxation time of free electrons. Accordingly a well known two-temperature model is implemented, dependent on the free electron and lattice temperature, connected by the carrier-phonon coupling coefficient [16,27,36].

Damping, diffusion, carrier-carrier interaction and correction

During and after excitation of electrons, the electron temperature varies throughout the medium. The damping term ($d_a \frac{\partial T_e}{\partial t}$) in Equation (2.6) determines the change in (local) electron temperature, depending on the electron heat capacity [20].

The electron temperature diffusion ($\nabla \cdot (-K_e \nabla T_e)$) redistributes the free electron temperature throughout the domain. That is, free electrons exchange energy induced by carrier-carrier interaction, redistributing the free electron temperature evenly, by diffusing kinetic energy from more to less excited regions, known as electron-thermal diffusion. As the free electron density increases additional carrier-carrier interaction (CC) are prevalent, forcing the shape of the energy distribution towards a Maxwellian distribution to achieve (local) equilibrium [20,37].

A supplementary term (C) in Equation (2.6) is implemented to account for two dimensional axisymmetry. The Coefficient Form PDE module used in COMSOL Multiphysics® solves for three dimensional heat conduction, the full derivation of the correction term can be found in de Zeeuw [22].

2.3.4 Lattice temperature

The lattice temperature is described according to the classical heat equation:

$$\rho C_p \frac{\partial T}{\partial t} + \nabla \cdot (-K_l \nabla T_l) = S_{TTM}(T_e, T_l), \tag{2.7}$$

where the source term is carrier-phonon interaction (S_{TTM}), see Section 2.3.3. The damping term ($\rho C_p \frac{\partial T}{\partial t}$) in Equation (2.7) is similar to damping in Equation (2.6), dependent on the heat capacity of the medium. Furthermore, heat conduction ($\nabla \cdot (-K_l \nabla T_l)$) due to temperature differences in the domain is dependent on the thermal conductivity of the material, assumed constant, see Section 2.3.5 for the full expressions.

2.3.5 Base model equations

The full expression and relevant parameters for each term discussed above are given:

From Equations (2.4) and (2.6) the multiphoton absorption:

$$L_{mpi}(I) = -S_{mpi}(I) = 8W_{mpi}(I)E_{ph}, \quad E_{ph} = \frac{hc_0}{\lambda}, \tag{2.8}$$

where the absorption is determined by the production rate according to the multiphoton ionization of the Keldysh framework (W_{mpi}), see Figure 2.6. Promoting an electron to the CB requires 8 photons, where the photon energy is determined by the Planck constant (h), speed of light in vacuum (c_0) and the wavelength (λ) of the photon.

From Equations (2.4) and (2.6) free electron absorption, impact and avalanche ionization:

$$L_{abs}(I, n_e) = -S_{abs}(I, n_e) = \sigma_{ab} n_e I, \tag{2.9}$$

where the absorption according to the Drude model is determined by the free electron cross-section (σ_{ab}), the (local) free electron density (n_e) and (local) intensity (I).

From Equation (2.5) tunneling and multiphoton ionization, described using the Keldysh framework:

$$P_{pi}(I) = W_{pi}(I), \tag{2.10}$$

a production term, dependent on the (local) intensity (I).

From Equation (2.5) the term generating free electron via free electron absorption, impact and avalanche ionization:

$$P_{abs}(I, n_e) = \sigma_{ab} I \frac{n_e}{E_g}, \quad \sigma_{dr} = \frac{e^2}{c_0 \epsilon_0 n m_e^*} \frac{\tau_c}{1 + \omega^2 \tau_c^2}, \quad \tau_c = \frac{16\pi\epsilon_0^2 \sqrt{m_e^*(0.1E_g)^3}}{\sqrt{2} e^4 n_e}, \tag{2.11}$$

where the band gap energy (E_g) and the absorption cross-section (σ_{ab}), of which the most important parameter is the mean electron collision time (τ_c), describe production dependent on the (local) intensity (I) and free electron density (n_e). Furthermore, the absorption cross-section and mean electron collision time depend on the elementary charge (e), free space permittivity (ϵ_0), refractive index (n), effective electron mass (m_e^*) and frequency of light (ω).

From Equation (2.5) the free electron relaxation:

$$L_{rec}(n_e) = \frac{n_e - n_{e,init}}{\tau_{rec}}, \tag{2.12}$$

depending on the initial free electron density ($n_{e,init}$), (local) free electron density (n_e) during and post-processing and recombination time (τ_{rec}).

From Equations (2.6) and (2.7) the two-temperature exchange:

$$L_{TTM}(T_e, T_l) = -S_{TTM}(T_e, T_l) = G_{TTM}(T_e - T_l), \quad G_{TTM} = \frac{\frac{3}{2} k_b n_e}{\tau_{rel}}, \tag{2.13}$$

where the free electron temperature (T_e) and lattice temperature (T_l) exchange energy according to the electron-phonon coupling coefficient (G_{TTM}), dependent on the Boltzmann constant (k_b) and electron-lattice relaxation time (τ_{rel}).

For the carrier-carrier interaction term, from Equation (2.6):

$$CC(n_e, T_e) = \frac{\partial n_e}{\partial t}(E_g + \frac{3}{2}k_b T_e), \tag{2.14}$$

all parameters have been mentioned above.

The correction term from Equation (2.6):

$$C(n_e, T_e) = \frac{1}{r}K_e\frac{\partial T_e}{\partial r}, \quad K_e = \frac{2k_b^2 T_e n_e \mu_e}{e}, \tag{2.15}$$

where the radial coordinate (r), (local) free electron temperature (T_e) and the electron-thermal diffusion coefficient (K_e), depending on above mentioned parameters and the electron mobility (μ_e), correct the PDE for assuming axisymmetry.

2.4 Limitations and selected improvements

It was concluded by de Zeeuw [22] that overall the base model and study results are in agreement with experiments. However, convergence issues are to be resolved and limitations of the model are to be reduced, giving several suggestions for improvement:

1. Better estimation of free electron absorption coefficient. That is because the current coefficient is an assumption to prevent negative free electron temperatures;
2. Limit the amount of electrons available for promotion from the VB to the CB to prevent non-physical behaviour, as the electron density surpasses the amount of electrons available in the VB;
3. Implement a denser mesh of the calculation grid and/or higher order elements to prevent numerical convergence errors, which lead to the simulation failing to complete due to the inability of solving steep gradients encountered at high intensity and free electron densities;
4. Extend model by focusing of the laser beam below the surface and include optical effects. That is because the base model propagates a nonphysical, collimated beam, see Figure 2.9 at $t = -0.8$[ps], leading to surface processing, see Figure 2.10 at $t = -0.6$[ps];
5. Include change of material properties and phase changes, allowing for an estimation of the morphology of induced modifications.

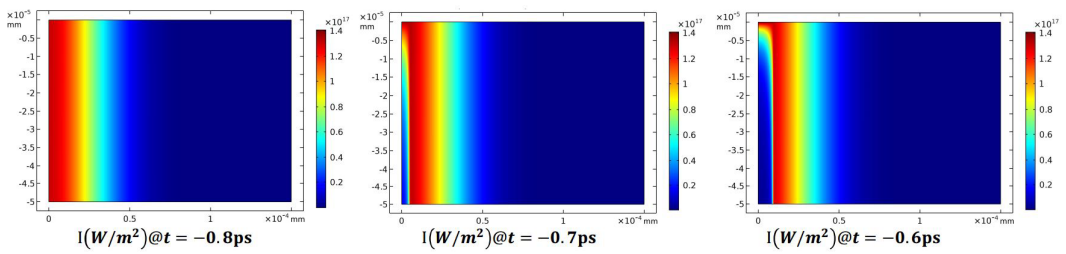

Figure 2.9: Resulting intensity distribution being a collimated laser beam, as used in the base model [21,22].

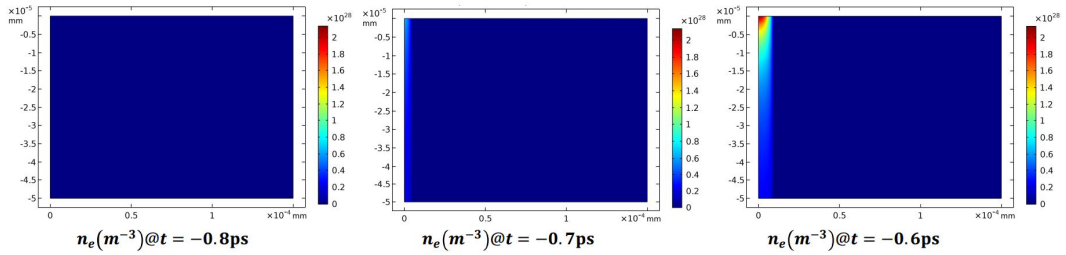

Figure 2.10: Resulting free electron density distribution, due to collimated laser beam used in the base model [21,22].

It was decided to address the following (most essential) suggestions for improvement in this thesis:

1. Implement a focusing laser beam profile to model the subsurface processing of sapphire (see suggestion 4. above);

2. Implement boundary conditions, to include interaction with the surrounding sapphire, the base model neglects interaction with the bulk material. This leads to accumulation of the pulse energy, causing and maintaining a high lattice temperature, as no energy diffuses into the bulk material;

3. Add stress calculations (see suggestion 5. above), as in experimental studies [12,13,23] the frequent formation of cracks have been observed, see Figures 1.2 and 1.5, frequently resulting from stress concentrations.

Chapter 3

Theory model improvements

3.1 Introduction

The theory regarding the selected model improvements in Section 2.4 is presented in this chapter. First, the theoretical description of light for laser beam propagation is given (model improvement 1.), leading to a simplified description of a Gaussian pulse in a medium. Subsequently, for each PDE the addition of boundary conditions is evaluated, giving equation where the boundary conditions are justified (model improvement 2.). Next, an extension of the model to determine thermal stress is given (model improvement 3.). Finally, the Drude-Lorentz and saturated absorption models are introduced, two alternative models studied, yet not implemented due to complexity and computational demand.

3.2 Laser beam propagation

The description of laser light propagation is dependent on the optical effects that are to be included in the model. Therefore it is difficult to select a-priori the most suitable theory of light to describe laser-material interaction.

Quantum optics [38], see Figure 3.1, effectively encompasses all optical effects, yet results in a computationally demanding model and is therefore disregarded. Ray optics is at the other end, an oversimplification of light, assuming the wavelength to be infinitesimal, ignoring the wave properties of light, therefore unsuitable for modelling complex optical effects occurring in laser-material interaction.

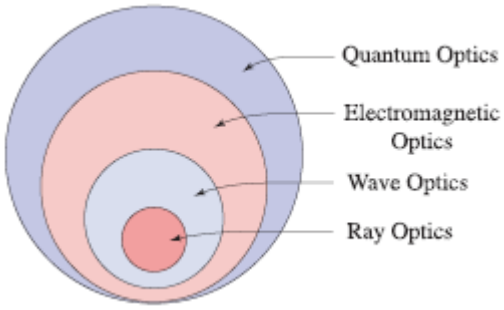

Figure 3.1: Theories of light [38].

The other theories of light, are discussed according to Saleh and Teich [38], starting at electromagnetic optics, leading to wave optics and finally beam optics, by taking several assumptions.

Electromagnetic optics

The description of light is given by two vector fields, the electric ($\mathcal{E}(\mathbf{x},t)$) and magnetic ($\mathcal{H}(\mathbf{x},t)$) field, as a function of space and time. The vector fields are coupled, satisfying Maxwell's equations:

$$\nabla \times \mathcal{H} = \epsilon_0 \frac{\partial \mathcal{E}}{\partial t}, \tag{3.1a}$$

$$\nabla \times \mathcal{E} = -\mu_0 \frac{\partial \mathcal{H}}{\partial t}, \tag{3.1b}$$

$$\nabla \cdot \mathcal{H} = 0, \tag{3.1c}$$

$$\nabla \cdot \mathcal{E} = 0, \tag{3.1d}$$

given for free space, where ϵ_0 and μ_0 are the electric permittivity and magnetic permeability of free space respectively. Additionally, each of the vector field scalars ($\mathcal{E}_x, \mathcal{E}_y, \mathcal{E}_z, \mathcal{H}_x, \mathcal{H}_y, \mathcal{H}_z$) is required to satisfy the wave equation:

$$\nabla^2 u - \frac{1}{c_0^2}\frac{\partial^2 u}{\partial t^2} = 0, \qquad c_0 = \frac{1}{\sqrt{\epsilon_0 \mu_0}}, \tag{3.2}$$

where c_0 is the speed of light in vacuum.

In a medium, lacking free electric charge or current, the effects on light propagation extend Maxwell's equations using the electric ($\mathcal{D}(\mathbf{x},t)$) and magnetic ($\mathcal{B}(\mathbf{x},t)$) flux density:

$$\nabla \times \mathcal{H} = \frac{\partial \mathcal{D}}{\partial t}, \tag{3.3a}$$

$$\nabla \times \mathcal{E} = -\frac{\partial \mathcal{B}}{\partial t}, \tag{3.3b}$$

$$\nabla \cdot \mathcal{D} = 0, \tag{3.3c}$$

$$\nabla \cdot \mathcal{B} = 0, \tag{3.3d}$$

where the vector fields are defined as:

$$\mathcal{D} = \epsilon_0 \mathcal{E} + \mathcal{P}, \tag{3.4a}$$

$$\mathcal{B} = \mu_0 \mathcal{H} + \mu_0 \mathcal{M}, \tag{3.4b}$$

where the polarization ($\mathcal{P}(\mathbf{x},t)$) and magnetization ($\mathcal{M}(\mathbf{x},t)$) vectors depend on the applied magnetic and electric fields and the electric and magnetic material parameters. To describe specific optical effects the equations are modified using additional assumptions.

The electromagnetic power flow of the laser beam is determined by the Poynting vector, showing the direction is orthogonal to the electric and magnetic field:

$$\mathcal{S} = \mathcal{E} \times \mathcal{H}, \tag{3.5}$$

determining the optical intensity by taking the time-average of the Poynting vector:

$$I(\boldsymbol{x},t) = \langle \mathcal{S} \rangle = \frac{1}{T}\int_0^T \mathcal{S}(t)dt, \tag{3.6}$$

describing the power flow across a unit area normal to the Poynting vector [38,39].

Wave optics

Wave optics simplifies the light description to a single scalar wave ($u(\boldsymbol{x}, t)$), known as the wave function, satisfying Equation (3.2). Propagation through a homogeneous medium reduced the speed of light by means of the refractive index (n) according to:

$$c = \frac{c_0}{n}, \qquad n = \sqrt{\frac{\epsilon}{\epsilon_0}\frac{\mu}{\mu_0}}, \tag{3.7}$$

replacing the speed of light in free space (c_0) in Equation (3.2), where ϵ and μ are the electric permittivity and magnetic permeability of the medium.

The optical intensity or irradiance follows from the wave function according to:

$$I(\boldsymbol{x}, t) = 2\langle u^2(\boldsymbol{x}, t)\rangle, \tag{3.8}$$

where the optical power flowing into an area is determined by integration:

$$P(t) = \int_A I(\boldsymbol{x}, t) dA, \tag{3.9}$$

determining the optical pulse energy for a time interval, for example pulse time (t_p), by integration over time:

$$E_p = \int_{t_p} P(t) dt, \tag{3.10}$$

able to describe the laser input, see Section 2.3.1, showing Gaussian power and intensity profiles in Figures 2.3 and 2.4 [38].

Beam optics

Further simplification, within wave optics, assuming monochromatic waves and a complex wave function, reduces Equation (3.2) to the Helmholtz equation:

$$\nabla^2 U + k^2 U = 0, \qquad k = \frac{2\pi}{\lambda} = \frac{\omega}{c_0}, \tag{3.11}$$

where k, λ and ω are the free space wavenumber, optical wavelength and angular frequency respectively. Furthermore, assuming a paraxial wavefront primarily travelling in one direction through a homogeneous medium, i.e. the slowly varying envelope approximation, leads to the paraxial Helmholtz equation:

$$\nabla_T^2 u - j2k_0 \frac{\partial u}{\partial z} = 0, \qquad k_0 = \frac{2\pi n}{\lambda}, \tag{3.12}$$

where k_0 is the reference wave number, satisfied by a paraxial wave according to:

$$U(\boldsymbol{x}) = A(\boldsymbol{x})\text{exp}[-jkz], \tag{3.13}$$

where $A(\boldsymbol{x})$ is a position dependent, slowly varying envelope function, determining the amplitude of the wave. The envelope variation and its derivative require to be slow over the distance of a single wavelength, i.e. maintaining plane-wave behaviour.

The Gaussian beam is one useful solution satisfying Equation (3.12) and (3.13), given for the cylindrical coordinate system and propagation in positive z-direction:

$$U(\boldsymbol{r}) = U_0 \frac{w_0}{w(z)} \exp\Big[- \frac{r^2}{w(z)^2} \Big] \exp\Big[- jk_0 z + j\zeta(z) - jk_0 \frac{r^2}{2R(z)} \Big], \tag{3.14}$$

where w_0, $w(z)$, $R(z)$ and $\zeta(z)$ are the beam radius, beam width, wavefront curvature and Gouy phase defined respectively as:

$$w_0 = \sqrt{\frac{\lambda z_R}{\pi}}, \tag{3.15a}$$

$$z_R = \frac{\pi w_0^2}{\lambda}, \tag{3.15b}$$

$$w(z) = w_0 \sqrt{1 + \Big(\frac{z - z_f}{z_R} \Big)^2}, \tag{3.15c}$$

$$R(z) = (z - z_f) \Big[1 + \Big(\frac{z_R}{z - z_f} \Big)^2 \Big], \tag{3.15d}$$

$$\zeta(z) = \tan^{-1} \Big(\frac{z - z_f}{z_R} \Big), \tag{3.15e}$$

where z_f is the focal point and z_R is the Rayleigh length.

At $z = 0$, the focal point, the beam width is equal to beam diameter or spot size ($2w_0$), diverging further outside the depth-of-focus according to a hyperbolic relation. The depth-of-focus for a Gaussian beam is the confocal parameter (b), equal to twice the Rayleigh length, at which the the beam radius has increased by a factor of $\sqrt{2}$, see Figure 3.2a [26,40,41].

The first term in the exponential of Equation (3.14) describes plane wave behaviour, followed by the second term describing the phase. Here the Gouy phase, see Figure 3.2a, multiplied by 10^2 to emphasize its behaviour, shows that the phase advances around the focal region, due to wavefront curvature changing rapidly over the length of a single wavelength. It causes the wave velocity to surpass the speed of light, however the wave equation is still satisfied, however the phase shift is stronger for higher-order Gaussian beam modes [42].

The shape of the wavefronts is determined by the final term in the exponential term of Equation (3.14), where $R(z)$ describes the wavefront curvature. At $z = 0$ the wavefront has no curvature, increasing to maximum curvature at the Rayleigh length ($\pm z_R$), followed by a gradual decrease of curvature outside the depth-of-focus, see Figure 3.2b [38,43].

The optical intensity of the Gaussian beam, as a function of the spatial coordinates, is:

$$|U(\boldsymbol{r})|^2 = I(r, z) = I_0 \Big[\frac{w_0}{w(z)} \Big]^2 \exp\Big[- \frac{2r^2}{w(z)^2} \Big], \tag{3.16}$$

where I_0 represent the maximum power of the beam, where Equation (3.9) and 3.10 are used to include a time-dependent behaviour.

The (2D) Gaussian intensity profile, see Figure 3.2c and 3.2d, showing the distribution of the intensity at the peak of the pulse ($t = 0$), excluding any material or optical effects modifying the beam profile.

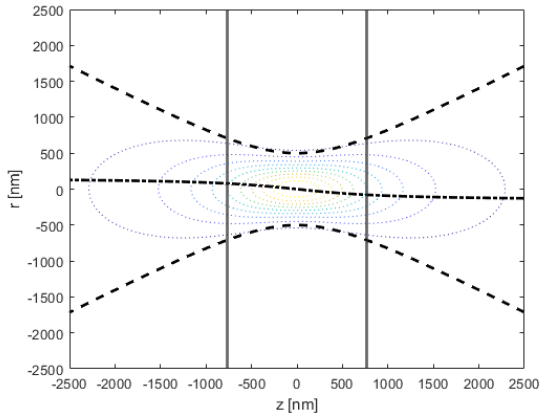

(a) $w(z)$ $(--)$ and $\zeta(z) * 10^2$ $(-\cdot)$.

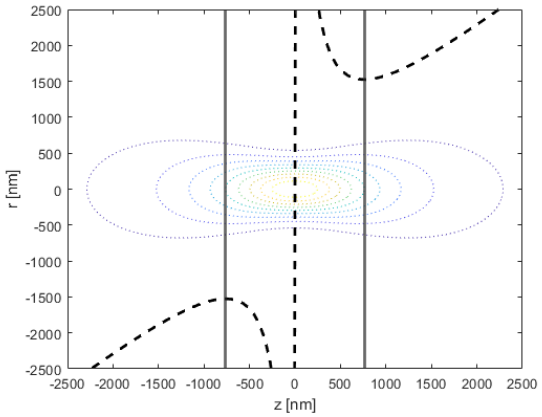

(b) $R(z)$ $(--)$ and $2z_R$ $(-)$.

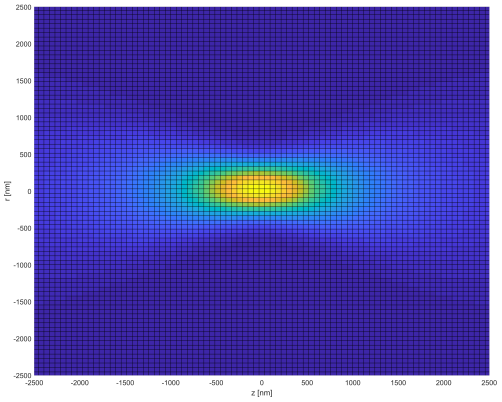

(c) Gaussian intensity profile (r, z).

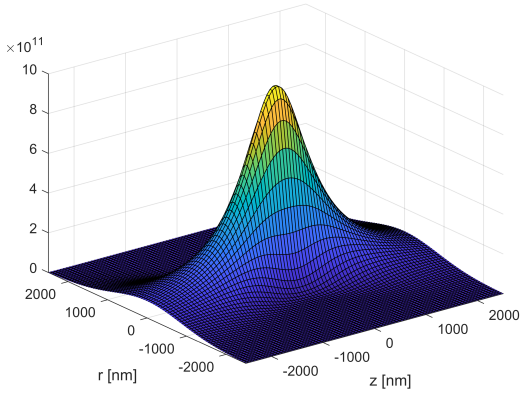

(d) Gaussian intensity profile (r, z, I).

Figure 3.2: Gaussian beam parameters and intensity profile ($I_0 = 10^{12}, w_0 = 500[\text{nm}]$, $\lambda = 1030[\text{nm}], z_f = 0[\text{nm}]$).

In version 5.3a of COMSOL Multiphysics®, used for this thesis, the paraxial Helmholtz equation is unavailable and using wave properties of light increases computational time significantly. Therefore, the Gaussian optical intensity profile derived from wave optics, Equation (3.16), is selected. The intensity profile is sufficient to compute a material response, but neglects optical effects, for implementation, see Chapter 4.

3.3 Boundary conditions

The base model, see Chapter 2, lacks proper boundary conditions, neglecting interaction with the surrounding bulk material. That is, in the base model all PDEs (I, n_e, T_e, T_l) have zero flux boundary conditions, containing all effects within the domain.

The PDE describing the changing local intensity, see Equation (2.4), uses a spatial derivative to determine the intensity distribution. In the base model an input boundary conditions at the top surface sets the conditions for this distribution, where only absorption terms in the domain, depending on (local) intensity and free electron density, modify the shape of the profile. Boundary conditions do not affect the shape of the beam and are therefore not implemented, maintaining the zero flux boundary conditions.

Similarly, in the base model the PDE describing free electron density, see Equation (2.5), models (local) excitation of electrons dependent on the incident intensity and free electron density. Including interaction with the bulk material, the transport of electrons, requires a drift-diffusion model [31,44,45], introducing new equations and considerably extending the model. Again, in the base model the PDE is unaffected by boundary conditions and therefore not implemented, maintaining the zero flux boundary conditions.

Electron temperature diffusion

The PDE determining free electron temperature, see Equation (2.6), includes diffusion behaviour in the calculation domain. Thus, boundary conditions properly describing continuing diffusion into the bulk sapphire affects the free electron temperature.

The boundary conditions to describe diffusion into the bulk are in accordance with thermal conduction [46]. Dependent on the electron thermal conductivity (K_e), a heat flux boundary condition is therefore proposed:

$$\phi_{T_e} = -K_e \nabla T_e, \tag{3.17}$$

emulating the electron diffusion behaviour in the domain, dependent on the free electron temperature and free electron density at the boundary, see Equation (2.15).

Lattice temperature diffusion

The PDEs modelling electron and lattice temperature describe an identical quantity and the lattice temperature PDE contains a heat conduction term, depending on the thermal conductivity (k). A boundary condition analogous to Equation (3.17) is proposed:

$$\phi_{T_l} = -k \nabla T_l, \tag{3.18}$$

depending only on the lattice temperature at the boundary, as the thermal conductivity is constant, conduction into the bulk material is modeled.

The implementation of the boundary conditions in COMSOL Multiphysics® is further elaborated in Chapter 4.

3.4 Thermal stress

The base model, see Chapter 2, does not include material modification. The lattice temperature of the material during and post-processing modifies the material. Besides thermal effects several other material modifications occur, phase changes leading to amorphization and void formation characterize the post-processing morphology [12].

Yet, the temperature and temperature changes in sapphire are available in the base model, described by Equation (2.7), leading to thermal stress and possibly connected to crack formation. To determine the influence of thermal stress, the inverted constitutive equation describing the induced thermal stress is implemented [27,47,48]:

$$\boldsymbol{\sigma} = \boldsymbol{C}(\boldsymbol{\epsilon} - \alpha T_l), \tag{3.19}$$

where ($\boldsymbol{C}$) is the elasticity tensor, dependent on material properties, giving the full form for

isotropic sapphire in cylindrical coordinates:

$$\begin{Bmatrix} \sigma_r \\ \sigma_\theta \\ \sigma_z \end{Bmatrix} = \frac{E}{(1-2\nu)(1+\nu)} \begin{bmatrix} (1-\nu) & \nu & \nu \\ \nu & (1-\nu) & \nu \\ \nu & \nu & (1-\nu) \end{bmatrix} \begin{Bmatrix} \epsilon_r \\ \epsilon_\theta \\ \epsilon_z \end{Bmatrix} - \frac{E}{(1-2\nu)} \begin{Bmatrix} \alpha_r T_l \\ \alpha_\theta T_l \\ \alpha_z T_l \end{Bmatrix}, \tag{3.20}$$

where ν and E are Poisson's ratio and Young's modulus given in Table 2.1.

As the model is 2D axisymmetric and only the thermal strain is modeled ($\epsilon_r = \epsilon_\theta = \epsilon_z = 0$), which reduced Equation (3.20) to:

$$\begin{Bmatrix} \sigma_r \\ \sigma_z \end{Bmatrix} = -\frac{E}{(1-2\nu)} \begin{Bmatrix} \alpha_r T_l \\ \alpha_z T_l \end{Bmatrix}, \tag{3.21}$$

leading to stress exclusively due to thermal expansion, dependent on the lattice temperature and thermal expansion coefficient (α).

The thermal expansion coefficient is dependent on the temperature and orientation with respect to the crystallographic planes, see Section 2.2 and Figure 3.3. A wide range of thermal expansion coefficient is found in literature, showing nonlinear behaviour as shown in Figure 3.3, however an equation is unavailable.

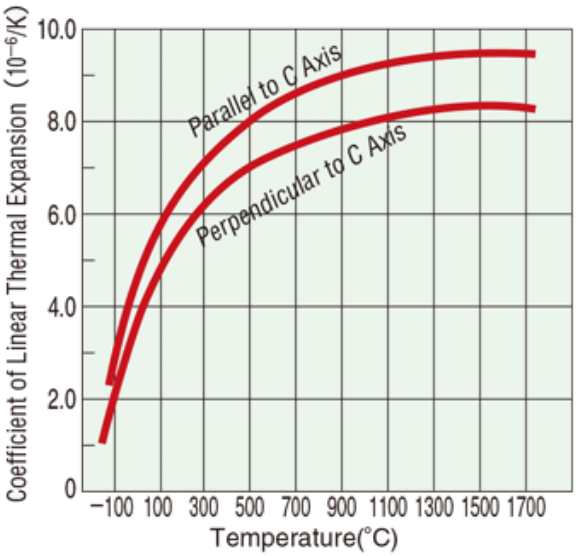

Figure 3.3: Thermal expansion coefficient dependent on temperature and orientation to C-axis [25].

Therefore, based on the limited data available, for relative elongation and averaged expansion parallel and perpendicular to the C-axis, see Figure 3.4, a linear approximation of the thermal expansion coefficient is determined. Selecting the approximation based on the averaged C-axis expansion, as the polynomial approximation of the data in Figure 3.4 most closely resembles the coefficients shown in Figure 3.3. This leads to the following equation determining the linear expansion coefficient:

$$\alpha_r = \alpha_z = 5.4664 \cdot 10^{-6} + 0.0026 \cdot 10^{-6} T_l, \tag{3.22}$$

maintaining the assumption of isotropic material, see Section 2.2. That is, the coefficient in radial, perpendicular to the symmetric axis, and height direction, parallel to the symmetric axis, is identical.

The implementation of the thermal stress in COMSOL Multiphysics® is further discussed in Chapter 4.

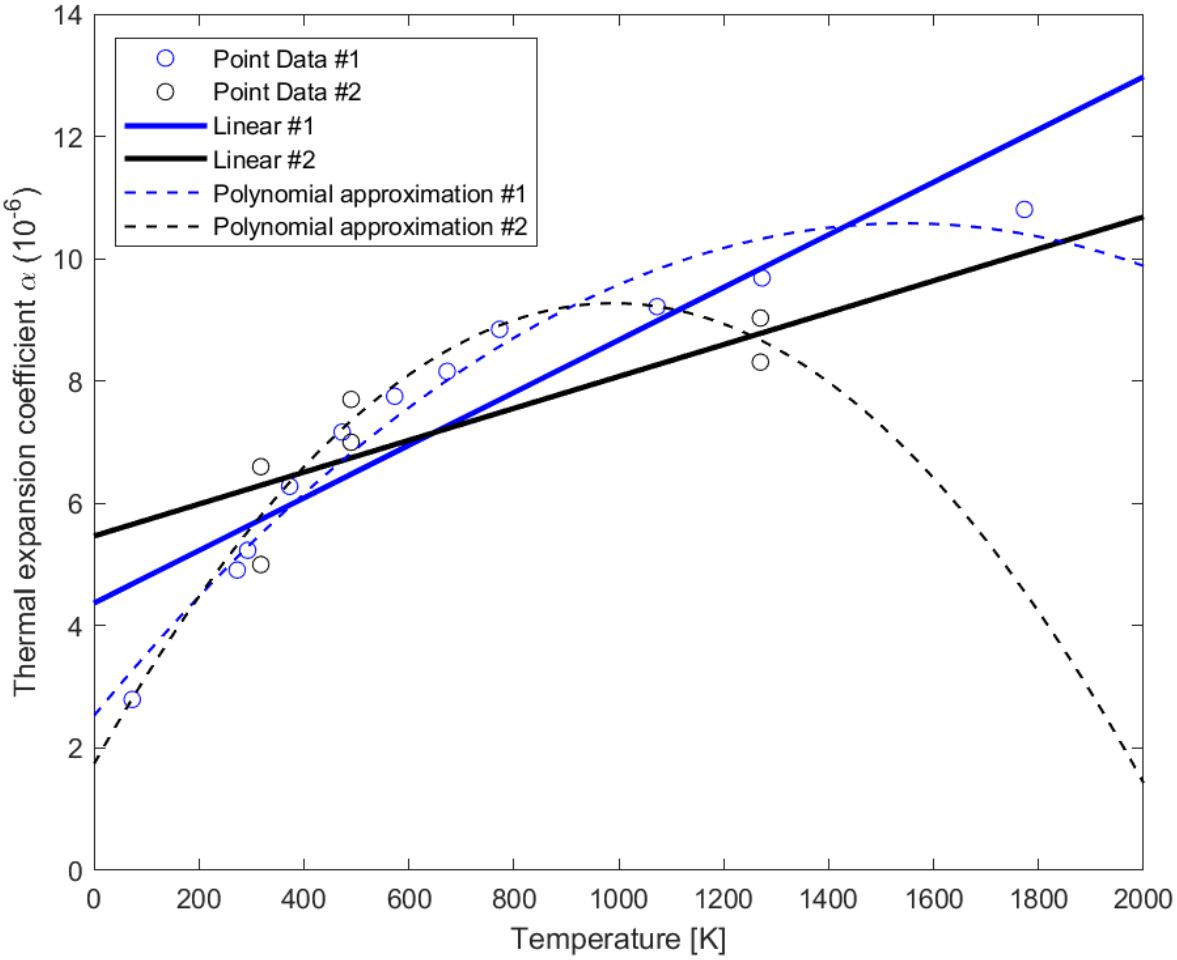

Figure 3.4: Thermal expansion coefficient (α), point data, linear and polynomial approximations based on relative elongation (#1) and averaging of the expansion parallel and perpendicular to the C-axis (#2) (produced from [2]).

3.5 Alternative absorption models

The suggestion to include optical effects (model suggestion 4., see Section 2.4) has been considered, to connect absorption effects and electromagnetic or wave optics, described in Section 3.2. Modelling these optics increase the complexity of the base model significantly, modifying the model input by replace the PDE shaping the intensity. Accordingly, a new connection to the other PDEs, for a comprehensive model, has to be found.

Several possibilities to model were evaluated, of which two, the Drude-Lorentz and saturated absorption model were most suitable due to limited complexity, however the exact connection to the optics and base model remained unclear.

Both models are discussed briefly in the following sections, requiring Maxwell's equa-

tions, extended by the material effects according to Equations (3.3a) to (3.3d). Where for Equations (3.4a) and (3.4b), describing the material effects, magnetization of sapphire is neglected, as magnetic susceptibility is negligible ($\chi_m < 10^{-6}$) and electric susceptibility is high ($\chi_e < 10^1$), assuming all material effects are due to polarization [2,38,49]:

$$\mathcal{P} = \epsilon_0 \chi_e \mathcal{E} = (\epsilon_r - 1)\mathcal{E}, \tag{3.23a}$$
$$\mathcal{M} = \chi_m \mathcal{H} = (\mu_r - 1)\mathcal{H} = 0 \tag{3.23b}$$

3.5.1 Drude-Lorentz model

The Drude-Lorentz model [50–52] is a combination of the Drude model for electron transportation in metals or highly doped semiconductors, extended by the Lorentz model, to include dispersion around a resonant frequency. The Drude model uses a dielectric function to describe the changing electric permittivity of the medium in Maxwell's equations:

$$\epsilon_r = \epsilon_\infty - \frac{\omega_p^2}{\omega(\omega + j\gamma)}, \tag{3.24}$$

where the high frequency permittivity (ϵ_∞), damping term (γ) are material dependent and the plasma frequency is given by:

$$\omega_p = \sqrt{\frac{n_e e^2}{\epsilon_0 m_e^*}}, \tag{3.25}$$

where n_e, e, ϵ_0 and m_e^* are the free electron density, electron charge, free space permittivity and effective electron mass respectively. The frequency of light in the Drude model describes absorption for $0 < \omega < \gamma$, reflection for $\gamma < \omega < \omega_p$ and transmission for $\omega > \omega_p$.

The extension by Lorentz includes strong dispersion, around a resonance frequency (ω_0), giving the following equation:

$$\epsilon_r = \epsilon_\infty - \frac{\omega_p^2}{\omega(\omega + j\gamma)} + \frac{\Delta_\in \omega_p^2}{-\omega^2 + j\gamma\omega + \omega_o}, \tag{3.26}$$

yet, the dependence on frequency makes the implementation into a time-dependent study ambiguous.

3.5.2 Saturated absorption model

The saturated absorption model [53–55] simulates electron kinetics for a saturable absorber, i.e. materials with a nonlinear absorption coefficient. At low intensity the photons are absorbed, exciting electron to the CB, as explained in Section 2.3.2. When recombination is infrequent the excited electrons remain in the CB while more electrons are excited, decreasing the amount of electrons in the VB available for excitation, thus saturating the absorption effect.

Combining the excitation with rate equations, similar to Equation (2.5), a new equation describing free electron density is obtained. Additionally, the saturated absorption model allows for a multilevel system, see Figure 3.5, for absorption at different frequencies of light. A two-level system uses the following equation:

$$\frac{dN_1}{dt} = -\frac{N_1}{\tau_{rec}} + \frac{1}{\hbar\omega_0}\mathbf{E} \cdot \frac{d\mathbf{P}}{dt}, \qquad N_{tot} = N_0 + N_1, \tag{3.27}$$

where N_1, N_0, N_{tot} are the free, bounded and total electron population density, conserving the number of electrons. The lifetime of the free electrons is determined by the recombination time (τ_{rec}) and the excitation by the transition frequency (ω_0) and reduced Planck constant ($\hbar$).

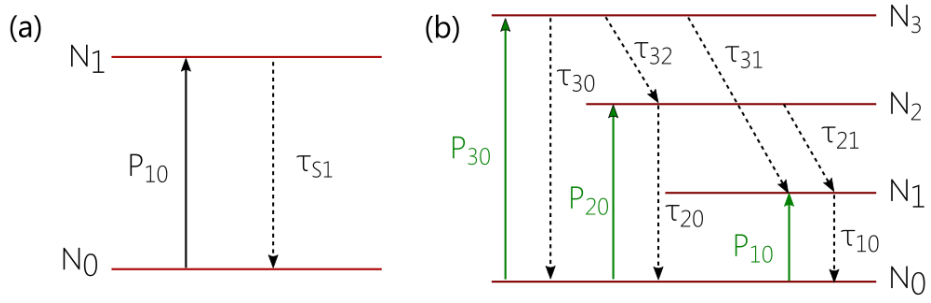

Figure 3.5: Jablonski diagrams of two- and four-level systems, showing transition and relaxation times [53].

The excited electrons lead to macroscopic polarization, depending on the difference in electron energy in the excited and bounded state. The polarization is described using the following equation:

$$\frac{d^2\mathbf{P}_{10}}{dt^2} + \gamma_{10}\frac{d\mathbf{P}_{10}}{dt} + \omega_0^2\mathbf{P}_{10} = \kappa(N_0 - N_1)\mathbf{E}, \qquad \kappa = \frac{6\pi\epsilon_0 c^3}{\tau_{rec}\omega_0\sqrt{\epsilon_r}}, \tag{3.28}$$

where κ is the coupling factor between the polarization and electric field vector, ϵ_r is the permittivity of the medium and γ_{10} the sum of all damping effects.

The macroscopic polarization is coupled with Maxwell's equations using Equation (3.4a), to describe absorption effects affecting the electric field vector. However, the model is disregarded as the connection to the free electron temperature is unclear, electromagnetic wave optics increases the computational demand and complexity of the model.

Finally, the optical intensity profile was selected, see Section 3.2, neglecting the optical effects, described using the wave properties of light.

Chapter 4

Model implementation

The first primary objective, see Section 1.2, is the implementation of improvements in the existing base model. The theoretical framework of the improvements, which were discussed in Chapter 3, serve as the guideline for the implementation.

The improved model, see Figure 4.1, includes the additional components and displays new relations and subsequent interaction. However, the modules representing the relevant physics in COMSOL Multiphysics® have limited options due to set equations for each module, also discussed in this chapter.

First, the Gaussian optical intensity profile implementation is described, followed by the implementation of boundary conditions. Third, the implementation of thermal stress is described, as an extension of the model, requiring two additional physics modules in COMSOL Multiphysics®. Finally, the mesh and solver configuration are adjusted for the improved model, along with accounting for the maximum available electrons, further stabilizing the model numerically.

4.1 Laser intensity distribution

The Gaussian optical intensity profile describes the laser pulse as a function of space and time, see Section 2.3.1. In the base model this results in a collimated beam. Therefore Equation (3.16) for optical intensity requires modification to include a time-dependent component, according to Equation (2.1), leading to an adapted boundary condition:

$$I(r,z,t) = \frac{2P(t)}{\pi w(z)^2}\exp\left[\frac{-2r}{w(z)^2}\right], \tag{4.1}$$

where, for differentiation, the beam radius ($w(z)$) according to Equation (3.15c) is rewritten using Equations (3.15a), (3.15b) and the beam divergence of a Gaussian laser beam [56]:

$$\theta = \frac{\lambda}{\pi w_0}, \tag{4.2}$$

to substitute the beam radius (w_0) and Rayleigh length (z_R), resulting in a beam diameter dependent on the spatial coordinate z:

$$w(z) = \frac{\lambda}{\pi\theta}\sqrt{1+\left(\frac{\lambda(z-z_f)}{\pi(\frac{\lambda}{\pi\theta})^2}\right)^2}, \tag{4.3}$$

and the optical wavelength (λ), radial beam divergence (θ) and focal point (z_f) as constants.

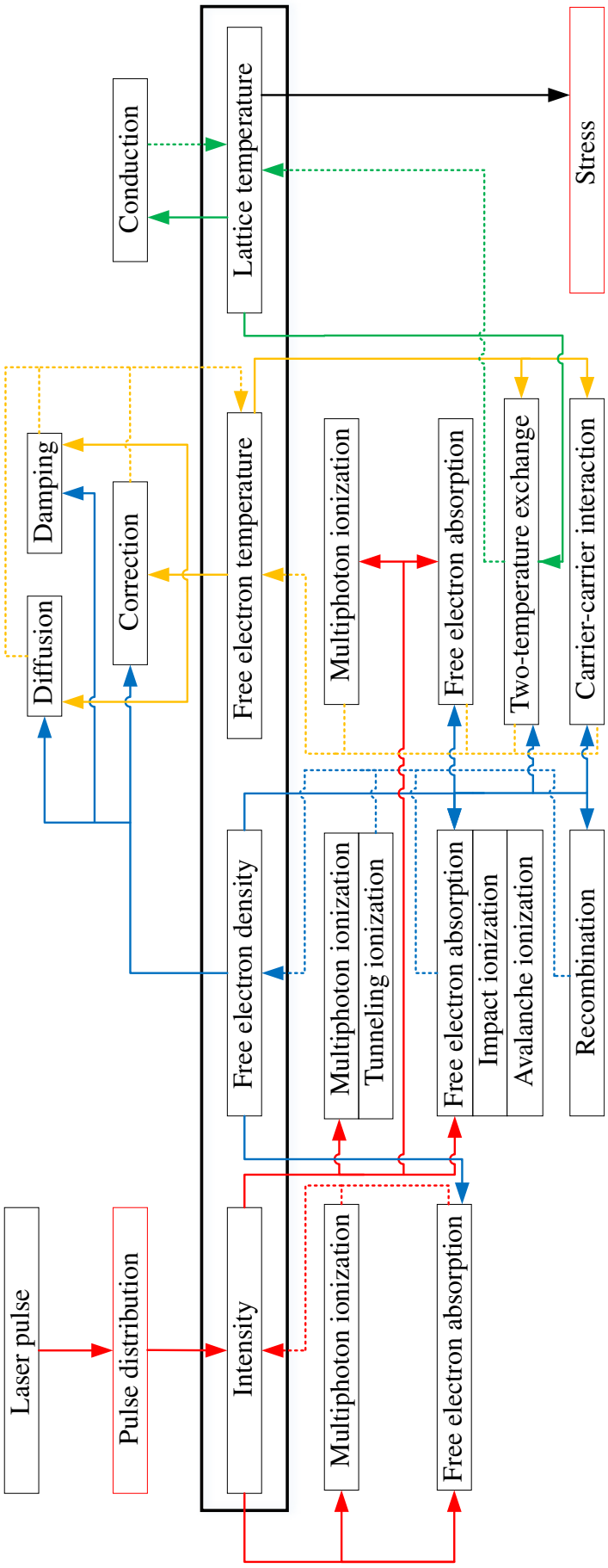

Figure 4.1: Improved model relations and variable interaction (additions in red boxes).

The modification of the boundary condition alone is insufficient to describe the intensity profile in the domain. The intensity PDE, Equation (2.4), shapes the intensity profile using a spatial derivative, thus a spatial and temporal component is modified to describe the Gaussian pulse:

$$\frac{\partial I}{\partial z} = -L_{mpi}(I) - L_{abs}(I, n_e) + P(t)D_{pulse}(r, z), \tag{4.4}$$

where the temporal profile ($P(t)$), according to Equation (2.1), determines the change of intensity w.r.t. time in the domain.

However, the spatial component of the term requires differentiation, as stated above, using Equations (4.1) and (4.3):

$$\begin{aligned} D_{pulse}(r,z) = 2\pi^3 \exp\left[-\frac{2r^2\theta^2\pi^2}{\lambda^2\left(\frac{\pi^2(z_f-z)^2}{\lambda^2\theta^4}+1\right)}\right] \frac{(2z_f-2z)}{\lambda^4\theta^2\left(\frac{\pi^2(z_f-z)^2}{\lambda^2\theta^4}+1\right)^2} \\ - 4r^2\pi^5 \exp\left[-\frac{2r^2\theta^2\pi^2}{\lambda^2\left(\frac{\pi^2(z_f-z)^2}{\lambda^2\theta^4}+1\right)}\right] \frac{2z_f-2z}{\lambda^6\left(\frac{\pi^2(z_f-z)^2}{\lambda^2\theta^4}+1\right)^3}, \end{aligned} \tag{4.5}$$

describing the spatial intensity distribution after integration.

4.2 Boundary conditions

In COMSOL Multiphysics® the options for boundary conditions are different for each physics module. For the PDE modules options are limited, whereas for the Heat Transfer module, used to model the lattice temperature via the classical heat equation, more options are available.

Electron temperature flux

The boundary condition for electron temperature diffusion, see Equation (3.17), into the bulk is implemented using a flux boundary conditions:

$$-\boldsymbol{n} \cdot (-K_e \nabla T_e) = g - qT_e, \tag{4.6}$$

where g and q are the free variables.

Modifying q, depending on the normal ($\boldsymbol{n}$) at the boundary, the electron-thermal flux over the length of the boundary is:

$$q_r = \frac{K_e}{\Delta z}, \qquad q_z = \frac{K_e}{\Delta r}, \tag{4.7}$$

where q_r is used at the boundary where the normal points in r-direction, the right boundary. Hence q_z is used at the boundaries where the normal points in the z-direction, the bottom boundary.

Lattice temperature conduction

The boundary condition for lattice temperature diffusion, see Equation (3.18), into the bulk is implemented using a thin layer boundary conditions, applying a thermally thick layer

approximation. The equation describing conduction into the thick layer is:

$$-\boldsymbol{n}\cdot\boldsymbol{q} = -\frac{1}{2}d\rho C_p\frac{\partial T_{tl}}{\partial t} - \frac{(T_l - T_{tl})}{R} + \frac{1}{2}dQ \quad \text{and} \quad R = \frac{d}{k}, \tag{4.8}$$

increasing the layer thickness (d) in the boundary condition leads to a layer size comparable to an infinite domain approximation. Where, the layer density (ρ), heat capacity (C_p) and thermal conductivity (k) are equivalent to the domain.

The first term ($\frac{1}{2}d\rho C_p\frac{\partial T_{tl}}{\partial t}$) describes the temperature change in the layer and the second term ($\frac{(T_l - T_{tl})}{R}$) the heat conduction to the layer. The final term ($\frac{1}{2}dQ$) is neglected, because it describes an external source, providing heat to the domain, not present in the described model.

4.3 Thermal stress

To include thermal stress the model requires extension implementing additional modules in COMSOL Multiphysics®, connecting to the Heat Transfer module describe the lattice temperature. The Multiphysics module of Thermal Expansion connects the lattice temperature to the Solid Mechanics module, to generate a thermal stress output.

Thermal expansion

The Multiphysics module of Thermal Expansion couples the temperature effects to the structural domain described by Solid Mechanics. The coupling is assumed to be thermoelastic damping, neglecting mechanical losses, describing a direct connection between the displacement, due to expansion and the temperature field output from Equation (2.6), using thermal strain:

$$\epsilon_{th} = \alpha(T_l)(T_l - T_{ref}), \tag{4.9}$$

where the secant coefficient of thermal expansion coefficient is temperature dependent, see Equation (3.22) and the volume reference temperature (T_{ref}) is equal to the temperature at which the strain is zero ($\epsilon_{th} = 0$).

Solid mechanics

The Solid Mechanics module determines displacement due to stress and external forces, independent of the coordinate system, according to:

$$\rho\frac{\partial^2\boldsymbol{u}}{\partial t^2} = \nabla\cdot\boldsymbol{S} + \boldsymbol{F}, \tag{4.10}$$

using the second Piola-Kirchhoff (PK2) stress tensor ($\boldsymbol{S}$) and volume forces ($\boldsymbol{F}$). Where the PK2 stress tensor is defined similarly to Equation (3.19):

$$\boldsymbol{S} = \boldsymbol{C} : \boldsymbol{\epsilon}_{el}, \qquad \boldsymbol{\epsilon}_{el} = \boldsymbol{\epsilon} - \boldsymbol{\epsilon}_{inel}, \tag{4.11}$$

using the stiffness tensor ($\boldsymbol{C}$), expanded in Equation (3.20), and the elastic strain tensor ($\boldsymbol{\epsilon}_{el}$), consisting of all elastic strains, as the inelastic strains ($\boldsymbol{\epsilon}_{inel}$) are subtracted.

The elastic strain depends on the strain tensor, determined by the displacement field, using:

$$\boldsymbol{\epsilon} = \frac{1}{2}\Big[(\nabla\boldsymbol{u})^T + \nabla\boldsymbol{u}\Big] = 0, \tag{4.12}$$

as no other effects cause displacement ($\boldsymbol{u} = 0$), the strain tensor is zero ($\boldsymbol{\epsilon} = 0$) and the inelastic strain remains:

$$\boldsymbol{\epsilon}_{inel} = \boldsymbol{\epsilon}_0 + \boldsymbol{\epsilon}_{ext} + \boldsymbol{\epsilon}_{th} + \boldsymbol{\epsilon}_{hs} + \boldsymbol{\epsilon}_{pl} + \boldsymbol{\epsilon}_{cr} + \boldsymbol{\epsilon}_{vp}, \tag{4.13}$$

containing initial ($\boldsymbol{\epsilon}_0$), external ($\boldsymbol{\epsilon}_{ext}$), thermal ($\boldsymbol{\epsilon}_{th}$), hygroscopic ($\boldsymbol{\epsilon}_{hs}$), plastic ($\boldsymbol{\epsilon}_{pl}$), creep ($\boldsymbol{\epsilon}_{cr}$) and viscoplastic ($\boldsymbol{\epsilon}_{vp}$) strain respectively.

As only thermal strain is considered, defined in Equation (4.9), Equation 4.10 is simplified to:

$$\rho \frac{\partial^2 \boldsymbol{u}}{\partial t^2} = \nabla \cdot (\boldsymbol{C} : -\boldsymbol{\epsilon}_{th}), \tag{4.14}$$

leading to the following definition of thermal stress:

$$\boldsymbol{S} = \boldsymbol{C} : -\boldsymbol{\epsilon}_{th}, \tag{4.15}$$

used to evaluate stress in the material.

4.4 Mesh and solver configuration

The base model configuration for the mesh and solver, defined by de Zeeuw [22], is modified to meet requirements for the improved model, increasing simulation speed and stability of the model extensions.

Mesh configuration

The width of the domain is reduced, to reduce nodes of the mesh, decreasing random-access memory (RAM) use for calculations. Nonetheless, the implementation of a finer mesh virtually negates this effect, as the resolution of the model is increased significantly.

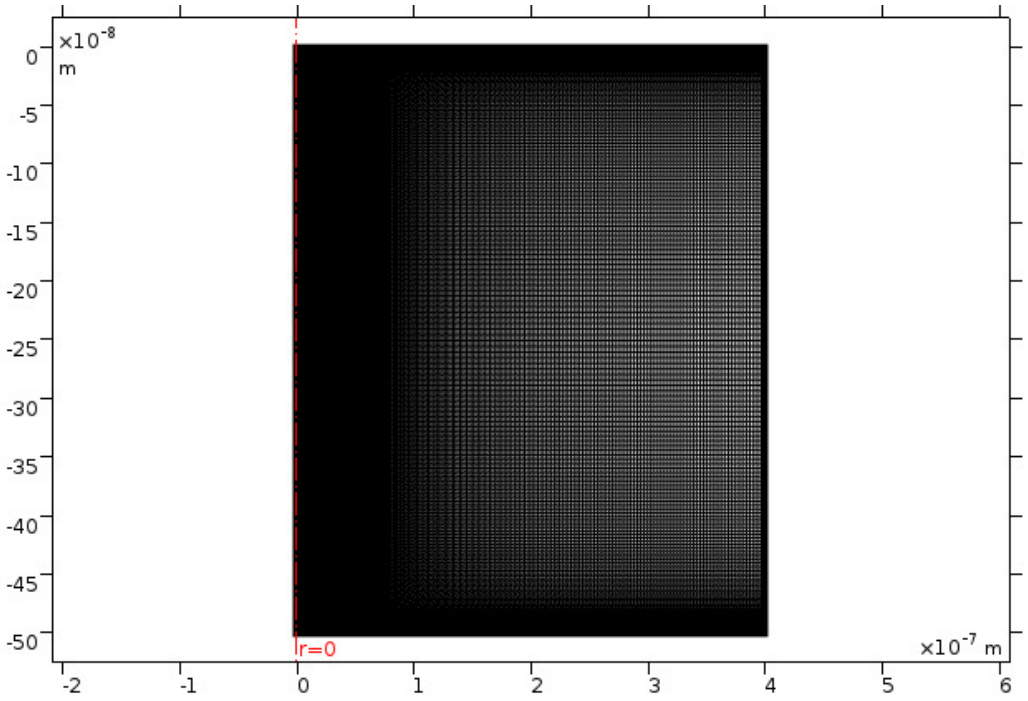

Figure 4.2: 2D model dimensions and refined mesh.

The entire mesh is reshaped to the implementation of the subsurface intensity profile, see Figure 4.2. Consisting of two distribution, from the top to the bottom boundary and from the symmetric axis to the right boundary, resulting in a denser mesh at the areas of interest.

The top to bottom distribution consists of 200 rectangular elements and the symmetric axis to right boundary consists of 250 rectangular elements. Both distributions apply an elements ratio of 0.01, resulting in a total of $50,000$ elements in the domain of which 900 elements are on the boundary.

The top-bottom distribution is a reverse symmetric distribution, giving a very fine mesh near the top and bottom boundary, growing coarser towards the center. The symmetric axis to right boundary mesh is fine closer to the symmetric axis, becoming coarser when moving towards the right boundary, since the focal point, where most effects are expected to occur, is on the symmetrical axis.

The standard quadratic Lagrange elements are maintained, considering that the convergence issues were related to steep gradient, caused by nonlinear behaviour, difficult to solve on a discrete grid. The mesh refinement is expected to be sufficient to improve stability, leading to convergence.

Solver configuration

The options for the solver configuration are numerous and allow for an extensive study to optimize for the laser-material interaction model. Yet, the time-dependent solver has been changed to MUMPS, as it supports cluster computing, used for the simulations, allowing for more memory use. Additionally, the solver has the capability to store intermediate solutions on the hard disk and is, at time, able to handle ill-conditions simulations [57].

The pulse time was reduced to limit calculation time around the pulse peak occurring at $t = 0$[ps]. Previously it was proved that starting initialization at $t = -10$[ps] is sufficient to prevent converging errors due to the high intensity gradient. Even though the reduced pulse time increases the gradient, the start time is maintained.

The time stepping method used is the Backward Differentiation Formula (BDF), an implicit integration method standard for COMSOL Multiphysics®. Further reducing the minimum time step size to 10^{-10}[ps] and maximum time step to 0.2[ps], using the Backward Euler or implicit Euler method for initialization.

To increase accuracy the tolerance factor was decreased to 10^{-4}, since dependent variables affect each other at each position in space, reducing accumulation of errors. The number of iterations was maintained at 30, as well as further solver settings adjusted by de Zeeuw [22].

Available electrons

Stated in Section 2.4, de Zeeuw [22] suggest the inclusion of the amount of electrons available for excitation leading to an increase of stability. Although the convergence issues have been attributed to the coarse mesh, unable to handle steep gradients, exceeding the amount of electron available is nonphysical. Therefore an equation is used to correct the ionization terms proposed by Bulgakova et al. [58], modifying Equation (2.5):

$$\frac{\partial n_e}{\partial t} = P_{pi,abs}\left(\frac{n_{at} - n_e}{n_{at}}\right) - L_{rec}(n_e), \tag{4.16}$$

where n_{at} is the number of electrons available for ionization.

Chapter 5

Results and discussion

5.1 Introduction

The second primary objective, see Section 1.2, is to simulate several scenarios, to study the effects of laser processing parameters on the various phenomena occurring during laser-material interaction.

Several parameter and settings are changed for the model and new simulations are performed, for each scenario, evaluating the influence of the parameters on the behaviour of the model. The results have been separated, based on the model response to varying pulse energy, into three categories: low, high and higher pulse energy, leading to higher intensity with increasing pulse energy.

First, the general study parameters are presented, identical for each of the categories. Followed by the results for low pulse energy, showing the intensity, free electron density, free electron temperature and lattice temperature distributions. Discussing general model behaviour, improvements and connecting notable physical behaviour to the mathematical description of the model and other studies. Similarly, for high and higher pulse energy the results are presented and discussed.

5.2 Simulation scenarios improved model

The simulation scenarios initialization and spatial parameters of the pulse are identical, see Table 5.1, placing the focus at the center of the symmetrical axis. For the temporal parameters, the laser pulse duration is constant, only the pulse energy of the temporal power profile is changed for each scenario. The pulse profile, see Figure 5.1, matches the Gaussian profile as was shown in Figure 3.2c, described by Equation (3.16).

Table 5.1: General parameters simulation scenarios.

Symbol	Description	Value	Unit
z_f	Focus depth	250	nm
w_0	Beam radius	200	nm
t_p	Pulse time	1	ps
$n_{e,init}$	Initial electron density CB	$2.22 \cdot 10^{-16}$	$1/m^3$
n_{at}	Initial electron density VB	$1.12 \cdot 10^{29}$	$1/m^3$
T_0	Initial temperature	300	K

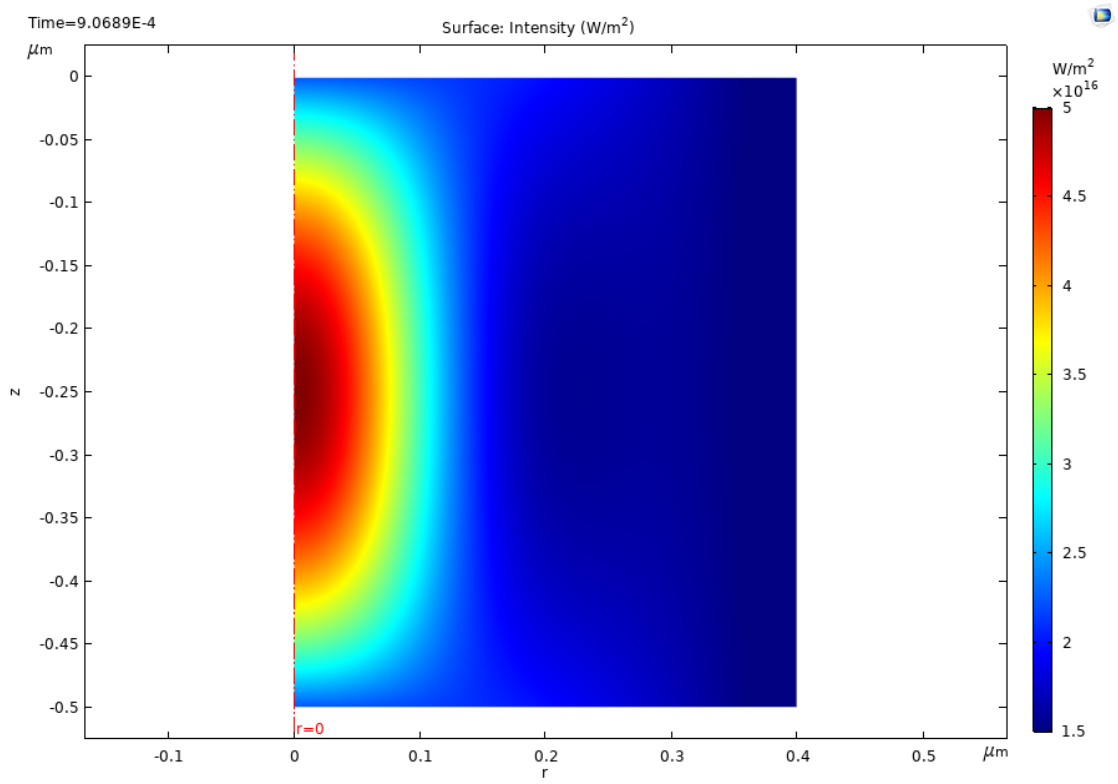

Figure 5.1: Intensity (I) distribution ($E_p = 0.025$[μJ], $t = 0$[ps]).

The levels of intensities, resulting from difference in pulse energy, lead to difference in model behaviour. I.e. certain effects are triggered by high intensity, whereas others are observed for low intensity. Increasing the pulse energy even further causes the behaviour to extend beyond the modeled domain, referred to as higher pulse energy.

5.2.1 Low pulse energy- laser heating

Several studies using low pulse energy, ≤ 0.025[μJ], have been performed, show identical behaviour, similar to laser heating, having only numerical differences. The selected pulse energy, resulting in low intensity distribution, is 0.025[μJ], presenting figures and graphs to describe intensity, free electron density, free electron temperature and lattice temperature behaviour.

Intensity distribution

The evolution of laser intensity as a function of time is shown in Figure 5.2, displaying four different time instances. The pulse intensity in space maintains the Gaussian spatial distribution for each section of the beam profile, as the free electron density is insufficient to cause strong absorption effects which would distort the laser pulse profile.

However, the absorption effects of multiphoton ionization and free electron absorption are triggered in the focus, see Figure 5.3, showing the behaviour in relation to the intensity.

Multiphoton ionization maintain a relatively low production rate, as intensity reaches a maximum of only $5 \cdot 10^{16}$[W/m^2] in the focal point, see Figure 2.6. The multiphoton absorption effect on the intensity is minimal, see Figure 5.4, yet initializes the production of free electrons.

The free electron absorption is influenced by both the intensity and free electron density,

contributing more significantly to absorption, see Figure 5.4. However, the absorption is minimal and insufficient to cause distortion of the laser intensity distribution, as observed at the high and higher pulse energy, see Sections 5.2.2 and 5.2.3.

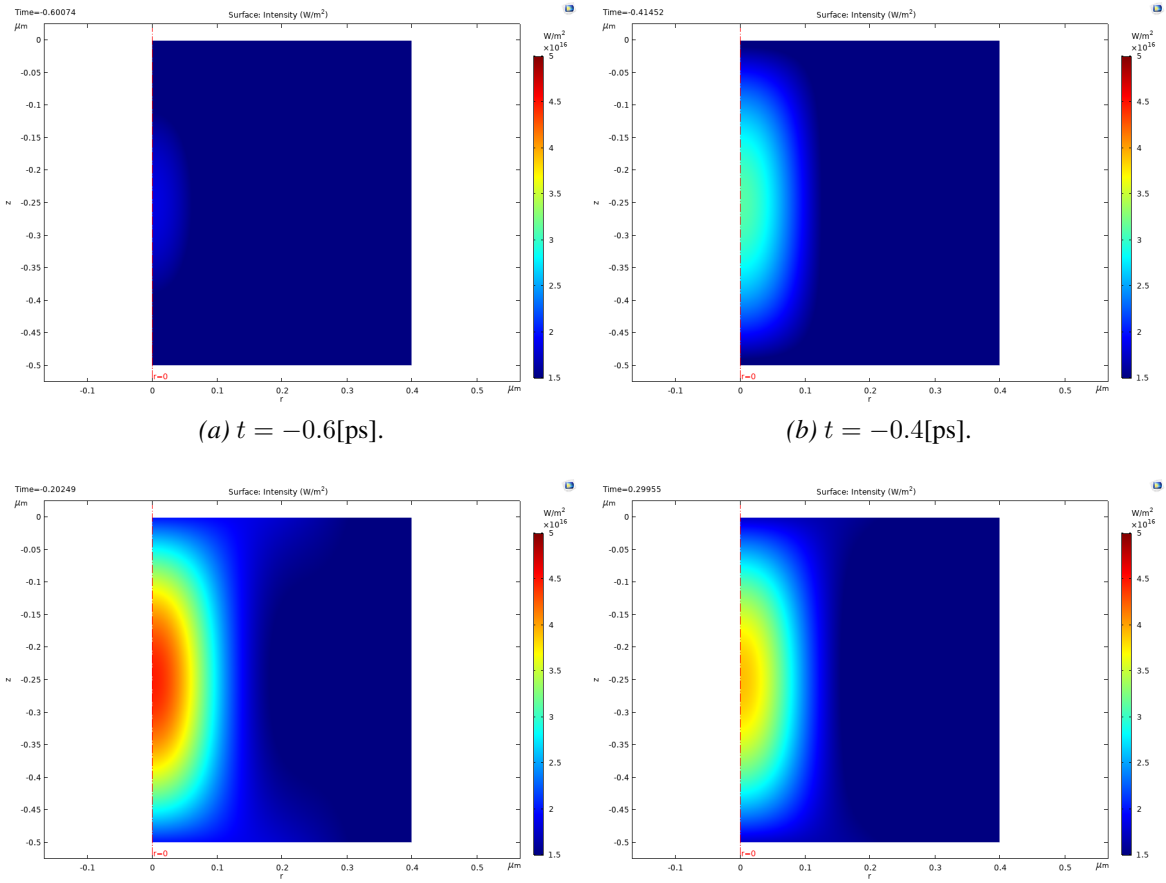

(a) $t = -0.6$[ps]. *(b)* $t = -0.4$[ps].

(c) $t = -0.2$[ps]. *(d)* $t = 0.3$[ps].

Figure 5.2: Intensity (I) distribution in time, low energy pulse ($E_p = 0.025$[µJ]).

Free electron density distribution

The free electron distribution follows the intensity distribution, first according to the Keldysh ionization framework, remaining in the multiphoton regime. Followed by avalanche ionization according to Drude, dominating excitation and the initiation of recombination, when sufficient free electron are generated, see Figure 5.6.

The initial excitation of electrons, up to $t = -0.5$[ps], as the Keldysh ionization rate is nonlinearly dependent on the intensity, see Figure 2.6. The ”saw-like” shape of the electron production rate in the multiphoton regime, see Figure 5.6, is seen in the free electron density distribution due to (local) intensity differences, generating a high free electron density ring surrounding the focal point, see Figure 5.7.

At the edge of the domain, where the intensity is significantly lower, the same sequence of phenomena occurs. For example, at the top boundary, the intensity reaches a maximum of $2.2 \cdot 10^{16}$[W/m^2], remaining in the linear part of the Keldysh framework. Subsequently, the Drude ionization and recombination phenomena display linear behaviour, leading to linear free electron generation at the top surface, see Figures 5.8 and 5.9.

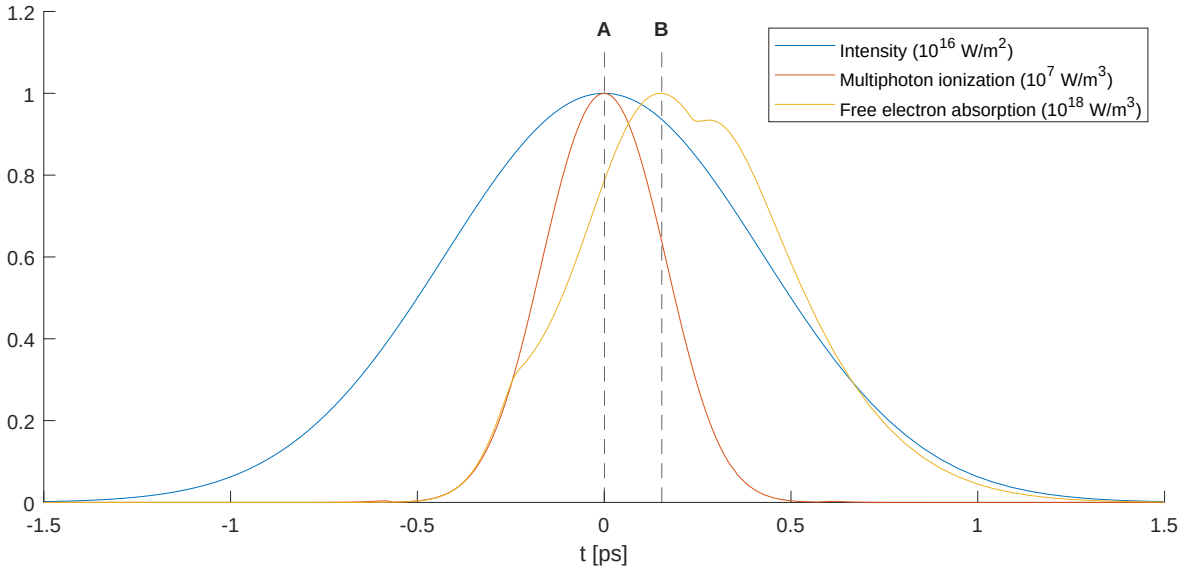

Figure 5.3: Normalized multiphoton ionization (L_{mpi}) and free electron absorption (L_{abs}) response to intensity (I) at $(0, z_f)$, reaching maximum at A and B respectively.

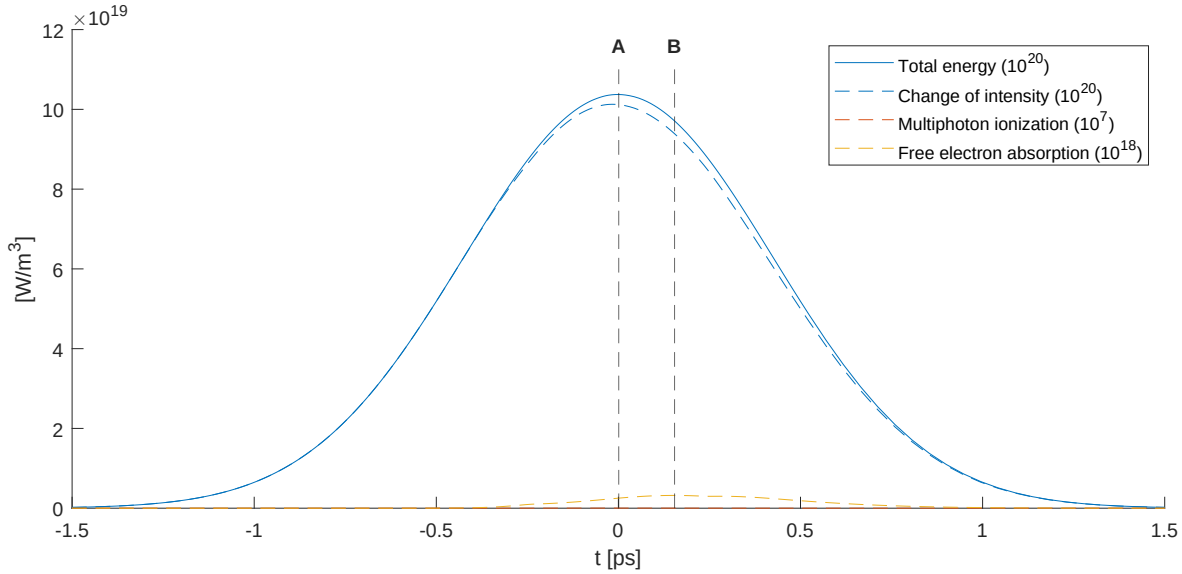

Figure 5.4: Effects of multiphoton ionization (L_{mpi}) and free electron absorption (L_{abs}) on the intensity (I) compared to the total energy incoming at $(0, z_f)$, reaching maximum at A and B respectively.

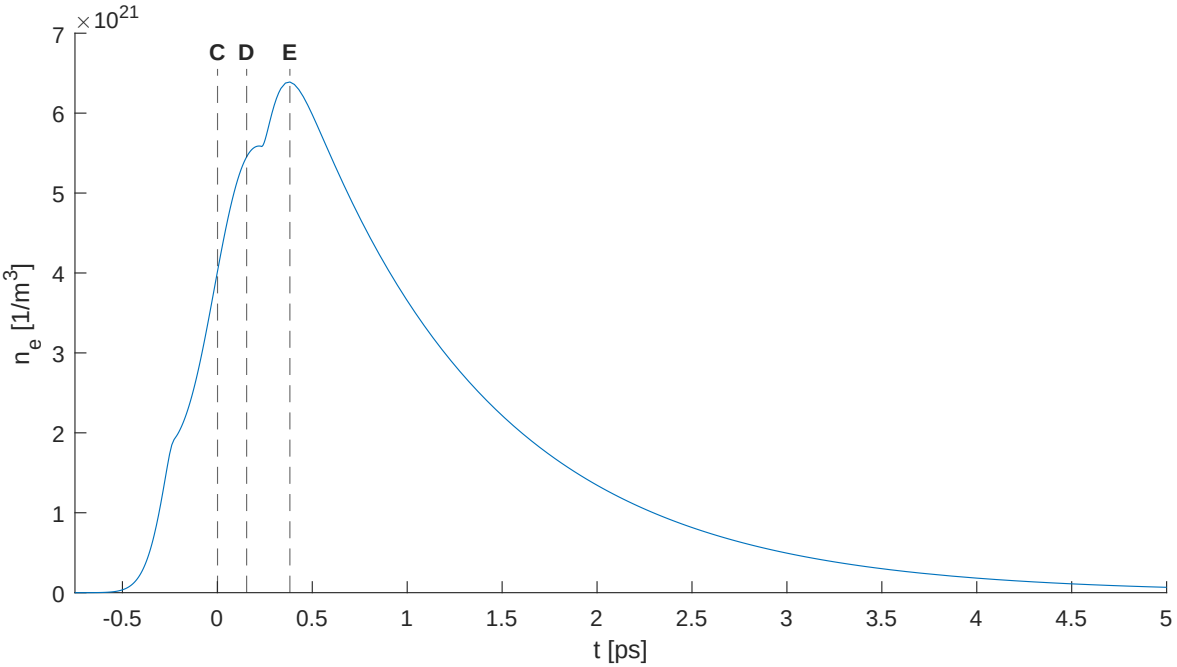

Figure 5.5: Free electron density (n_e) due to Keldysh ionization (P_{pi}), Drude ionization (P_{abs}) and recombination (L_{rec}) at $(0, z_f)$, reaching maximum at C, D and E respectively.

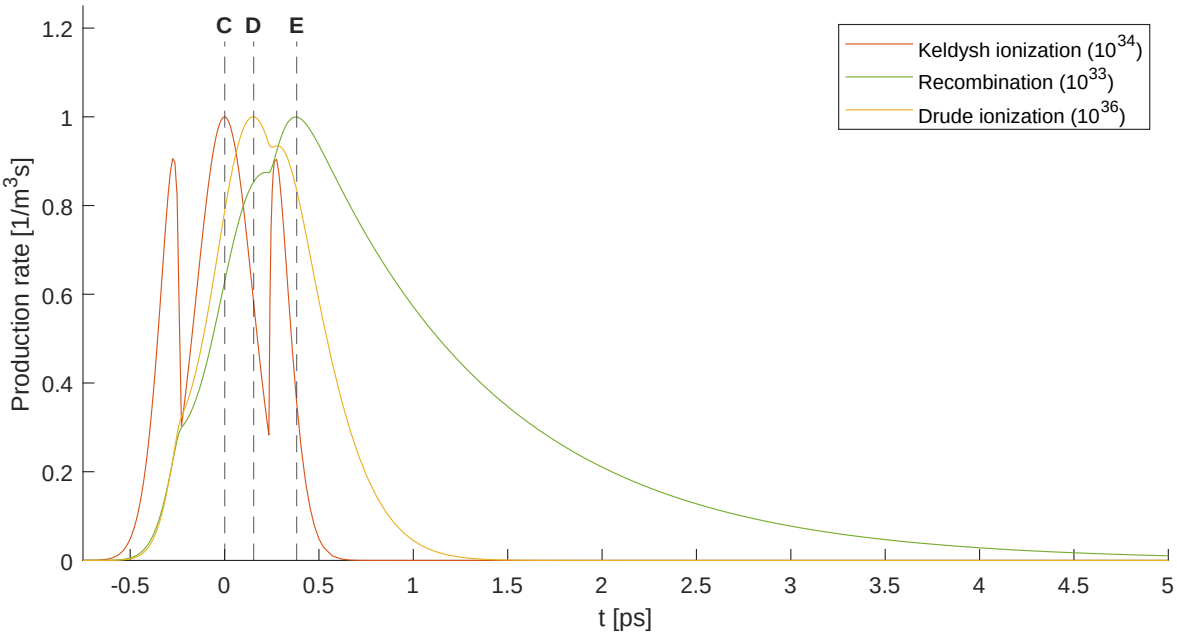

Figure 5.6: Normalized Keldysh ionization (P_{pi}), Drude ionization (P_{abs}) and recombination (L_{rec}) response to intensity (I) and free electron density (n_e) at $(0, z_f)$, reaching maximum at C, D and E respectively.

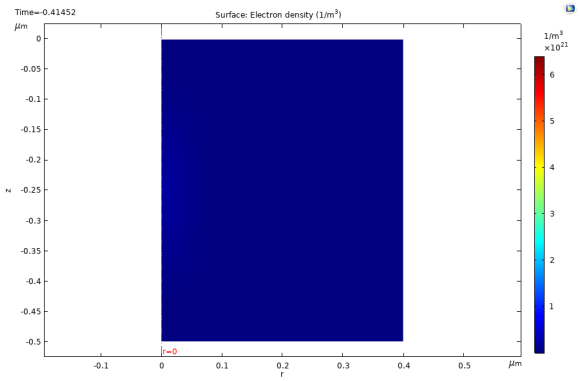

(a) $t = -0.4$[ps].

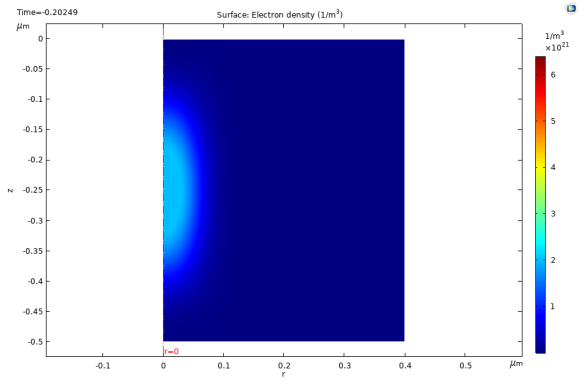

(b) $t = -0.2$[ps].

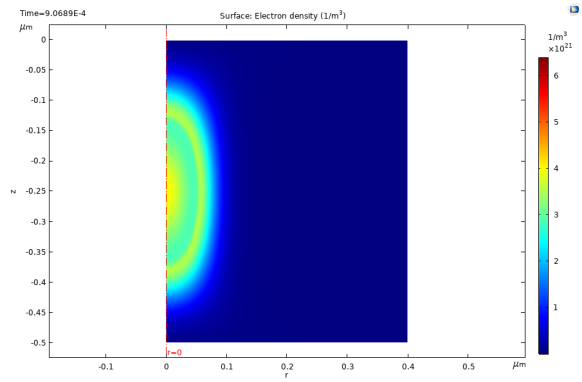

(c) $t = 0$[ps].

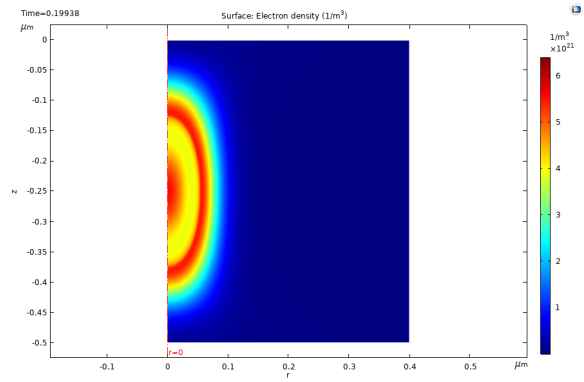

(d) $t = 0.2$[ps].

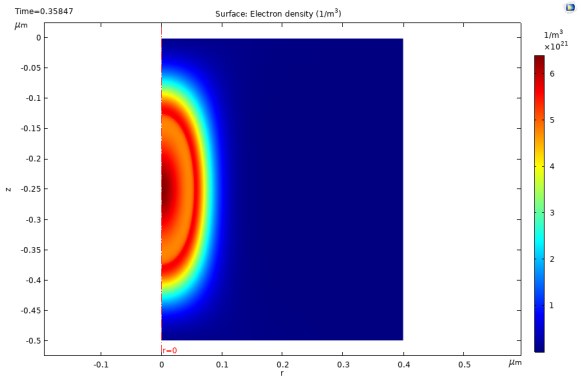

(e) $t = -0.35$[ps].

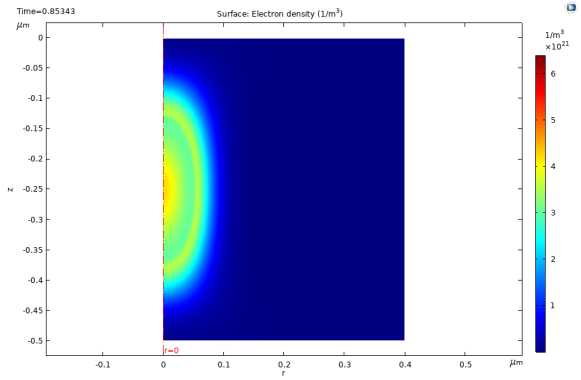

(f) $t = 0.85$[ps].

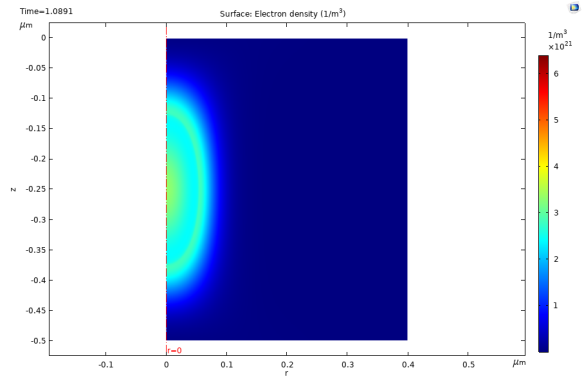

(g) $t = 1$[ps].

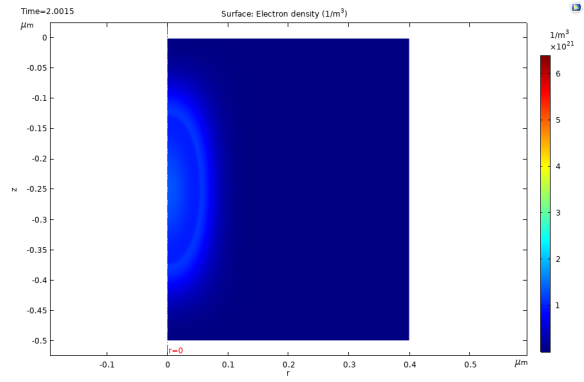

(h) $t = 2$[ps].

Figure 5.7: Free electron density (n_e) distribution in time, low energy pulse ($E_p = 0.025$[µJ]).

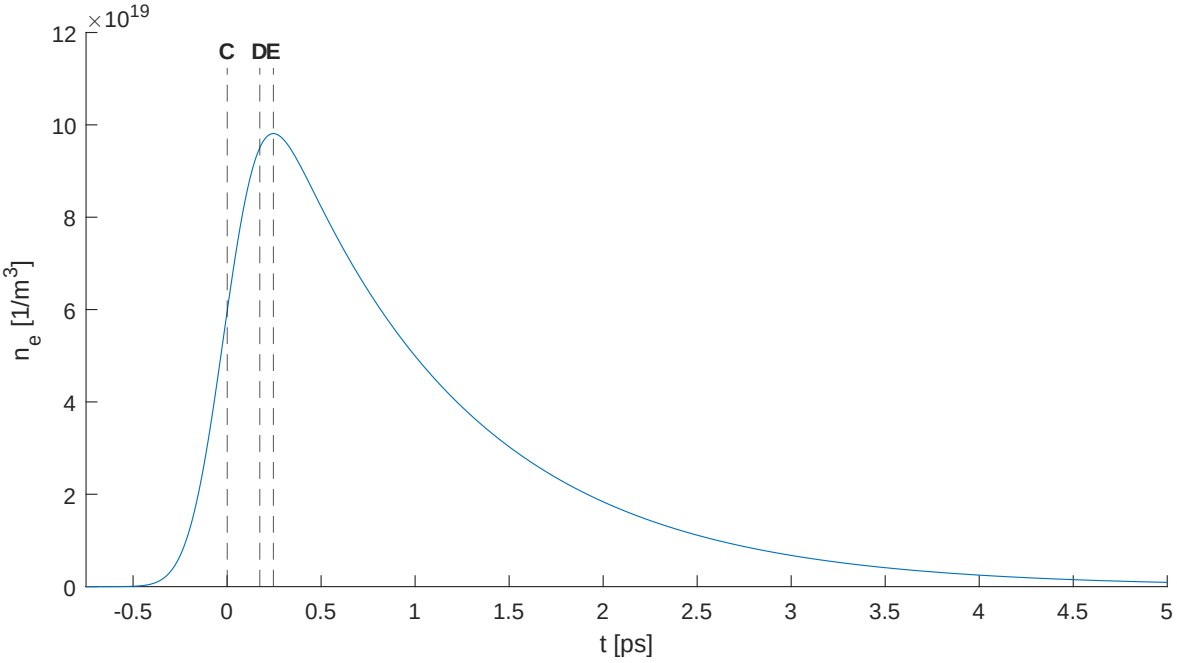

Figure 5.8: Normalized Keldysh ionization (P_{pi}), Drude ionization (P_{abs}) and recombination (L_{rec}) response to intensity (I) and free electron density (n_e) at top surface $(0, 0)$, reaching maximum at C, D and E respectively.

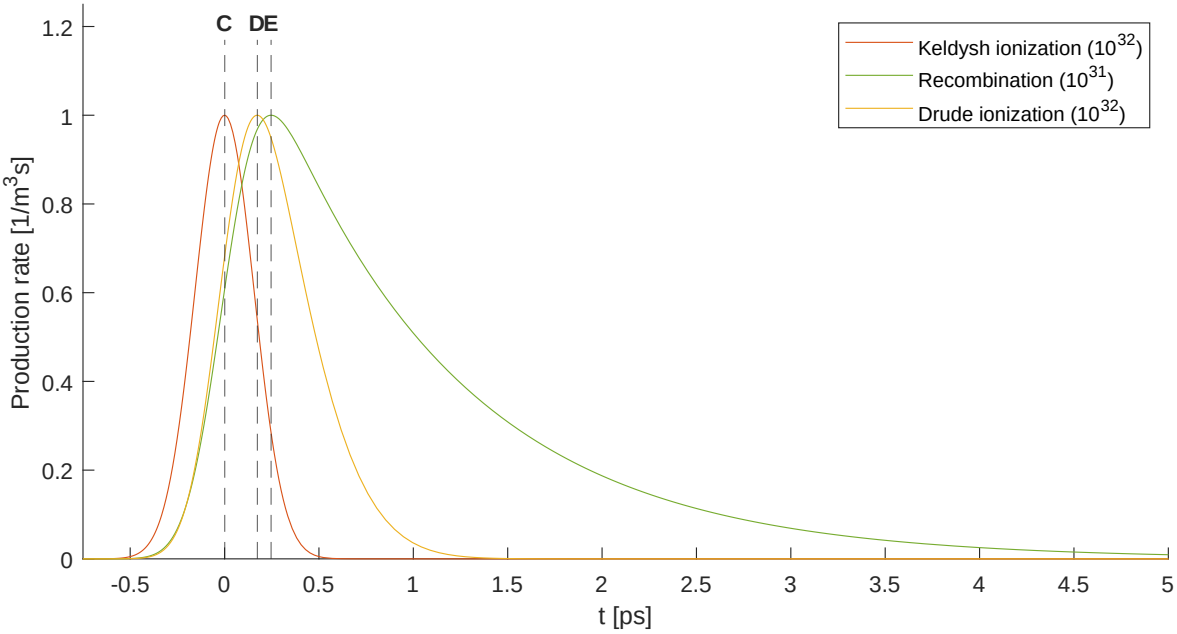

Figure 5.9: Free electron density (n_e) due to Keldysh ionization (P_{pi}), Drude ionization (P_{abs}) and recombination (L_{rec}) at top surface $(0, 0)$, reaching maximum at C, D and E respectively.

Free electron temperature distribution

The energy absorbed due to multiphoton ionization and free electron absorption promotes electrons, increasing their kinetic energy. The increase in kinetic energy, characterized as electron temperature, coincides with the increase in free electron density, yet continues to increase as opposed to the decrease in density, see Figures 5.5 and 5.10.

The energy is contained in the domain and redistributes rapidly, caused by carrier-carrier interaction and diffusion, resulting in an uniform distribution of electron temperature in the domain, see Figure 5.12.

The boundary conditions have minimal effect on the free electron temperature, as the diffusion is dependent on the (local) free electron density, which is minimal at the boundaries, see Figure 5.7.

Lattice temperature distribution

The two-temperature model describes energy exchange between electrons and phonons and is the only phenomena reducing the free electron temperature, increasing the lattice temperature. The electron-phonon coupling coefficient (G_{TTM}) connects the electron and lattice temperatures and the coupling coefficient is dependent on the local electron density. Therefore, the resulting lattice temperature distribution is similar to the free electron density distribution, see Figures 5.7 and 5.13.

It is no surprise that the lattice temperature effect trails behind the free electron density and increasing electron temperature, resulting in a delayed response in the lattice. Heat conduction effects occur in the domain, diffusing the lattice temperature, see Figures 5.13g and 5.13h, where the lattice temperature of the ring, induced by the free electron density ring, and of the focus consolidate gradually.

5.2.2 High pulse energy - plasma formation

Unfortunately, the studies using high pulse energy, $0.05 \leq E_p \leq 0.075$[μJ], did not converge due to large gradients locally, affecting subsequent model behaviour. However, the simulation scenarios maintained stability after $t = 0$[ps], which is after the time instance of the pulse peak, unlike studies performed by de Zeeuw [22].

To clearly show model behaviour two scenarios are presented, resulting in high intensity distribution. A pulse energy of 0.05[μJ], stable until $t = 1.9$[ps] and 0.06[μJ] stable until $t = 0.35$[ps]. The second scenario shown did not complete the FWHM pulse, $t < 0.5$[ps], due to higher input energy, yet displays the physical behaviour more clearly, in a larger area in the modeled domain. For all scenarios the intensity, free electron density, free electron temperature and lattice temperature behaviour is similar, presenting the relevant figures and graphs below.

Intensity distribution

The propagation of the laser intensity is spatially equivalent to the low intensity profile, see Figure 5.1. The pulse energy is higher, triggering absorption effects that lead to electron shielding, see Figures 5.14d, 5.15b, 5.15c and 5.15d.

Electron shielding occurs due to plasma formation, when sufficient free electrons are generated a plasma forms, consisting of the free electrons, Al^{3+} and O^{2-} ions. The free electrons absorb the incoming photons from the laser beam via free electron absorption, the photons are unable to pass through the plasma, thus shielding the material below from the incident laser light [59,60].

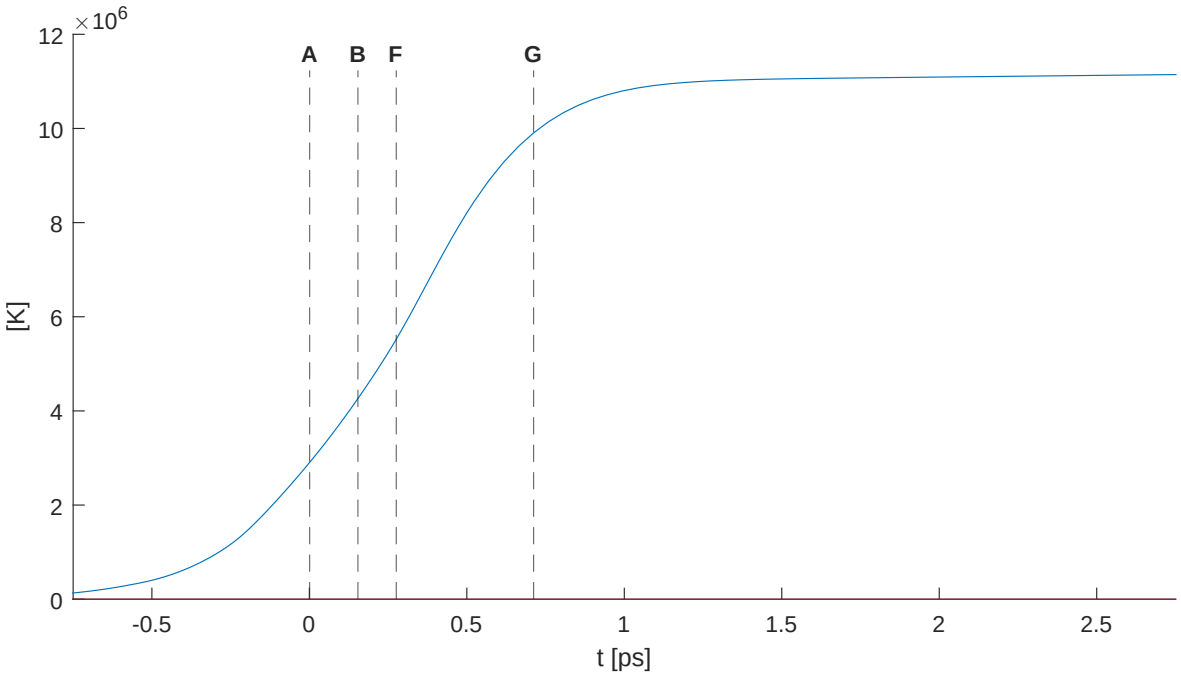

Figure 5.10: Free electron temperature (T_e) due to multiphoton ionization (S_{mpi}), free electron absorption (S_{abs}), carrier-carrier interaction (CC) and two-temperature exchange (L_{TTM}) at $(0, z_f)$, reaching maximum at A, B, F and G respectively.

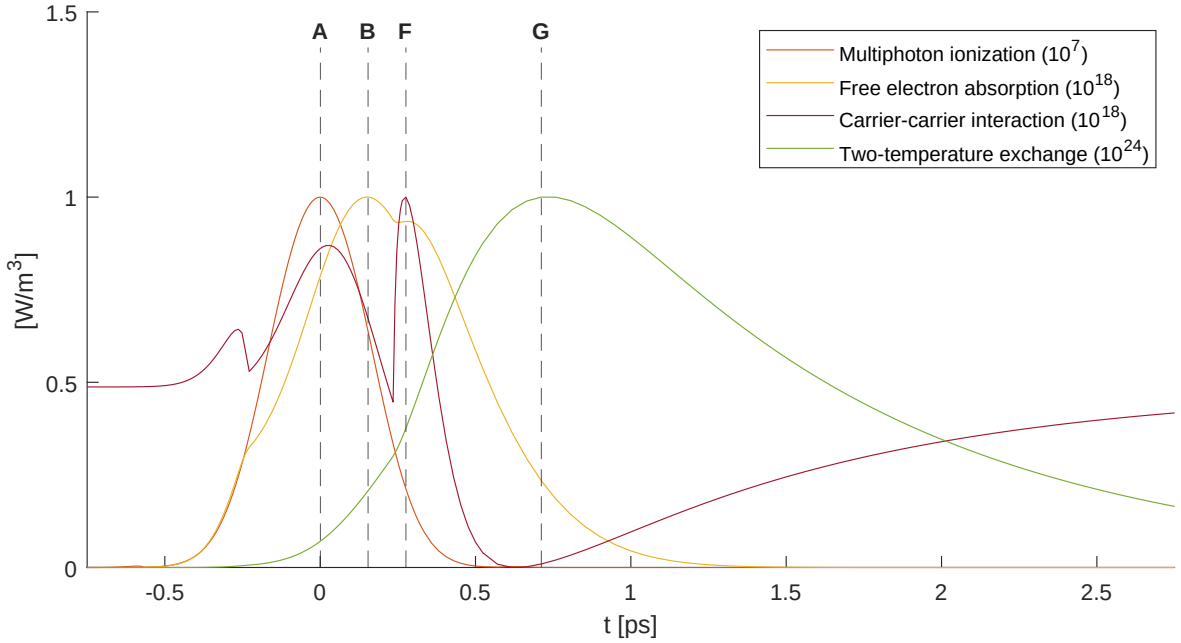

Figure 5.11: Normalized multiphoton ionization (S_{mpi}), free electron absorption (S_{abs}), carrier-carrier interaction (CC) and two-temperature exchange (L_{TTM}) response to all variables at $(0, z_f)$, reaching maximum at A, B, F and G respectively.

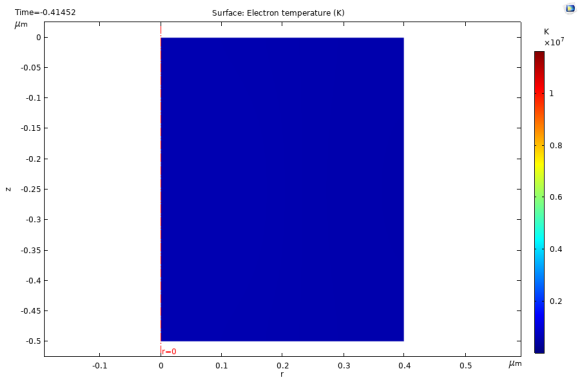

(a) $t = -0.4$[ps].

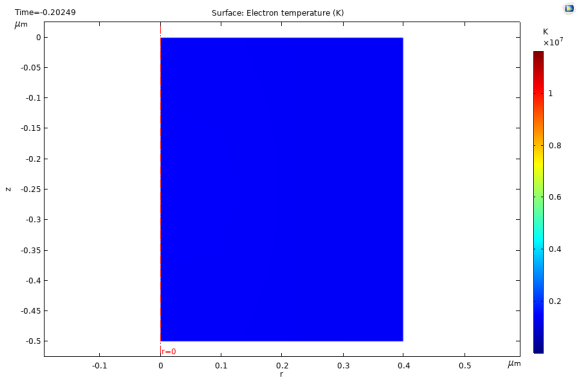

(b) $t = -0.2$[ps].

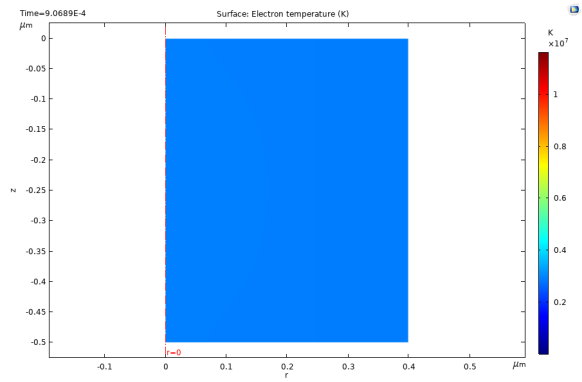

(c) $t = 0$[ps].

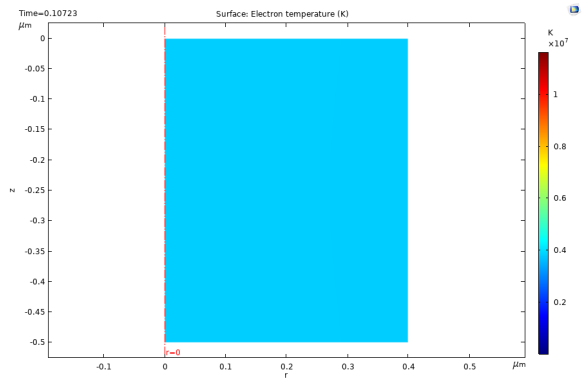

(d) $t = 0.2$[ps].

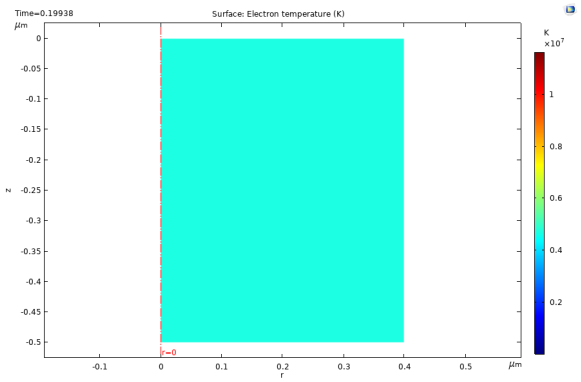

(e) $t = -0.35$[ps].

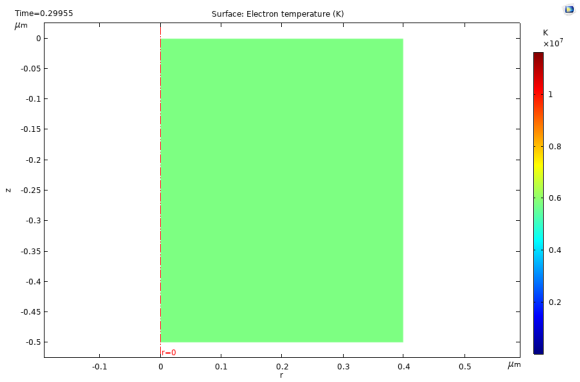

(f) $t = 0.85$[ps].

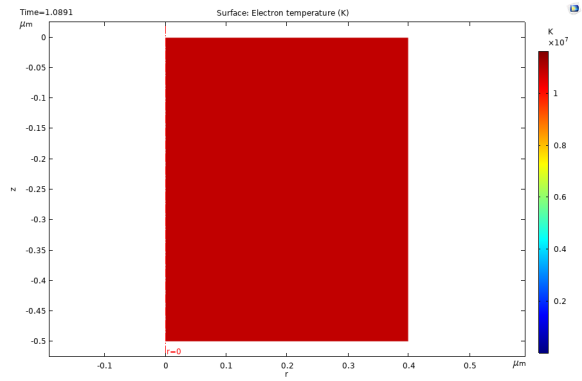

(g) $t = 1$[ps].

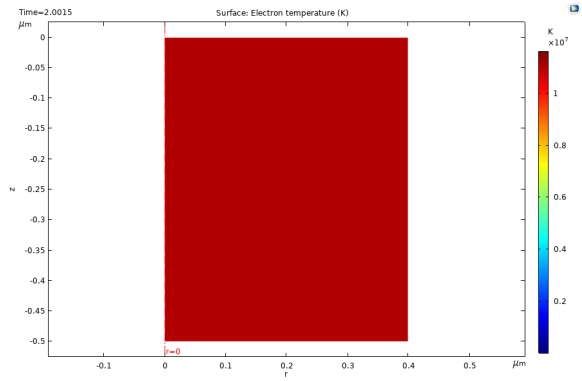

(h) $t = 2$[ps].

Figure 5.12: Free electron temperature (T_e) in time, low energy pulse ($E_p = 0.025$[µJ]).

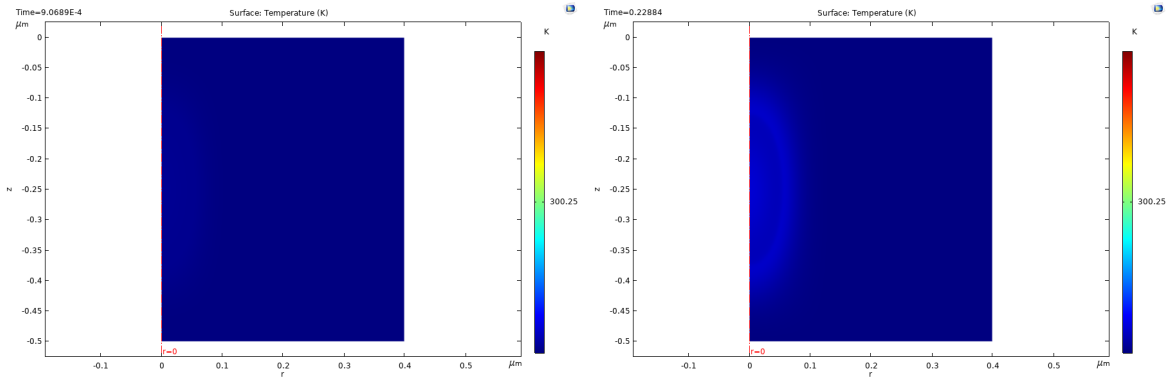

(a) $t = 0$[ps]. *(b)* $t = 0.2$[ps].

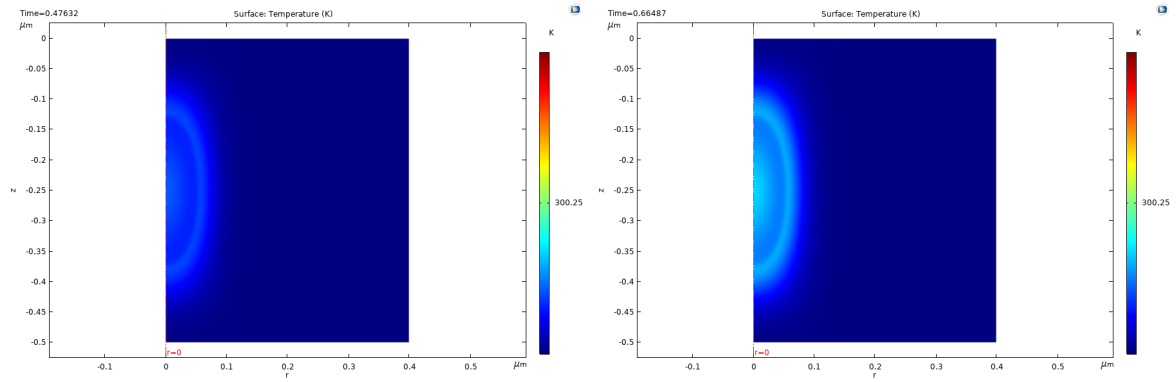

(c) $t = 0.45$[ps]. *(d)* $t = 0.65$[ps].

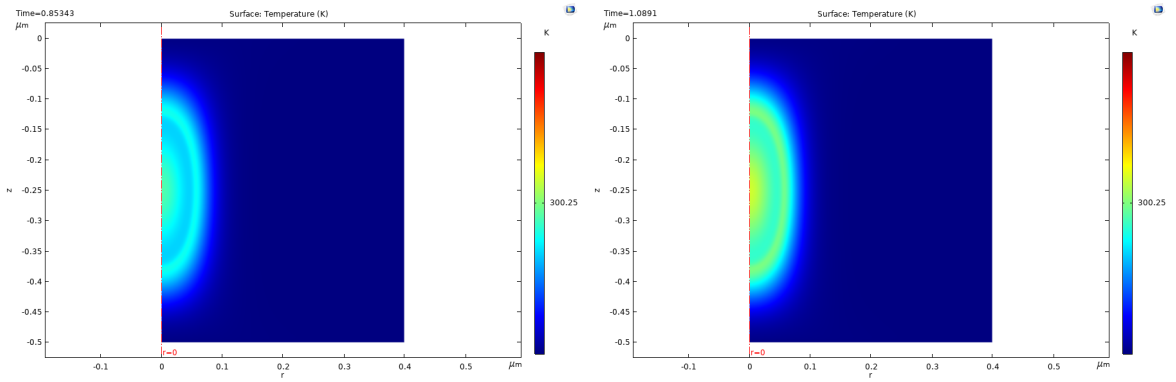

(e) $t = 0.85$[ps]. *(f)* $t = 1$[ps].

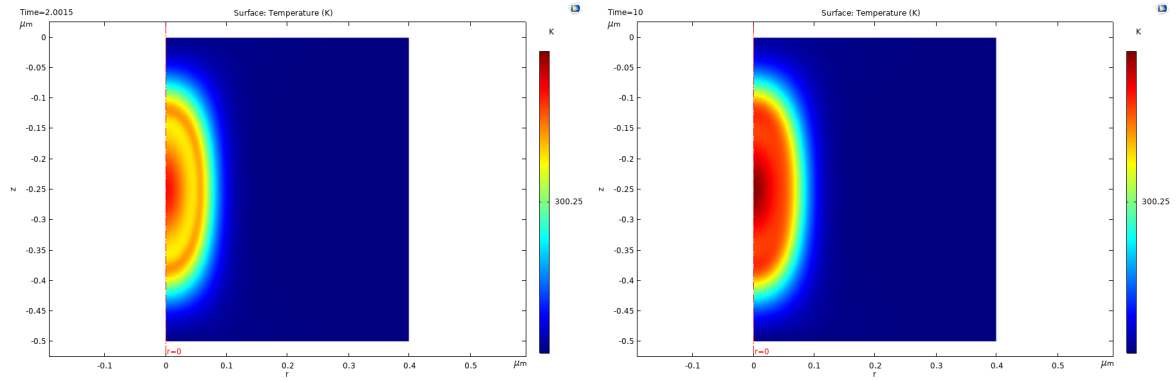

(g) $t = 2$[ps]. *(h)* $t = 10$[ps].

Figure 5.13: Lattice temperature (T_l) distribution in time, low energy pulse ($E_p = 0.025$[µJ]).

The intensity peaks at $1 \cdot 10^{17}$[W/m^2], reaching the regime of tunneling ionization in the Keldysh ionization framework, clearly displaying ”saw-like” behaviour and symmetry due to dependence of the Keldysh ionization on the intensity, see Figures 2.6 and 5.17. Again, the influence of multiphoton ionization on absorption is minimal, yet initiates free electron absorption, leading to strong absorption effects.

The effect of electron shielding is brought on by strong free electron absorption, as exceedingly more photons are absorbed by free electron. The increasing number of free electrons leads to more impact events, evolving into avalanche ionization rapidly increasing free electron density, creating a reinforced effect absorbing all of the incident pulse energy, see Figures 5.17 and 5.22.

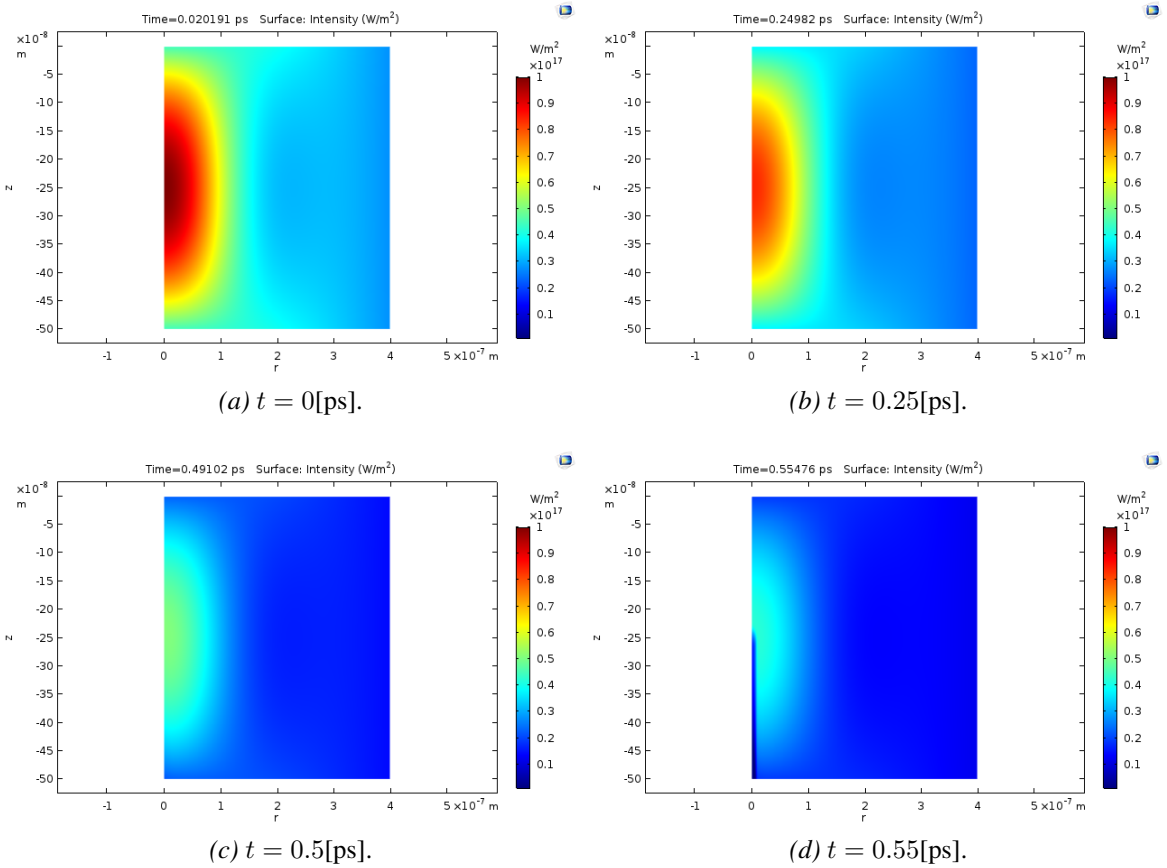

(a) $t = 0$[ps]. *(b)* $t = 0.25$[ps].

(c) $t = 0.5$[ps]. *(d)* $t = 0.55$[ps].

Figure 5.14: Intensity (I) distribution in time, high energy pulse ($E_p = 0.05$[µJ]).

The effect of electron shielding is more apparent for higher pulse energies, see Figure 5.15, where the shielding effect develops during the second half of the FWHM pulse time, $t > 0$[ps]. The ”saw-like” behaviour of the Keldysh framework and the complete absorption of pulse energy by free electron absorption occurs earlier and more strongly due to higher intensity and resultant accelerated production of free electrons, see Figures 5.20 and 5.21.

Free electron density distribution

The production rate of free electrons at the focal point is substantial compared to the surrounding material, see Figures 5.16a and 5.19a, shaped similarly to the initial low intensity free electron distribution, see Figure 5.7b.

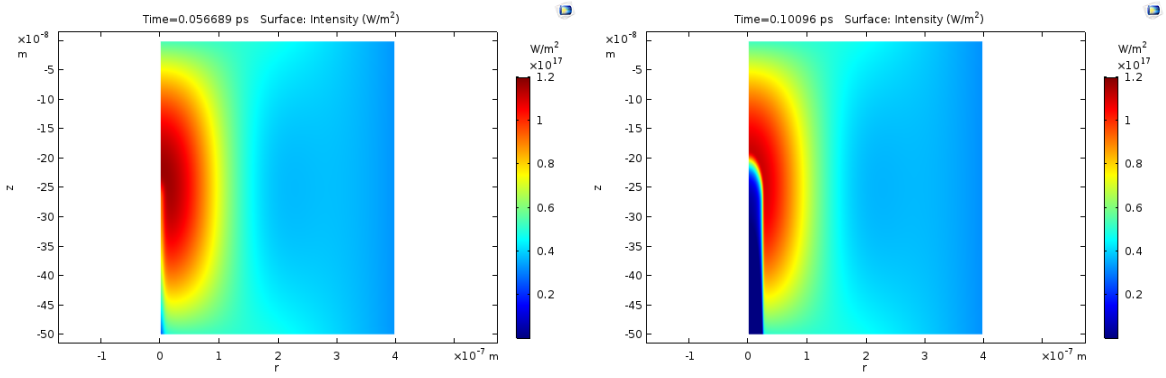

(a) $t = 0.05$[ps]. *(b)* $t = 0.1$[ps].

(c) $t = 0.2$[ps]. *(d)* $t = 0.35$[ps].

Figure 5.15: Intensity (I) distribution in time, high energy pulse ($E_p = 0.06$[μJ]).

After $t = 0.5$[ps] the increase of free electron density generates a plasma of free electrons and ions, due to strong absorption effects, see Figure 5.23. The electrons in the plasma shield the material below from incident laser energy, whereas above the shield effects continue to increase, expanding and displacing the plasma region, see Figures 5.16b and 5.16c [59].

The electron density below the shield diminishes after $t = 1$[ps], see Figure 5.16d, as the incident intensity is blocked. Observed clearly in the focal region of the beam, the electron density reduces gradually according to the recombination time, see Figures 5.22 and 5.23.

For a pulse energy of 0.06[μJ], the effects of Keldysh ionization, avalanche ionization and recombination develop in rapid succession, see Figure 5.25. Clearly showing that Keldysh ionization decreases immediately due to electron shielding from the plasma. The free electron density reduction as a result of recombination occurs in the shielded area, yet is concealed by the dominating behaviour of increasing electron production in the focal point, see Figures 5.19, 5.24 and 5.25, until $t = 0.1$[ps], when recombination determines the electron density.

Free electron temperature distribution

Similarly to the low intensity pulse, see Figure 5.12, the diffusion of free electron temperature results in an uniform distribution of electron temperature for both 0.05[μJ] and 0.06[μJ]. The local differences are minimal and remain constant in shape, the free electron temperature in the focal point remains highest, as the temperature in the domain rises, see Figures 5.26a and 5.26b.

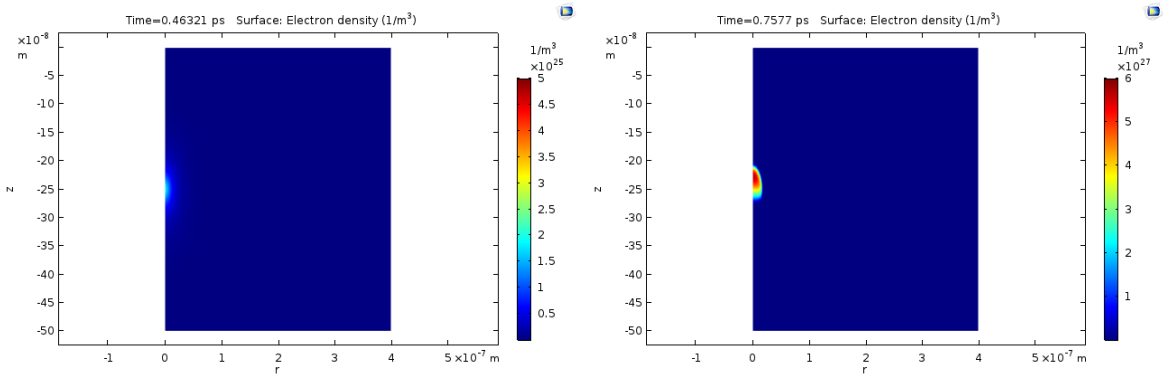

(a) $t = 0.5$[ps]. *(b)* $t = 0.75$[ps].

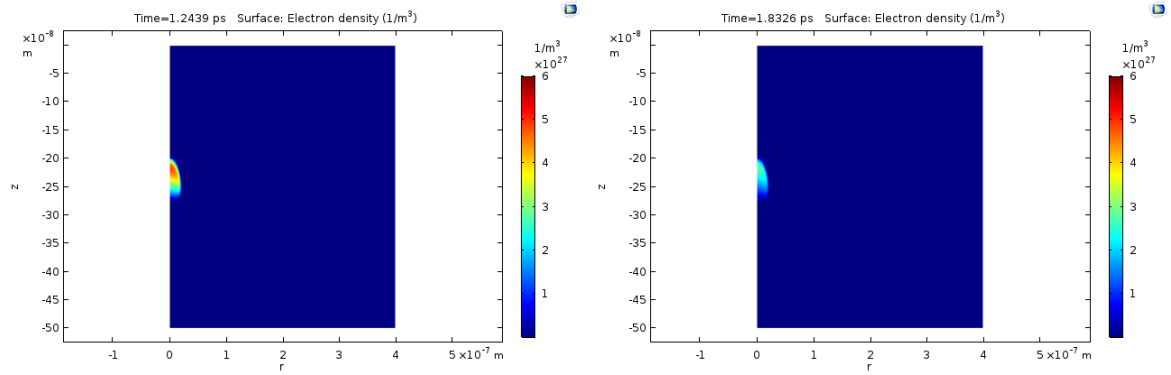

(c) $t = 1.25$[ps]. *(d)* $t = 1.8$[ps].

Figure 5.16: Free electron density (n_e) distribution in time, high energy pulse ($E_p = 0.05$[µJ]).

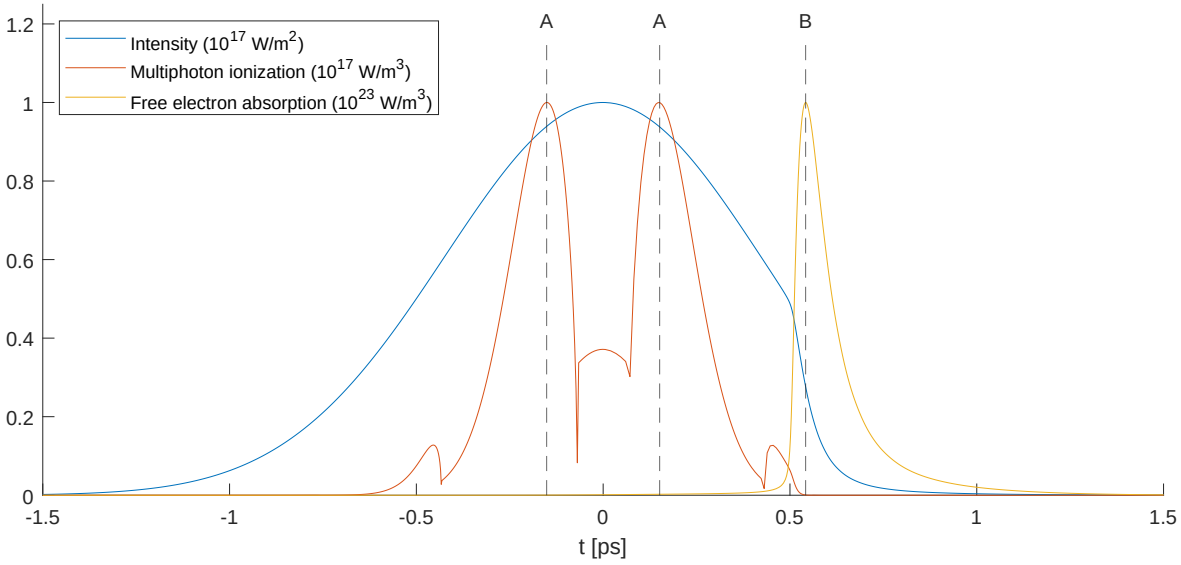

Figure 5.17: Normalized multiphoton ionization (L_{mpi}) and free electron absorption (L_{abs}) response to intensity (I) at $(0, z_f)$, reaching maximum at B and C respectively ($E_p = 0.05$[µJ]).

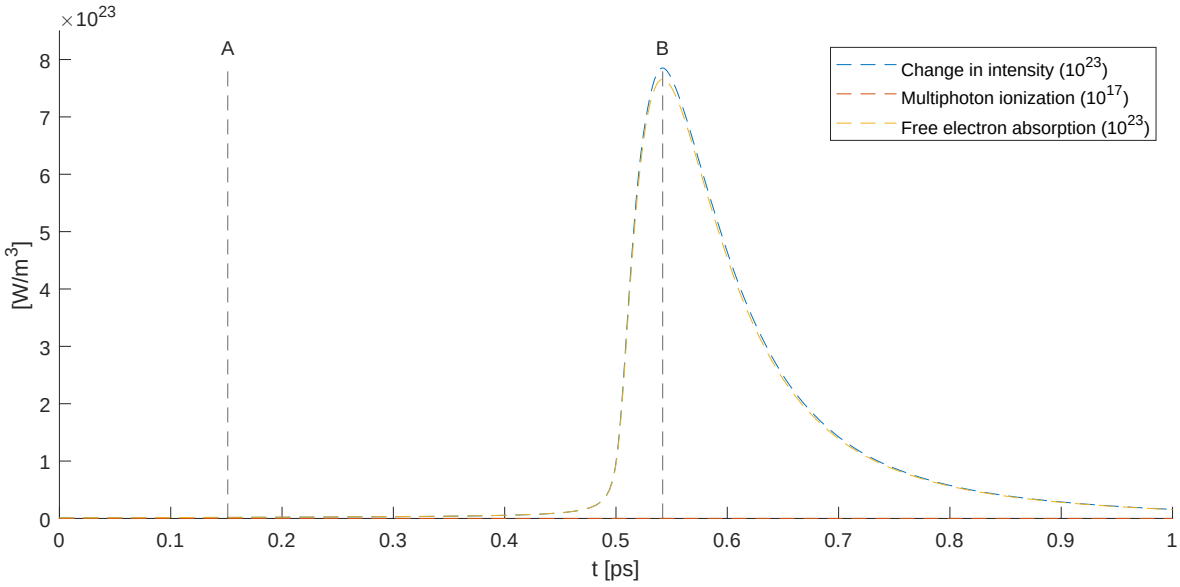

Figure 5.18: Effects of multiphoton ionization (L_{mpi}) and free electron absorption (L_{abs}) on the intensity (I) at $(0, z_f)$, reaching maximum at B and C respectively ($E_p = 0.05$[µJ]).

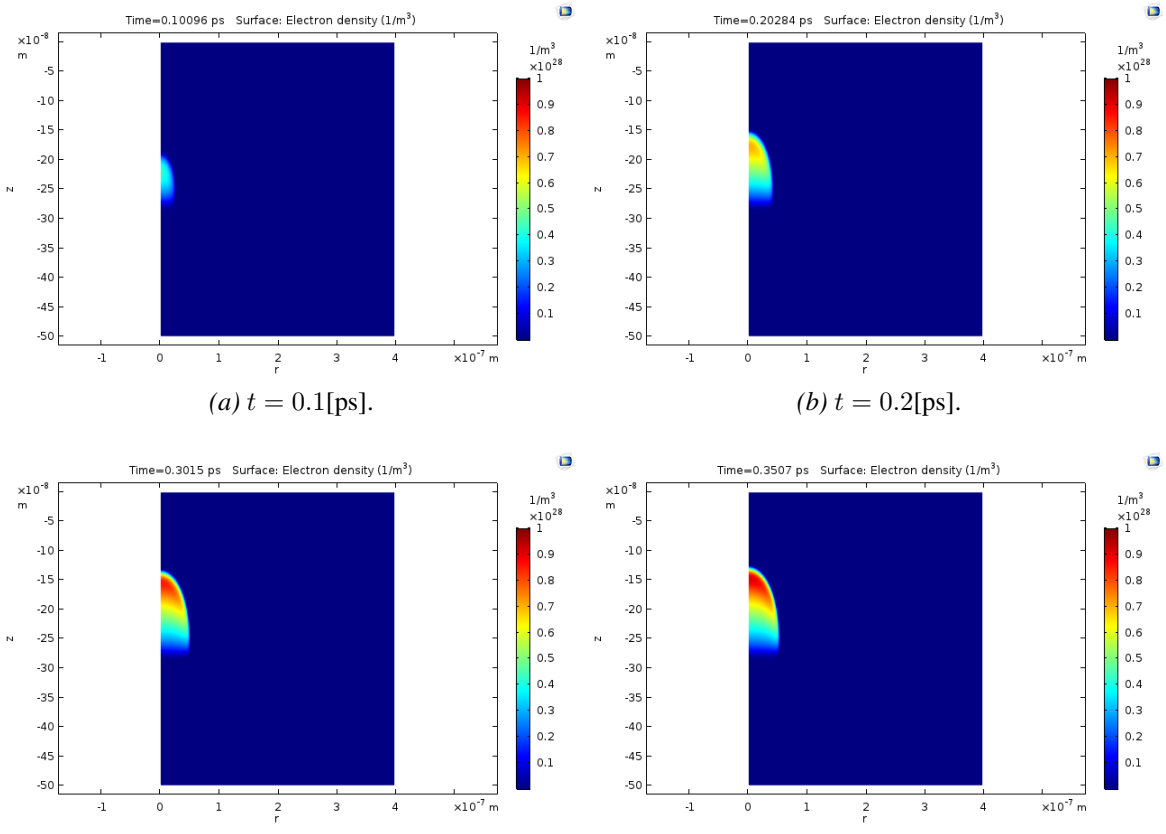

(a) $t = 0.1$[ps]. *(b)* $t = 0.2$[ps].

(c) $t = 0.3$[ps]. *(d)* $t = 0.35$[ps].

Figure 5.19: Free electron density (n_e) distribution in time, high energy pulse ($E_p = 0.06$[µJ]).

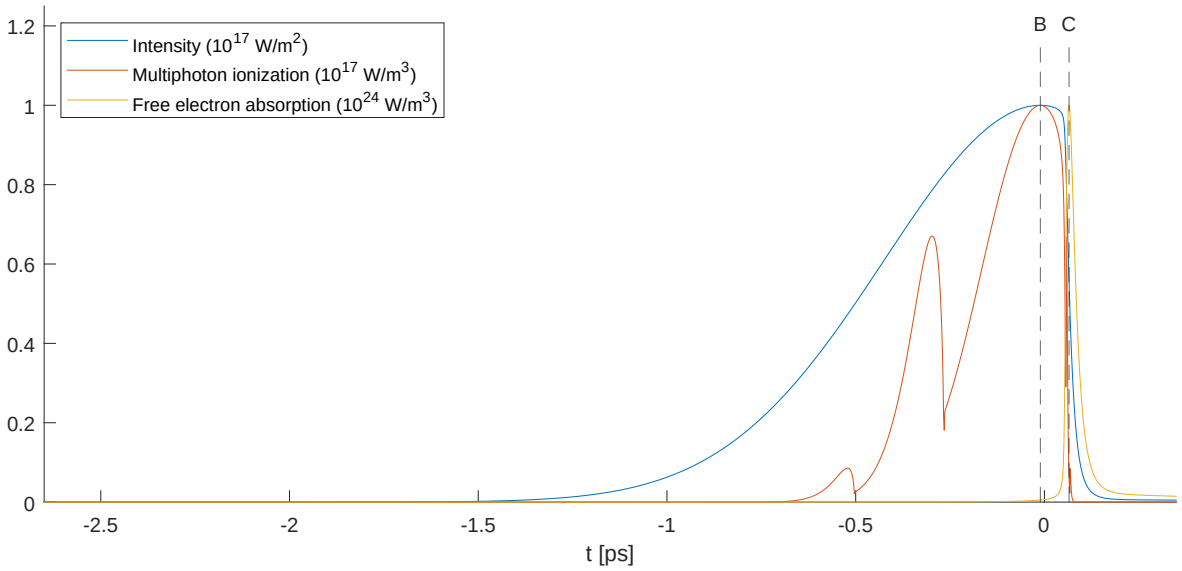

Figure 5.20: Normalized multiphoton ionization (L_{mpi}) and free electron absorption (L_{abs}) response to intensity (I) at $(0, z_f)$, reaching maximum at B and C respectively ($E_p = 0.06$[µJ]).

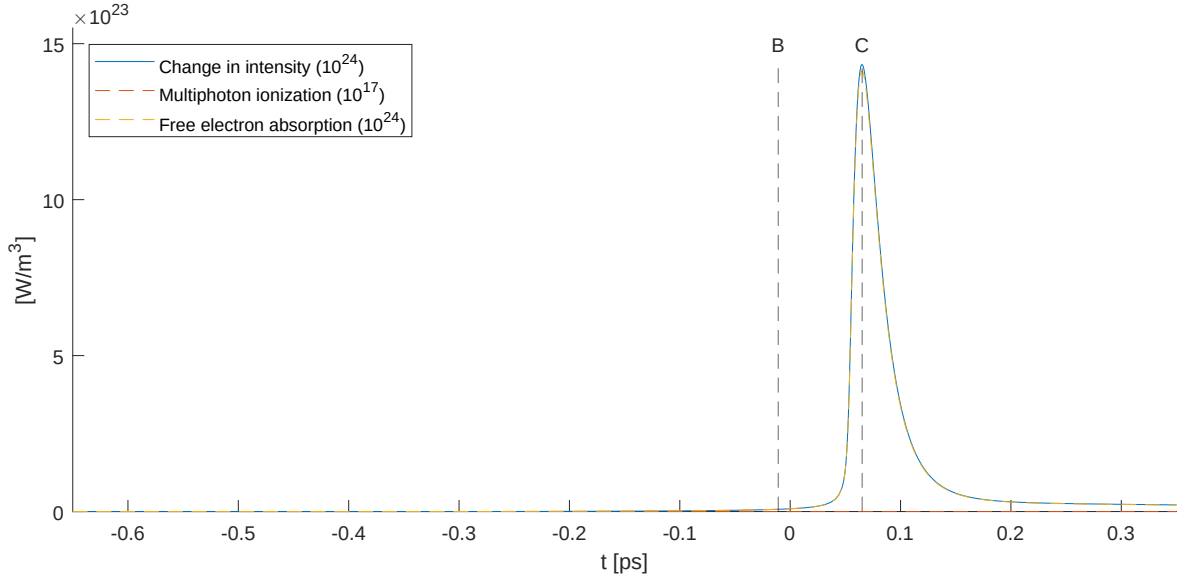

Figure 5.21: Effects of multiphoton ionization (L_{mpi}) and free electron absorption (L_{abs}) on the intensity (I) at $(0, z_f)$, reaching maximum at B and C respectively ($E_p = 0.06$[µJ]).

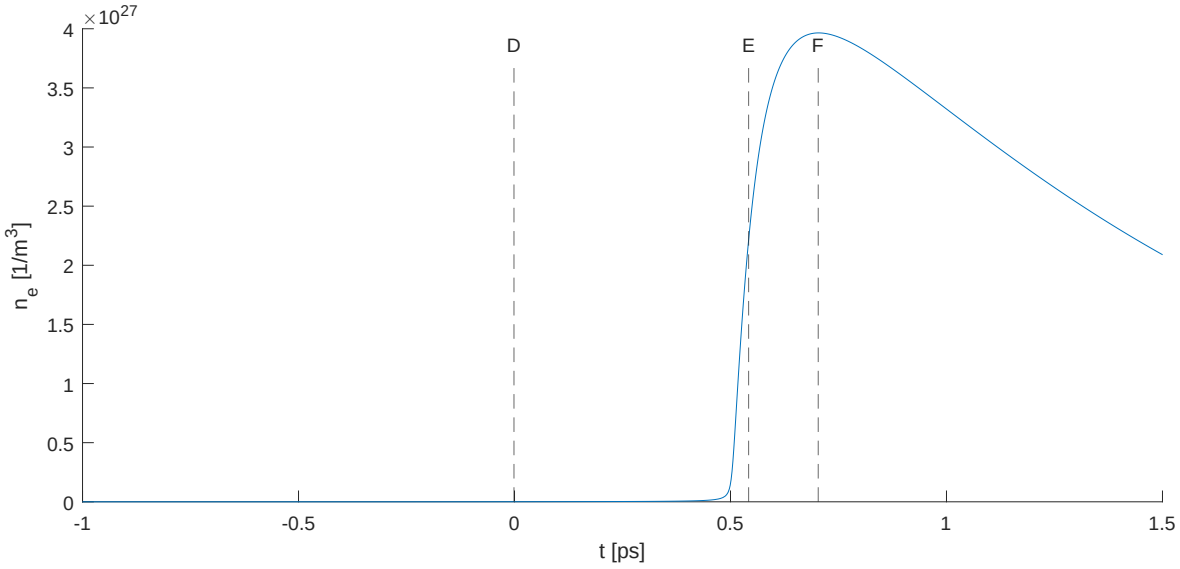

Figure 5.22: Free electron density (n_e) due to Keldysh ionization (P_{pi}), Drude ionization (P_{abs}) and recombination (L_{rec}) at $(0, z_f)$, reaching maximum at D, E and F respectively ($E_p = 0.05$[µJ]).

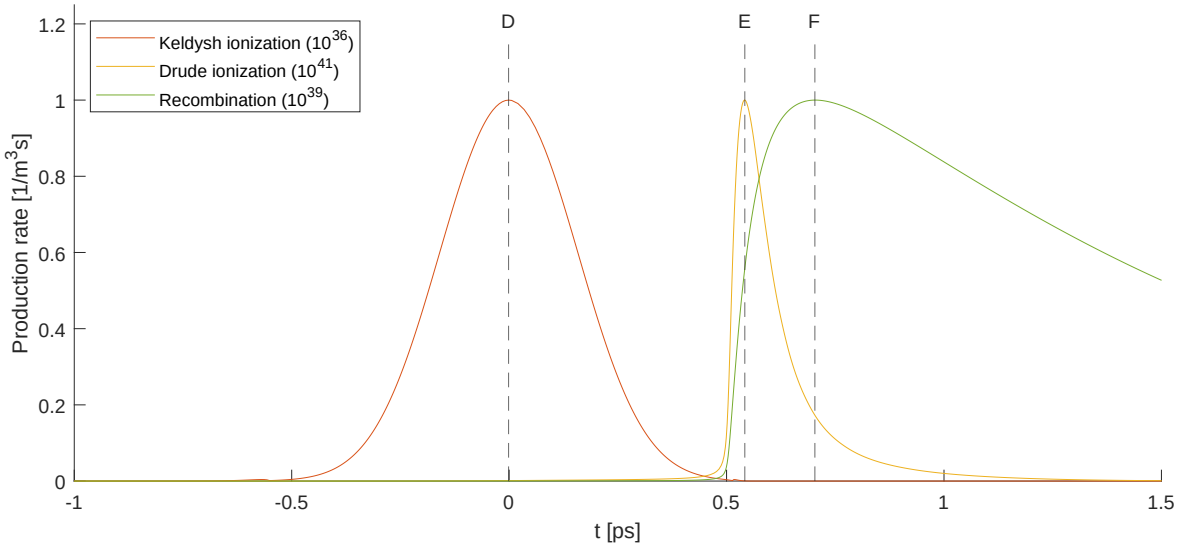

Figure 5.23: Normalized Keldysh ionization (P_{pi}), Drude ionization (P_{abs}) and recombination (L_{rec}) response to intensity (I) and free electron density (n_e) at $(0, z_f)$, reaching maximum at D, E and F respectively ($E_p = 0.05$[µJ]).

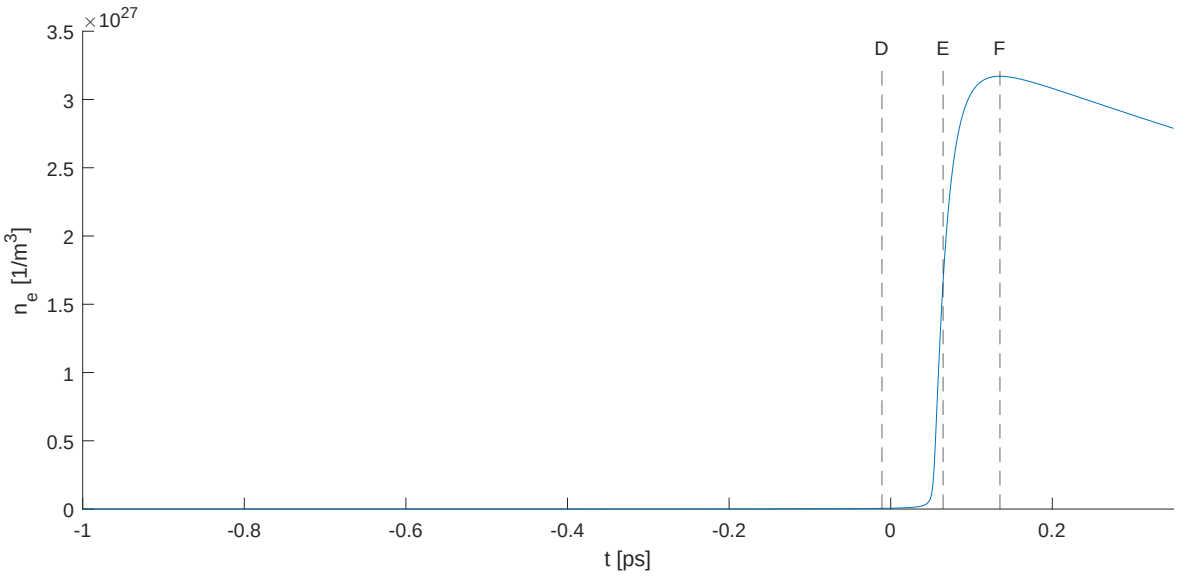

Figure 5.24: Free electron density (n_e) due to Keldysh ionization (P_{pi}), Drude ionization (P_{abs}) and recombination (L_{rec}) at $(0, z_f)$, reaching maximum at D, E and F respectively ($E_p = 0.06$[µJ]).

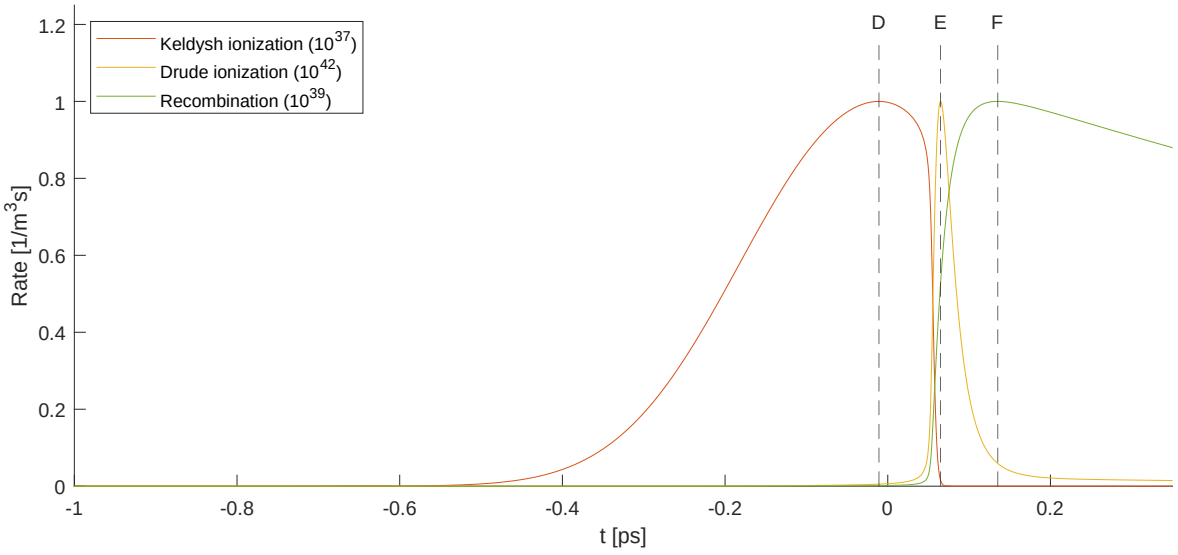

Figure 5.25: Normalized Keldysh ionization (P_{pi}), Drude ionization (P_{abs}) and recombination (L_{rec}) response to intensity (I) and free electron density (n_e) at $(0, z_f)$, reaching maximum at D, E and F respectively ($E_p = 0.06$[µJ]).

Yet, when the two-temperature exchange is triggered the temperature in the focus decreases, see Figure 5.26c. As the exchange between the electrons and phonons in and around the focal point continues, the free electron temperature reduces further, leading to a higher electron temperature outside the high intensity region, see Figures 5.15 and 5.26d until 5.26g.

The phenomena affecting the free electron temperature occur in a different sequence compared to the low intensity, see Figures 5.11, 5.28 and 5.30. The rapid increase in free electron density causes carrier-carrier interaction to occur before free electron density becomes significant, shaping the electron distribution before electron shielding blocks the intensity.

However, multiphoton ionization diminishes when free electron absorption starts to dominate, continuing to increase the free electron temperature, after redistribution via carrier-carrier interaction and reduction via the two-temperature exchange. After the free electron absorption starts to diminish around $t = 0.07$[ps], the two-temperature exchange increases again, due to free electron temperature increasing, see Figures 5.27, 5.28, 5.29 and 5.30.

Lattice temperature distribution

As for low intensity, the exchange of energy between electrons and phonons via the two-temperature model is the source term for the lattice temperature, see Equation (2.7). The exchange is dependent on the electron-phonon coupling coefficient, shaping the lattice temperature, see Figures 5.31 and 5.32, according to the the free electron density distribution, see Figures 5.16 and 5.19.

In Figures 5.31b and 5.31a the temperature bar maximum is 500[K], showing lattice temperature profiles similar to the low pulse energy simulations, see Figure 5.13. Whereas for Figures 5.31c until 5.31h the temperature bar maximum is $4 \cdot 10^4$[K], the temperature distribution follows the shape of the electron shield, rapidly increasing the lattice temperature.

Again, the lattice temperature effects for a pulse energy of 0.05[µJ] are small compared to the domain. The effects are more clearly visible for the higher pulse energy of 0.06[µJ], shaped by a larger plasma region, see Figures 5.19 and 5.32, with high free electron density.

In the Figures 5.32a until 5.32c the maximum of the temperature bar is 350[K], for which the behaviour is similar, located in and around the focal point. For Figures 5.32h until 5.32h the temperature bar maximum is $1.1 \cdot 10^4$[K], shaped according to the free electron density distribution, trailing behind the generated electron shield, see Figure 5.19.

5.2.3 Higher pulse energy - domain limitations

When increasing the laser pulse energy further, ≥ 0.2[µJ], numerical convergence issues do not occur due to the intensity distribution extending beyond the domain. Yet, this allows for studying the (local) model behaviour after irradiation to determine the post-processing effects.

The higher pulse energy selected is 0.2[µJ], presenting notable behaviour for the intensity, free electron density, free electron temperature and lattice temperature is similar for all higher pulse energy scenarios.

Intensity distribution

Similarly to the low and high pulse energy scenarios the intensity distribution is spatially equivalent, see Figures 5.1, 5.2, 5.14 and 5.15. The difference between high and higher pulse energy is that the incident laser pulse increases the intensity in the domain rapidly, reaching a maximum of $1.9 \cdot 10^{17}$[W/m^2] in the focal point.

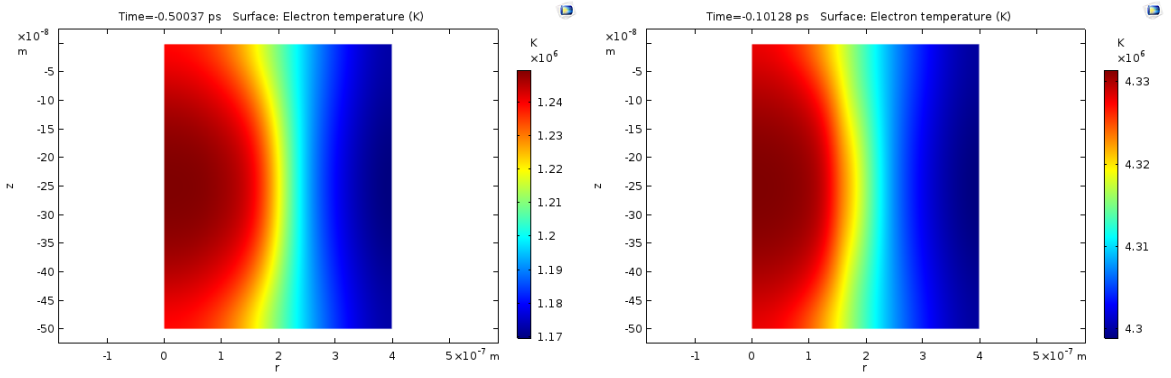

(a) $t = -0.5$[ps]. *(b)* $t = -0.1$[ps].

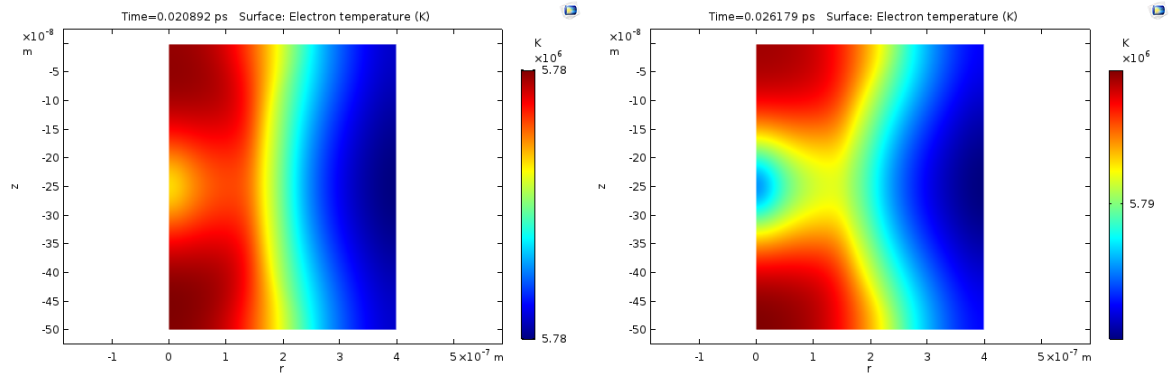

(c) $t = 0$[ps]. *(d)* $t = 0.025$[ps].

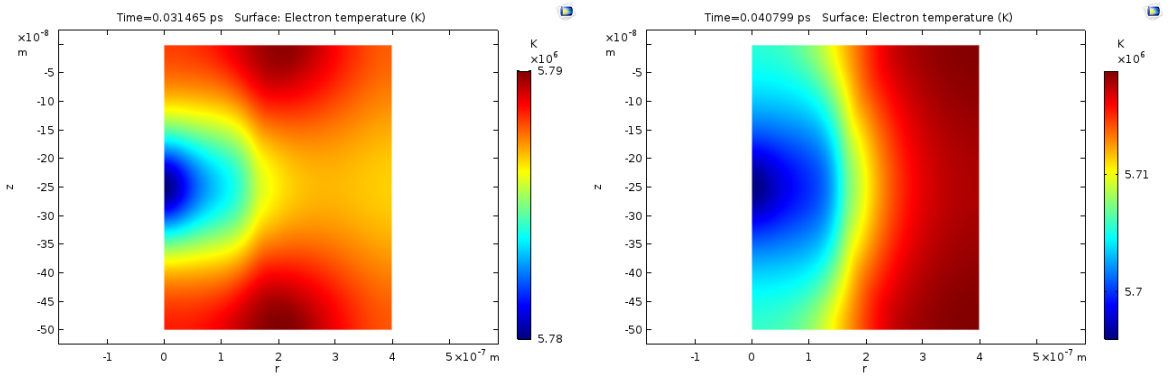

(e) $t = 0.03$[ps]. *(f)* $t = 0.04$[ps].

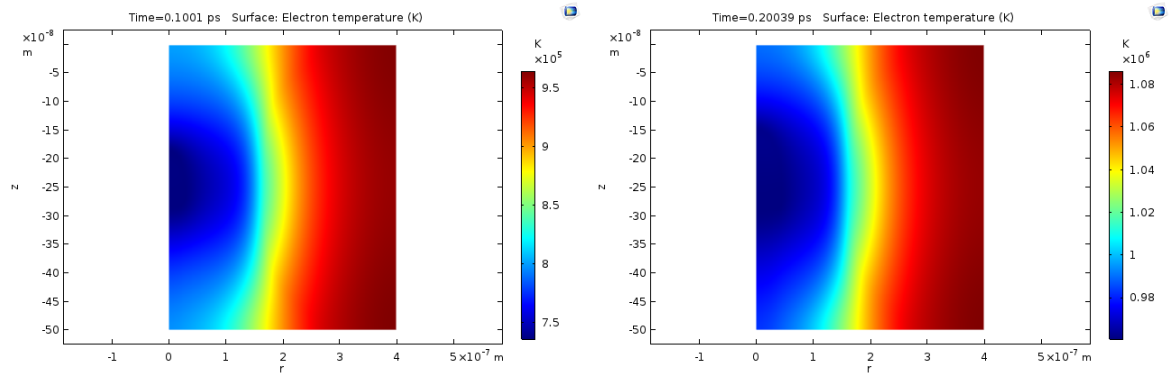

(g) $t = 0.1$[ps]. *(h)* $t = 0.2$[ps].

Figure 5.26: Local free electron temperature (T_e) distribution in time, high energy pulse ($E_p = 0.06$[μJ]).

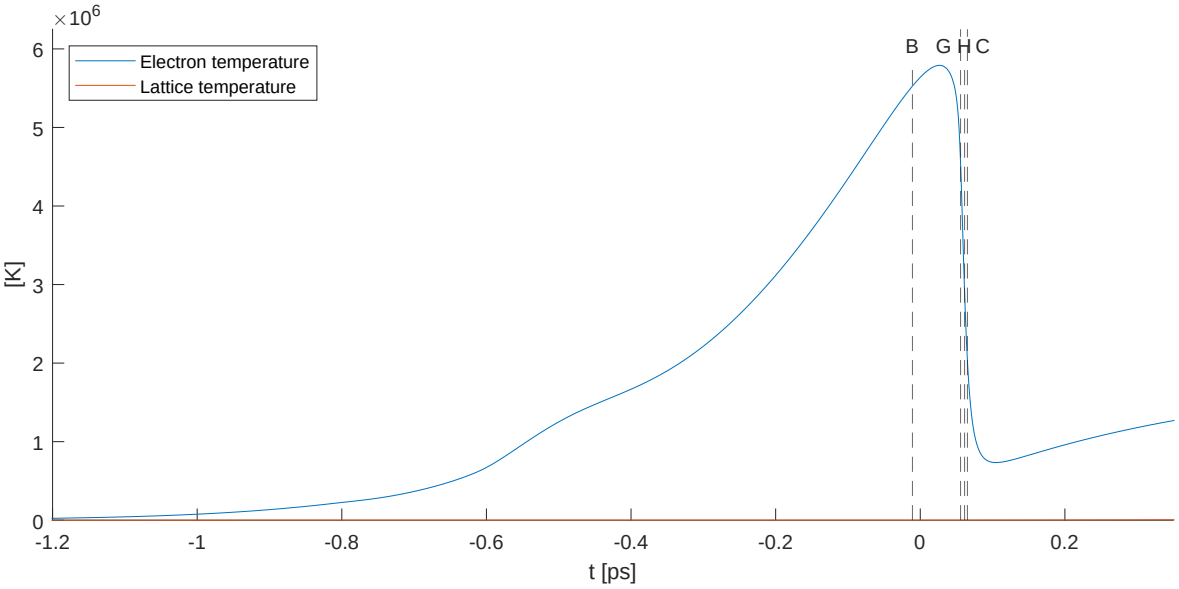

Figure 5.27: Free electron temperature (T_e) due to multiphoton ionization (S_{mpi}), free electron absorption (S_{abs}), carrier-carrier interaction (CC) and two-temperature exchange (L_{TTM}) at $(0, z_f)$, reaching maximum at B, C, G, H respectively ($E_p = 0.06$[µJ]).

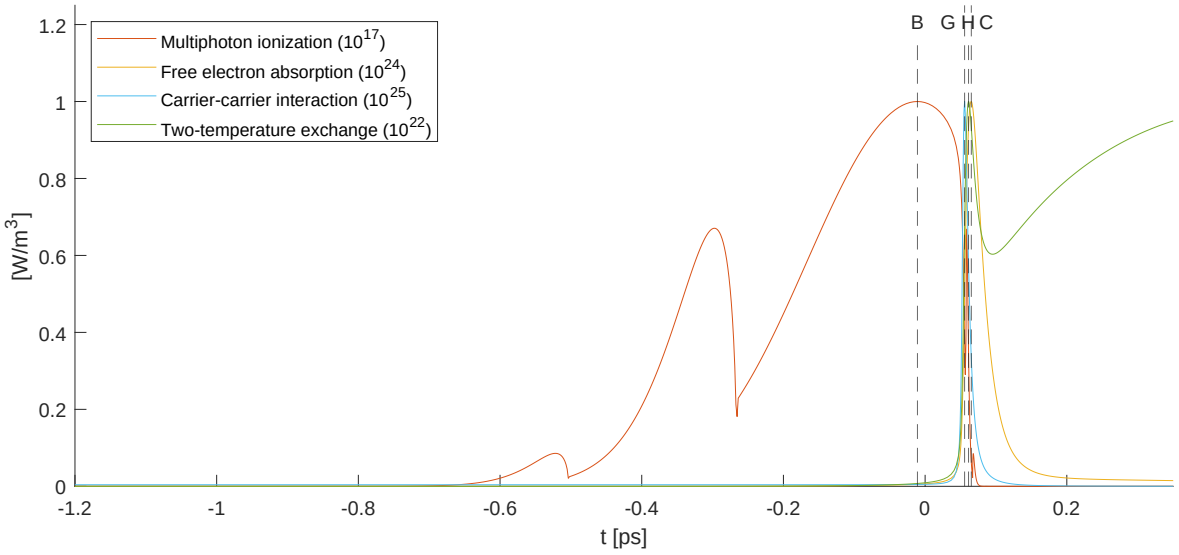

Figure 5.28: Normalized multiphoton ionization (S_{mpi}), free electron absorption (S_{abs}), carrier-carrier interaction (CC) and two-temperature exchange (L_{TTM}) to all variables at $(0, z_f)$, reaching maximum at B, C, G, H respectively ($E_p = 0.06$[µJ]).

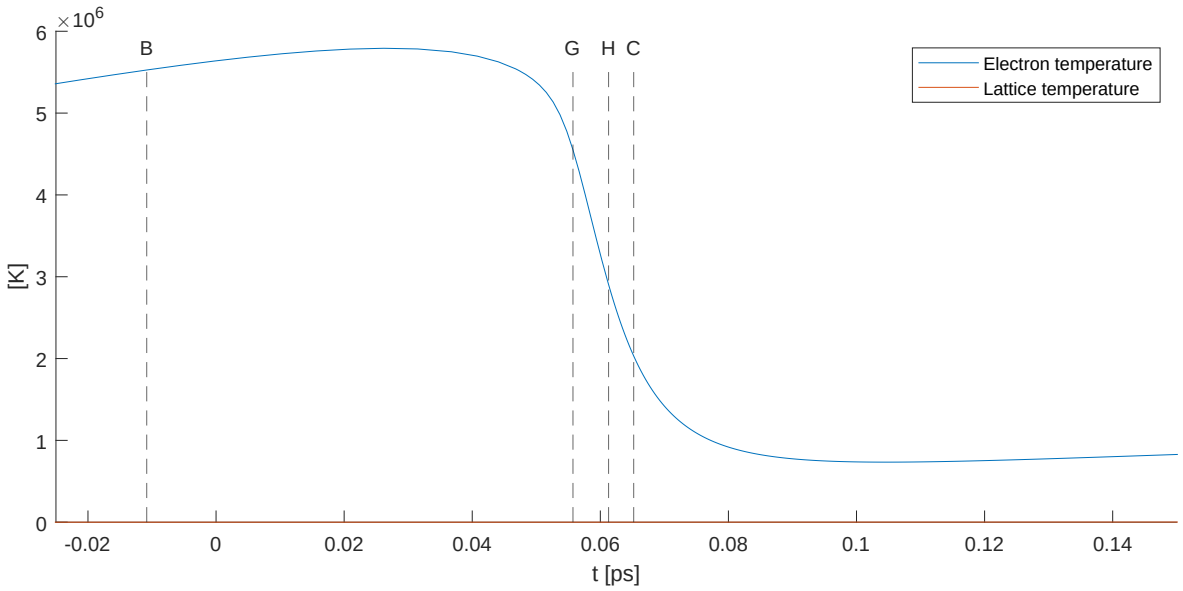

Figure 5.29: Free electron temperature (T_e) due to multiphoton ionization (S_{mpi}), free electron absorption (S_{abs}), carrier-carrier interaction (CC) and two-temperature exchange (L_{TTM}) at $(0, z_f)$, reaching maximum at B, C, G, H respectively ($E_p = 0.06$[µJ], detailed).

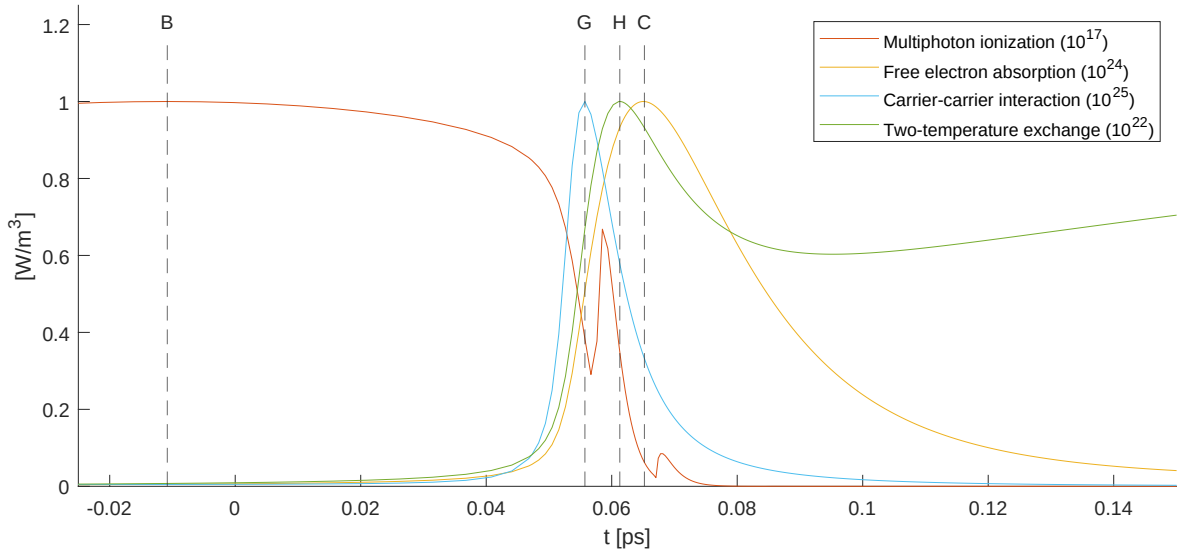

Figure 5.30: Normalized multiphoton ionization (S_{mpi}), free electron absorption (S_{abs}), carrier-carrier interaction (CC) and two-temperature exchange (L_{TTM}) to all variables at $(0, z_f)$, reaching maximum at B, C, G, H respectively ($E_p = 0.06$[µJ], detailed).

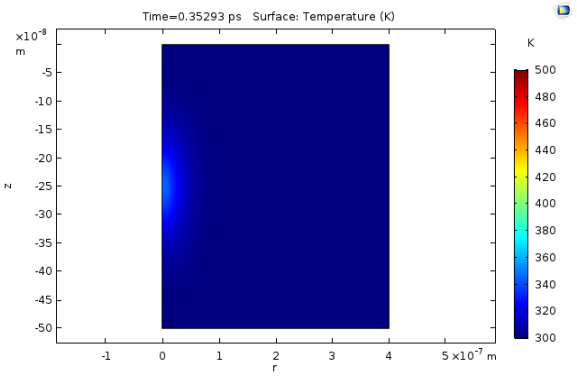

(a) $t = 0.35$[ps].

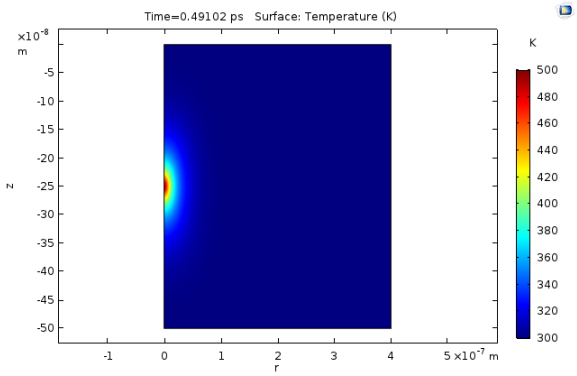

(b) $t = 0.5$[ps].

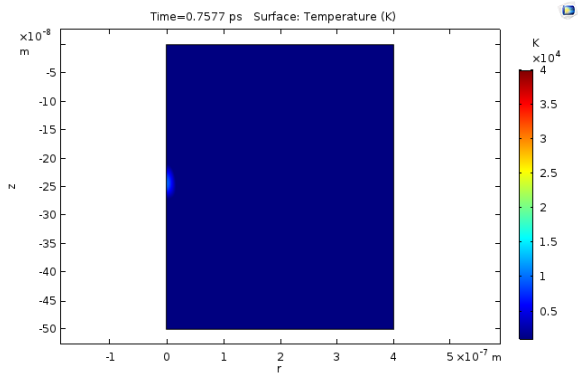

(c) $t = 0.75$[ps].

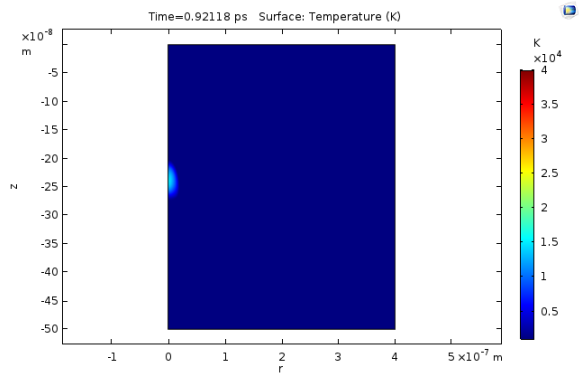

(d) $t = 0.9$[ps].

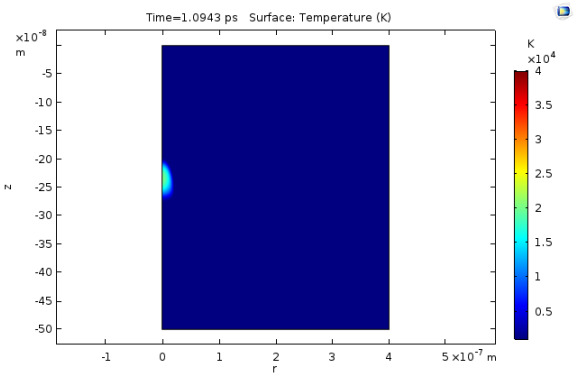

(e) $t = 1.1$[ps].

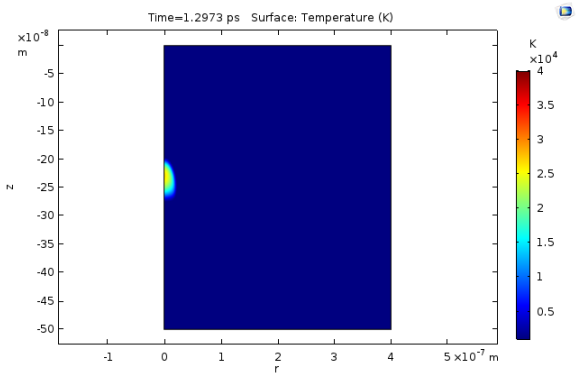

(f) $t = 1.3$[ps].

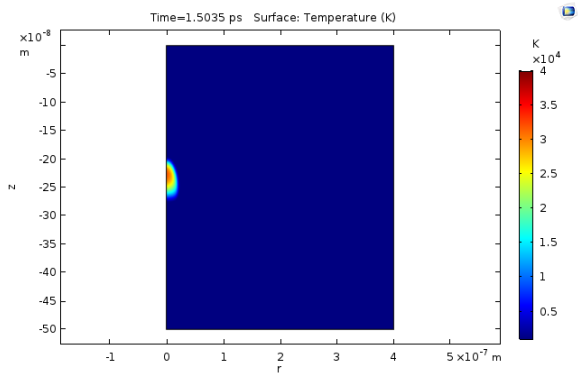

(g) $t = 1.5$[ps].

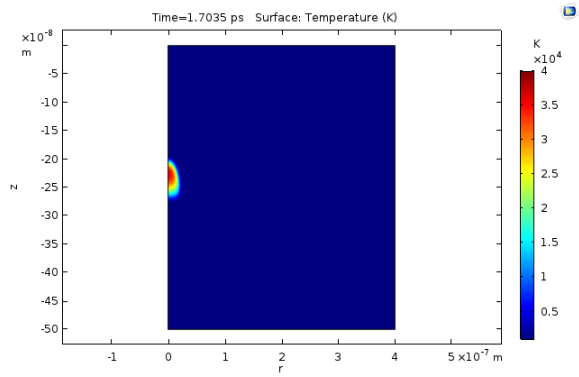

(h) $t = 1.7$[ps].

Figure 5.31: Lattice temperature (T_l) distribution in time, high energy pulse ($E_p = 0.05$[μJ]).

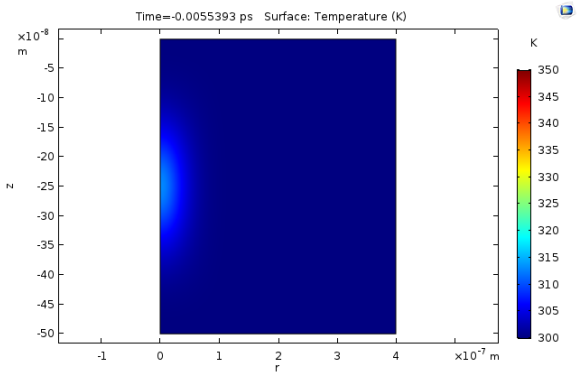

(a) $t = 0$[ps].

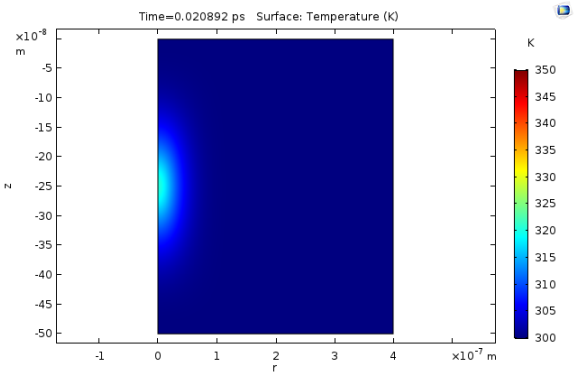

(b) $t = 0.02$[ps].

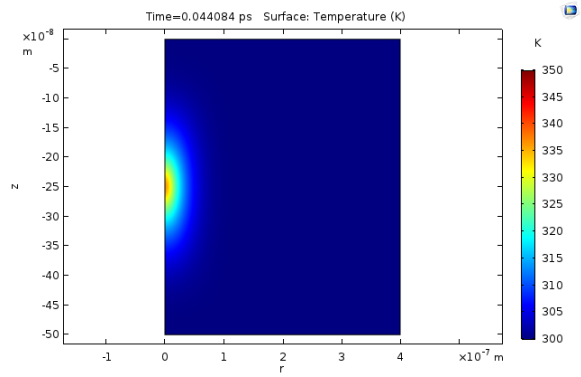

(c) $t = 0.04$[ps].

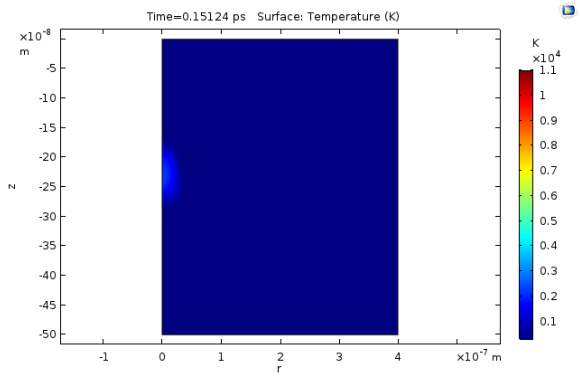

(d) $t = 0.15$[ps].

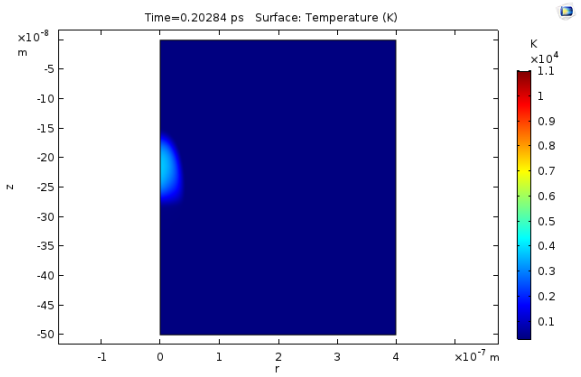

(e) $t = 0.2$[ps].

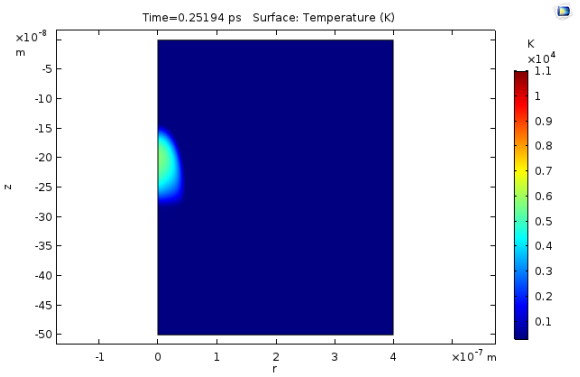

(f) $t = 0.25$[ps].

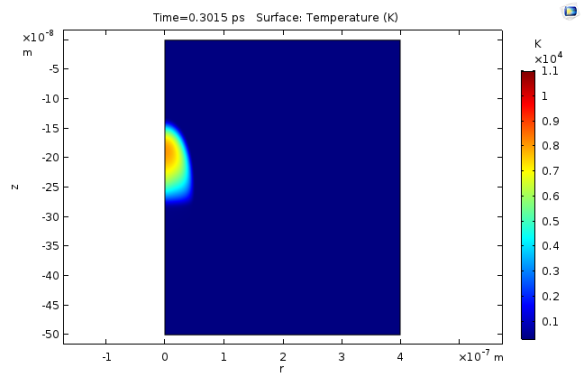

(g) $t = 0.3$[ps].

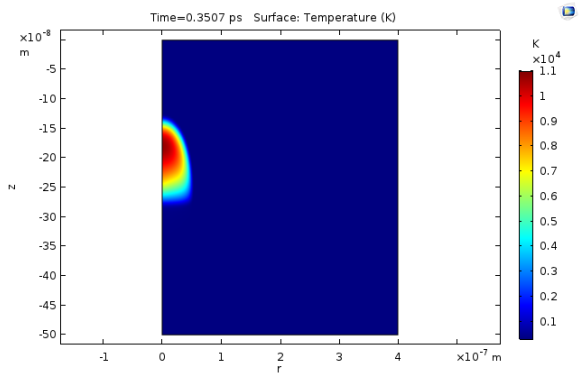

(h) $t = 0.35$[ps].

Figure 5.32: Lattice temperature (T_l) distribution in time, high energy pulse ($E_p = 0.06$[μJ]).

The high intensity causes tunneling ionization to occur, following the Keldysh ionization framework, see Figure 2.6. After which free electron absorption becomes dominant, triggering the shielding effect before the FWHM is reached ($t < -0.5$[ps]), see Figures 5.33, 5.34 and 5.35.

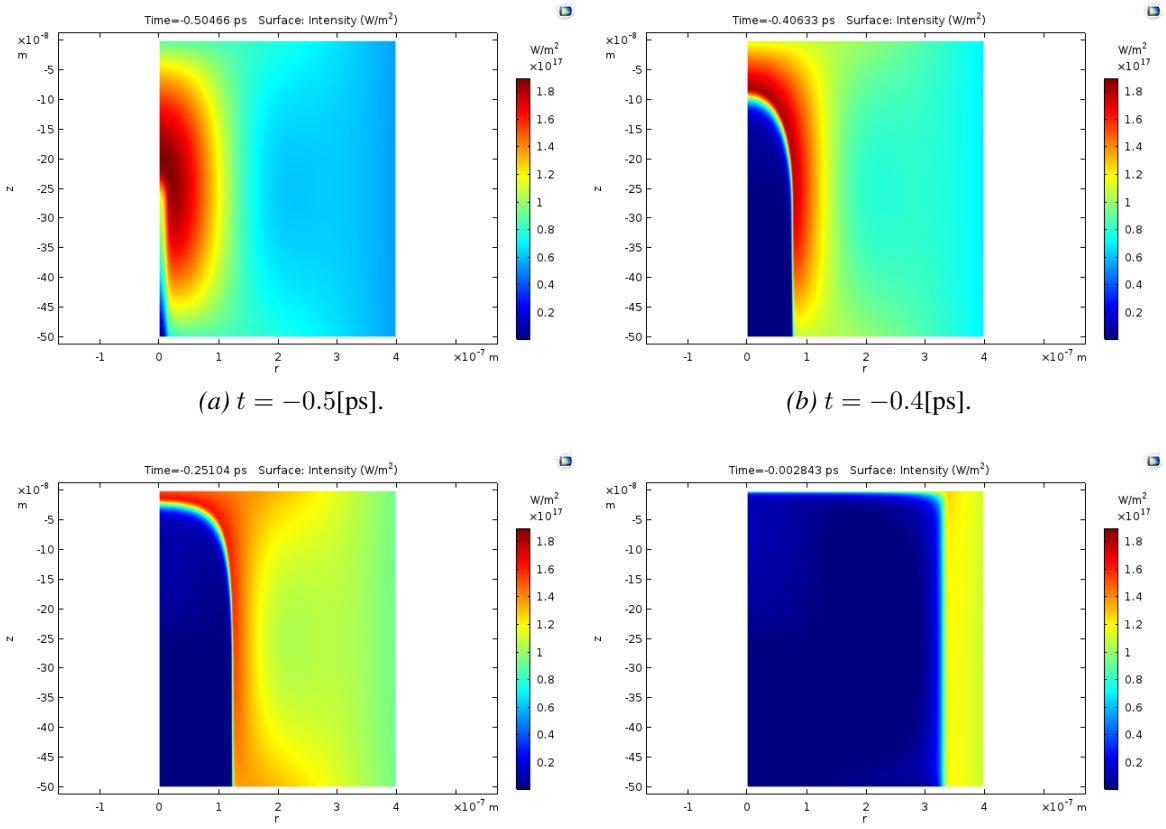

(a) $t = -0.5$[ps]. *(b)* $t = -0.4$[ps].

(c) $t = -0.25$[ps]. *(d)* $t = 0$[ps].

Figure 5.33: Intensity (I) distribution in time, higher energy pulse ($E_p = 0.2$[μJ]).

Due to the high intensity the plasma region continues to expand and develops towards the top boundary, see Figure 5.33c. After reaching the top surface, the shield expands towards the right boundary, see Figure 5.33d, until the entire domain is shielded.

Free electron density distribution

The free electron density generating the shield behaves identical to the high energy pulse, see Figures 5.16 and 5.19. The behaviour extending beyond the domain shows post-processing behaviour, as the incident pulse energy no longer influences the behaviour below the shield.

In the focal point, after the avalanche ionization dominates, see Figures 5.36a and 5.37, the electron density continues to increase. As a result of the remaining free electrons in the focal point, impact events continue to occur, increasing the (local) free electron density, see Figure 5.38.

Meanwhile, recombination continues to reduce the free electron density, until an equilibrium between the Drude ionization and recombination is reached, after which recombination is the dominant process, see Figure 5.38. Yet, the recombination effect reduces as more electrons recombine, until the initial free electron density, before excitation of electrons, is reached.

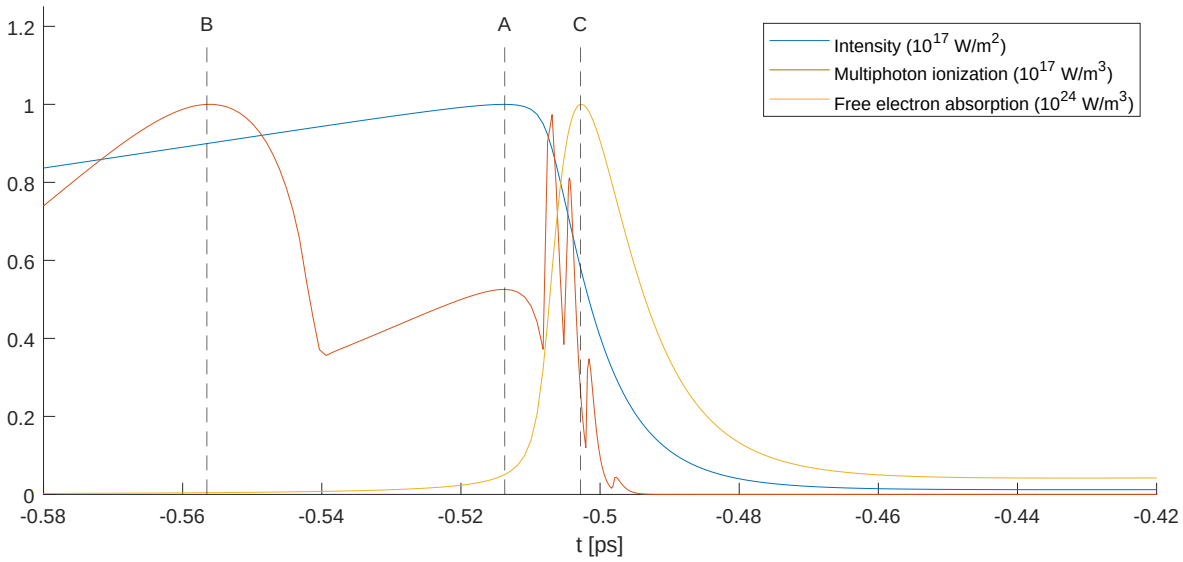

Figure 5.34: Normalized multiphoton ionization (L_{mpi}) and free electron absorption (L_{abs}) response to intensity (I) at $(0, z_f)$, reaching maximum at B and C respectively ($E_p = 0.2$[µJ]).

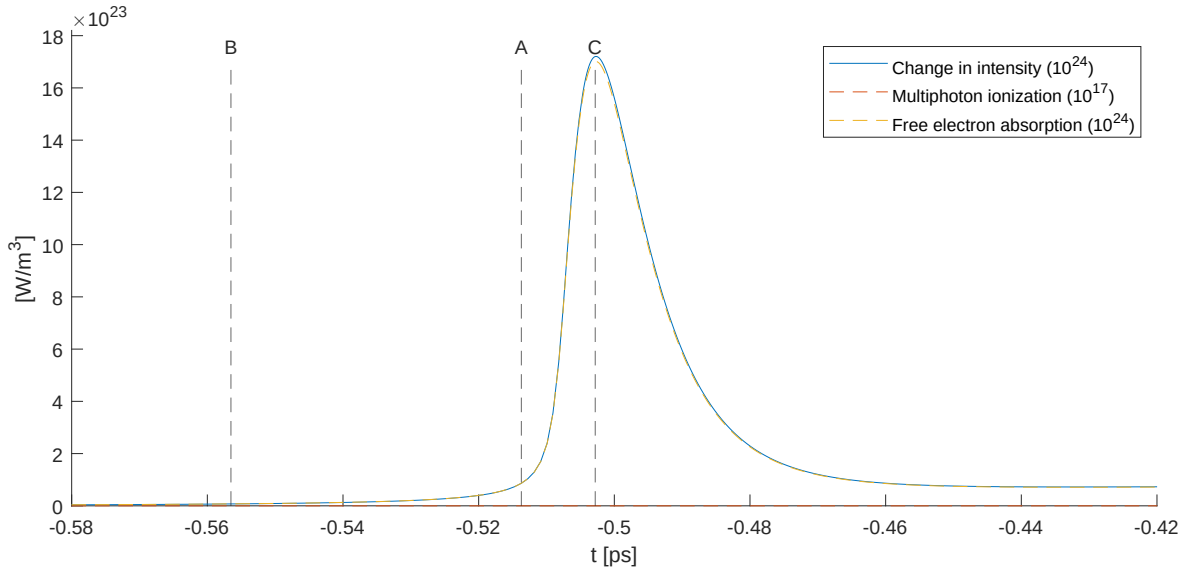

Figure 5.35: Effects of multiphoton ionization (L_{mpi}) and free electron absorption (L_{abs}) on the intensity (I)at $(0, z_f)$, reaching maximum at B and C respectively ($E_p = 0.2$[µJ]).

Free electron temperature distribution

The free electron temperature distribution behaves identical to the low and high energy pulse. When the exchange of energy between electrons and phonons via the two-temperature model is initiated, the local effect seen in Figure 5.26 is observed. The rapid diffusion and carrier-carrier interaction increases the free electron temperature evenly throughout the domain, as seen in Figure 5.12.

Only minimal differences are observed after plasma generation at $t > -0.5$[ps], see Figure 5.43, comparing maximum electron temperature in the focal point, at the top surface, along the optical axis and throughout the domain.

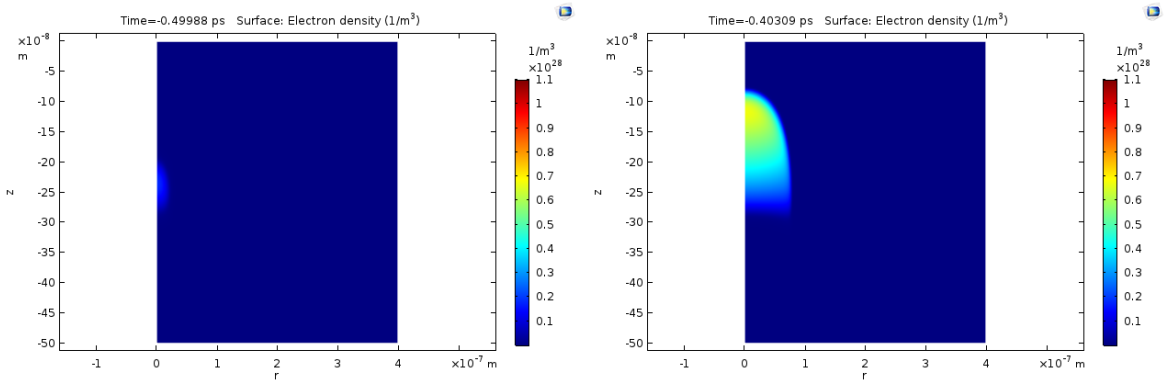

(a) $t = -0.5$[ps]. *(b)* $t = -0.4$[ps].

(c) $t = -0.25$[ps]. *(d)* $t = 0$[ps].

Figure 5.36: Free electron density (n_e) distribution in time, higher energy pulse ($E_p = 0.2$[µJ]).

Again, the initial increase in free electron temperature is due to multiphoton ionization, generating free electrons, increasing the kinetic energy according to the Keldysh framework, see Figure 2.6.

Due to the higher intensity, the effects occur in more rapid succession than for high energy pulses. Most notably the two-temperature exchange is minor, see Figure 5.42, yet after subsequent strong carrier-carrier interaction and free electron absorption effects, the two-temperature exchange determines the free electron temperature, see Figures 5.39 and 5.40.

As seen in the detailed graph, see Figure 5.41, the carrier-carrier interaction redistributes and the two-temperature exchange reduces the free electron temperature. Followed by an

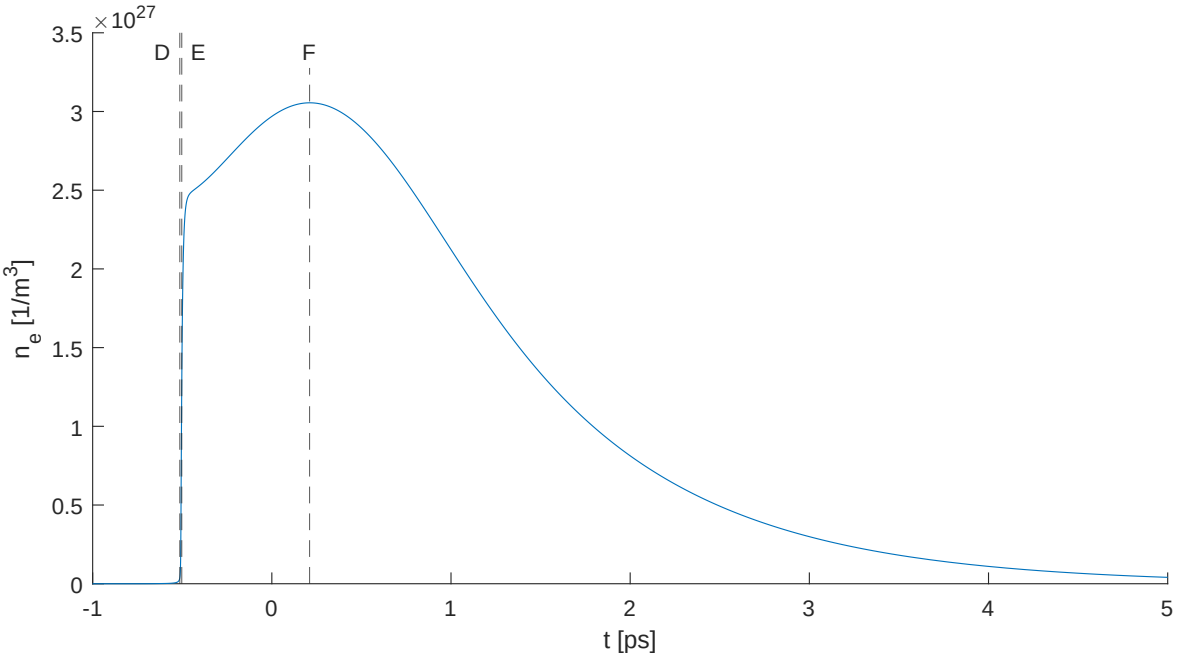

Figure 5.37: Free electron density (n_e) due to Keldysh ionization (P_{pi}), Drude ionization (P_{abs}) and recombination (L_{rec}) at $(0, z_f)$, reaching maximum at D, E and F respectively ($E_p = 0.2$[μJ]).

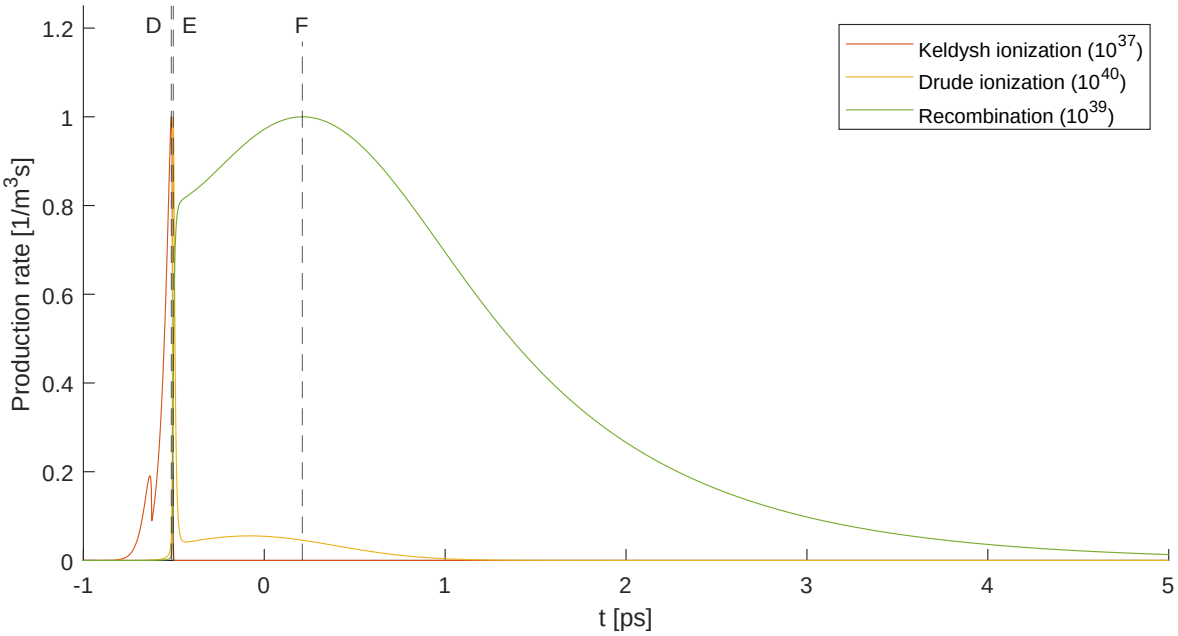

Figure 5.38: Normalized Keldysh ionization (P_{pi}), Drude ionization (P_{abs}) and recombination (L_{rec}) at $(0, z_f)$, reaching maximum at D, E and F respectively ($E_p = 0.2$[μJ]).

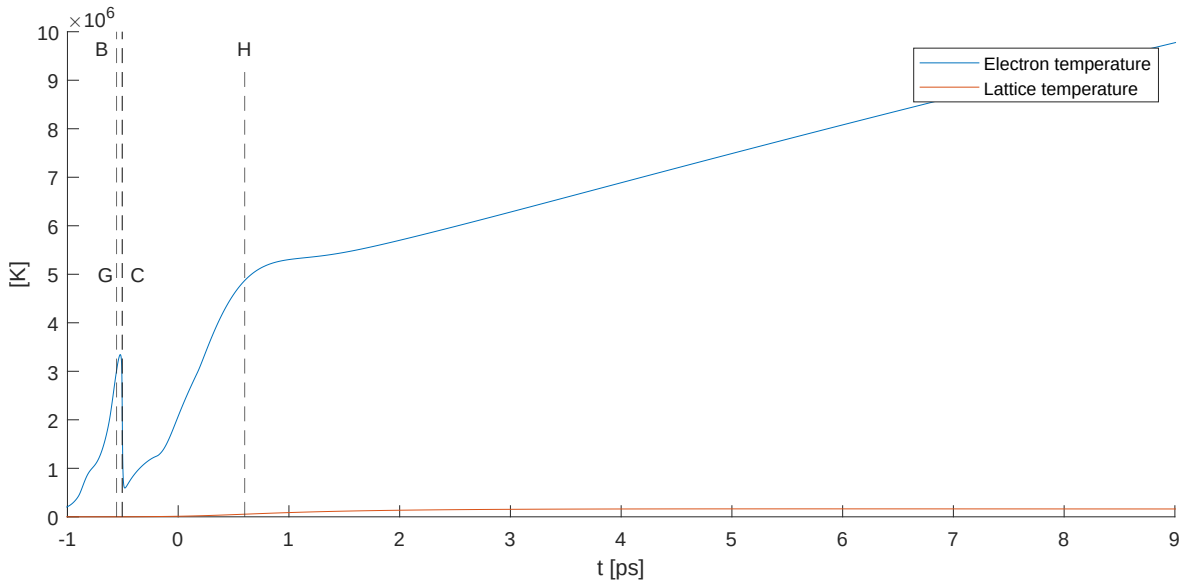

Figure 5.39: Free electron temperature (T_e) due to multiphoton ionization (S_{mpi}), free electron absorption (S_{abs}), carrier-carrier interaction (CC) and two-temperature exchange (L_{TTM}) response to all variables at $(0, z_f)$ reaching maximum at B, C, G, H respectively ($E_p = 0.2$[µJ]).

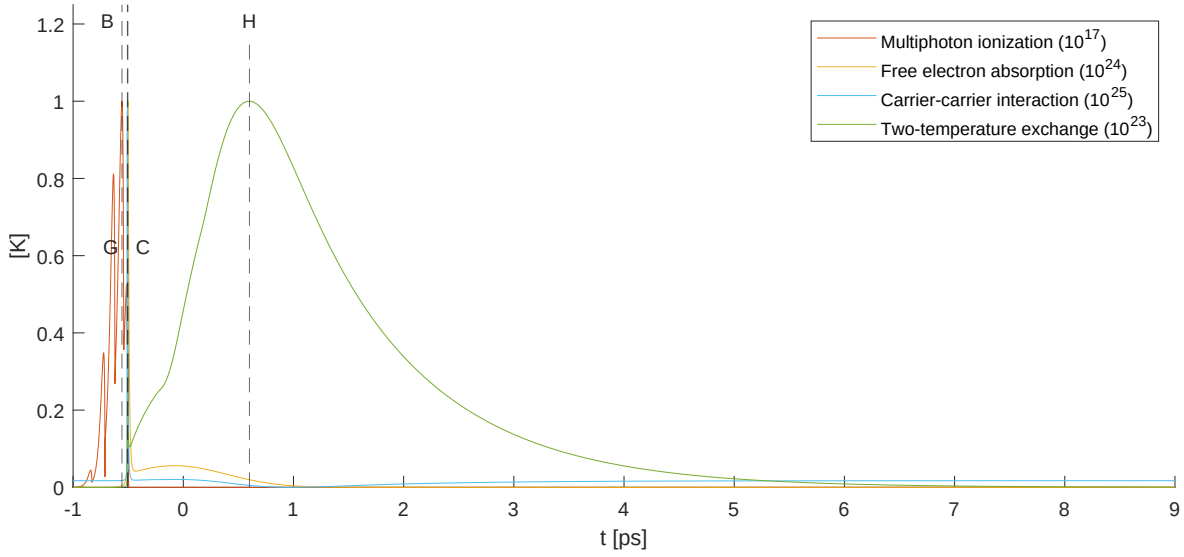

Figure 5.40: Normalized multiphoton ionization (S_{mpi}), free electron absorption (S_{abs}), carrier-carrier interaction (CC) and two-temperature exchange (L_{TTM}) response to all variables at $(0, z_f)$, reaching maximum at B, C, G, H respectively ($E_p = 0.2$[µJ]).

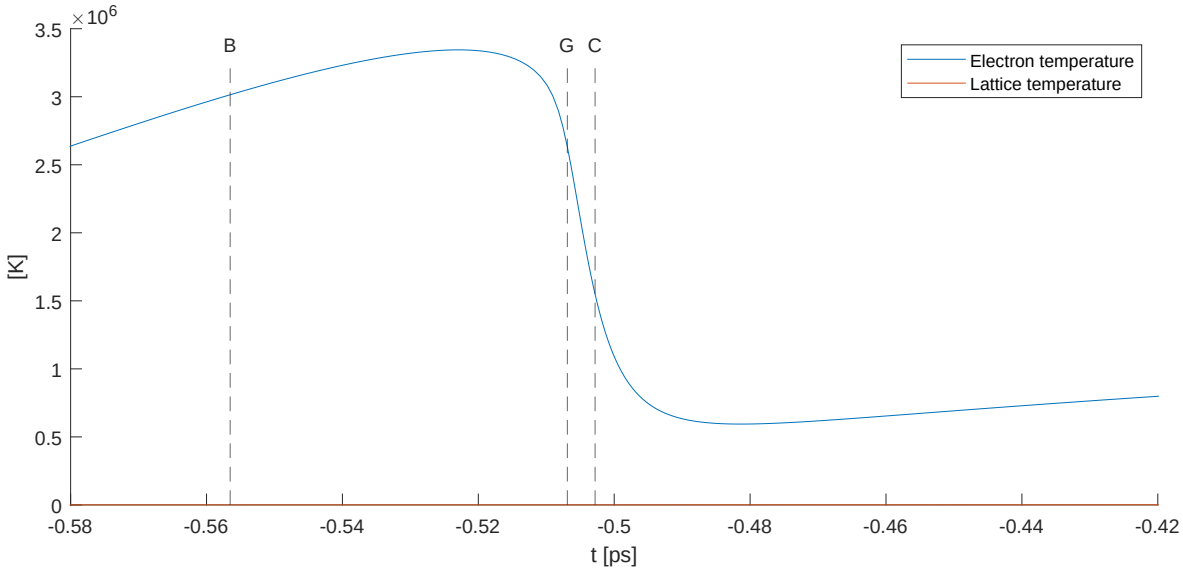

Figure 5.41: Free electron temperature (T_e) due to multiphoton ionization (S_{mpi}), free electron absorption (S_{abs}), carrier-carrier interaction (CC) and two-temperature exchange (L_{TTM}) response to all variables at $(0, z_f)$, reaching maximum at B, C, G, H respectively ($E_p = 0.02$[µJ], detailed).

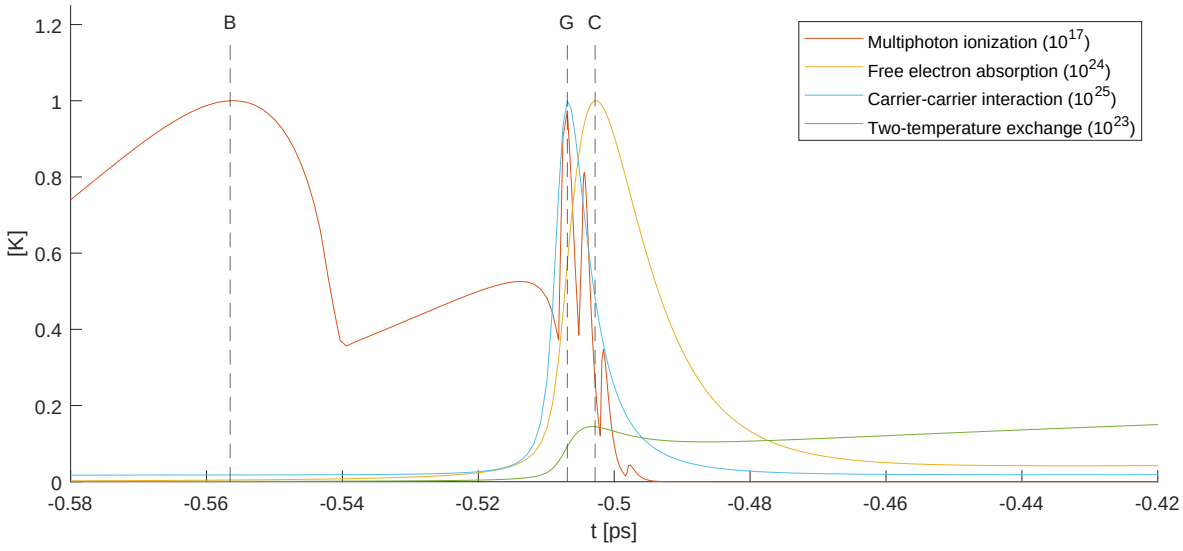

Figure 5.42: Normalized multiphoton ionization (S_{mpi}), free electron absorption (S_{abs}), carrier-carrier interaction (CC) and two-temperature exchange (L_{TTM}) response to all variables at $(0, z_f)$, reaching maximum at B, C, G, H respectively ($E_p = 0.2$[µJ], detailed).

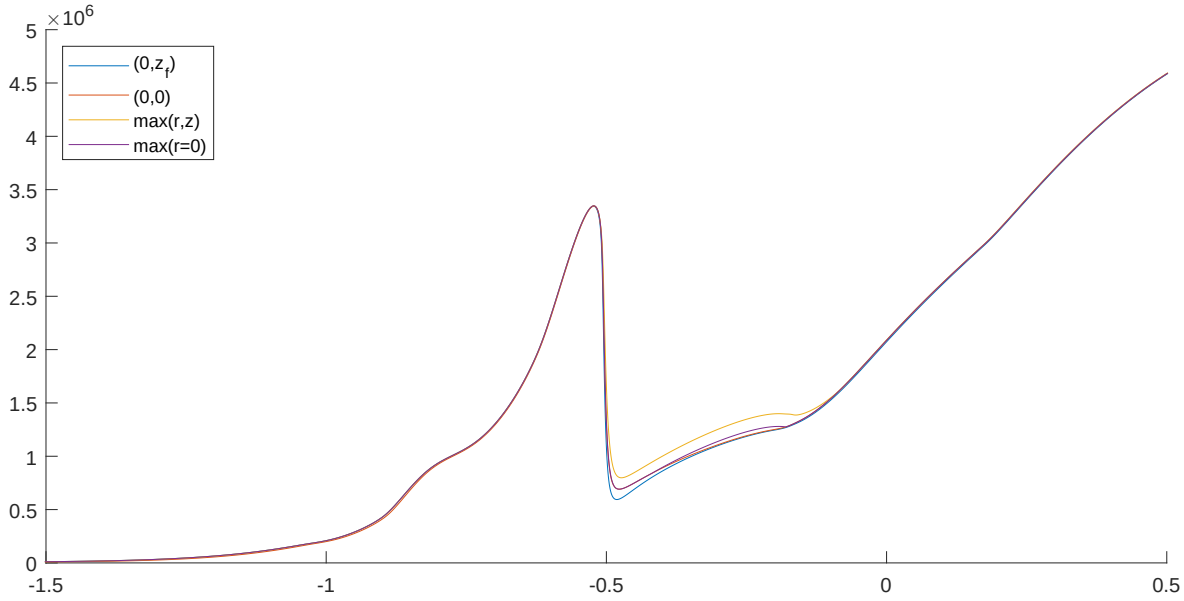

Figure 5.43: Free electron temperature (T_e) at $(0, z_f)$, $(0, 0)$, the domain maximum and the optical axis maximum respectively ($E_p = 0.2$[µJ]).

increase of free electron temperature, due to free electron absorption, as more free electrons are available to absorb pulse energy.

An extended simulation, until 300[ps], shows that the free electron temperature decreases towards 300[K] (T_0) around $t = 100$[ps], see Figure 5.44. This effect coincides with the complete recombination of all free electrons in the focal point. Thus, the increase in free electron temperature before complete recombination is due to the kinetic energy remaining in the free electrons, i.e. less free electrons containing the same quantity of energy, leading to an increase in temperature [61,62].

Lattice temperature distribution

The lattice temperature distribution behaves identical to the high energy pulse lattice temperature, see Figures 5.31 and 5.32. Nevertheless, the lattice temperature distribution continues until the top surface, see Figure 5.46d, following the free electron density behaviour, see Figure 5.36d.

The extended simulation until 300[ps] confirmed the temperature diffusing into the bulk material. Though difficult to display, the lattice temperature continues to decrease in the focal point and throughout the domain due to the implemented boundary conditions. In Figure 5.45, where the lattice temperature in the focal point, top surface and domain maximum is displayed, the lattice temperature continues to decrease.

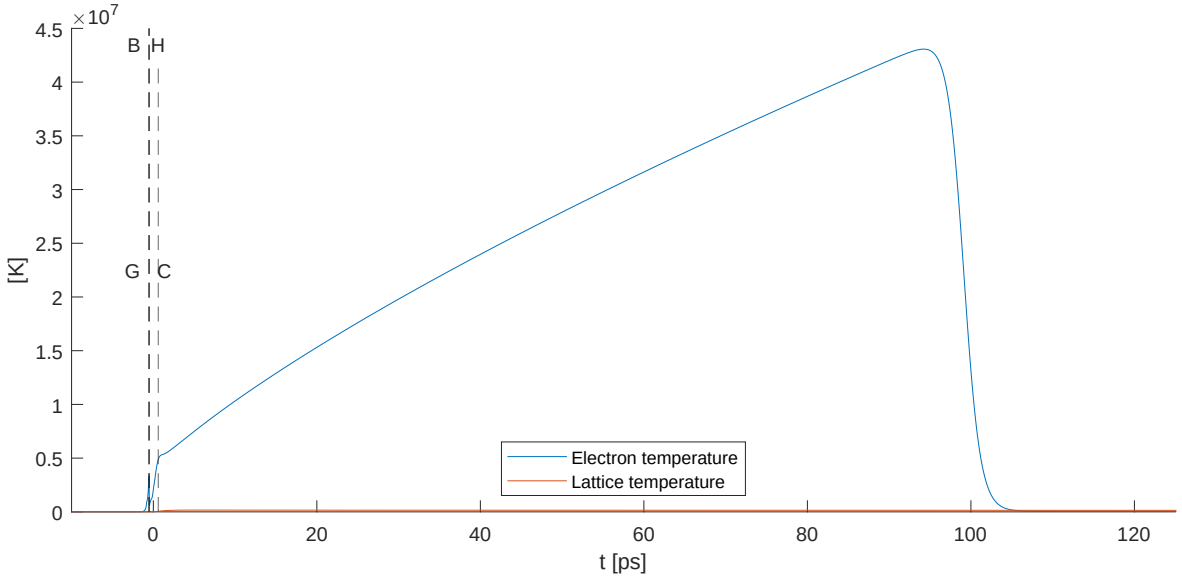

Figure 5.44: Free electron temperature (T_e) due to multiphoton ionization (S_{mpi}), free electron absorption (S_{abs}), carrier-carrier interaction (CC) and two-temperature exchange (L_{TTM}) response to all variables at $(0, z_f)$, ($E_p = 0.2$[µJ], extended).

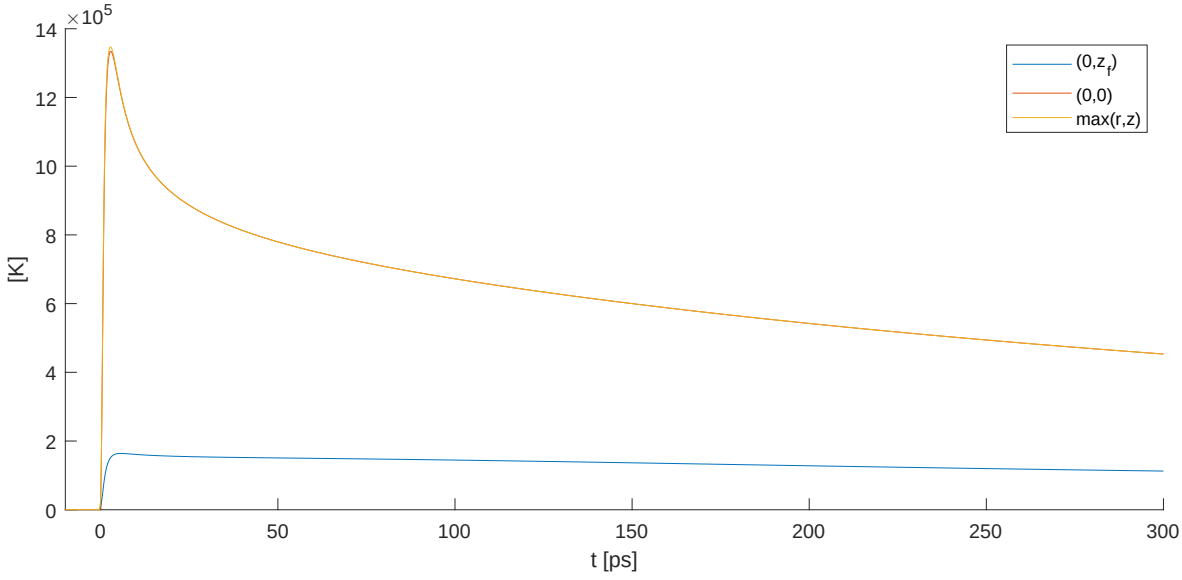

Figure 5.45: Lattice temperature (T_l) at $(0, z_f)$, $(0, 0)$ and domain maximum respectively ($E_p = 0.2$[µJ]).

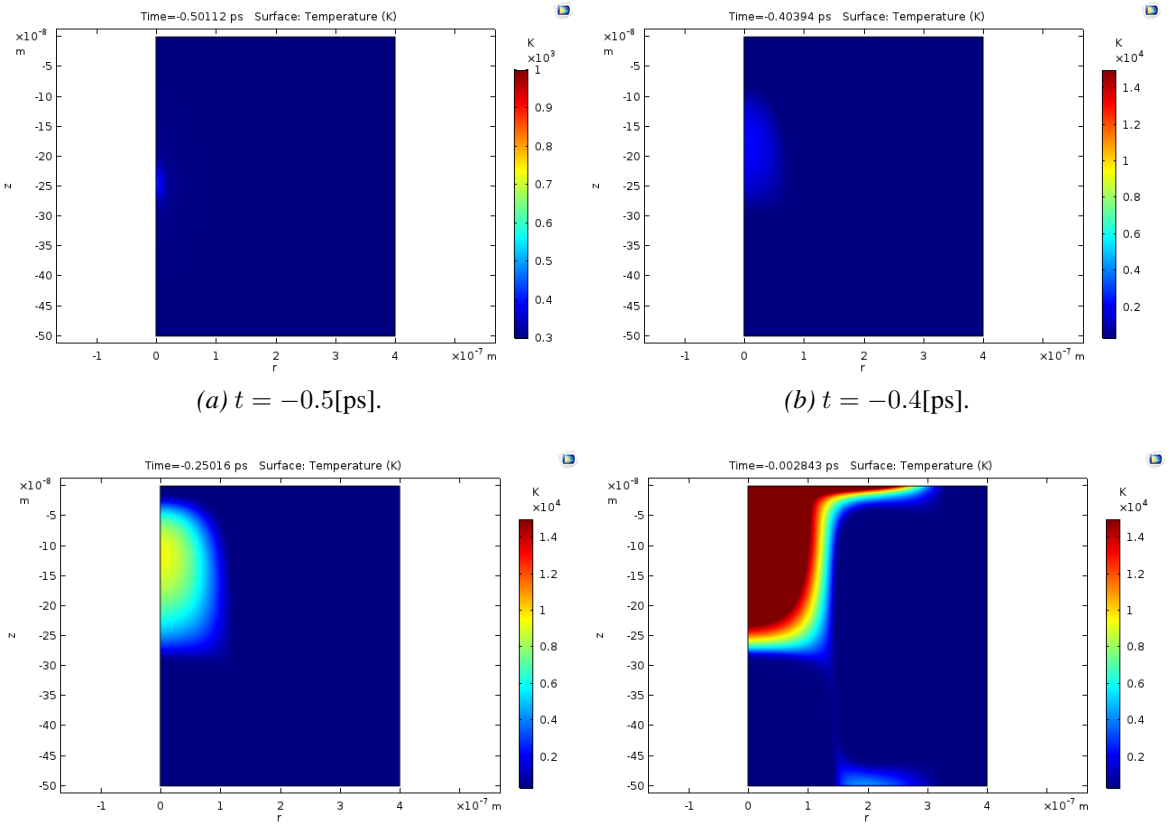

(a) $t = -0.5$[ps]. *(b)* $t = -0.4$[ps].

(c) $t = -0.25$[ps]. *(d)* $t = 0$[ps].

Figure 5.46: Lattice temperature (T_l) distribution in time, higher energy pulse ($E_p = 0.2$[µJ]).

5.3 Summary

The performed scenarios are separated into three categories, low pulse energy, high pulse energy and higher pulse energy. For each of the categories different aspects of the improved model are presented, displaying the interaction of the phenomena, see Figures 5.47 and 5.48, similar to Sundaram et al. [16]. The interaction phenomena for low pulse energy remain in the focal region, whereas for high and higher pulse energy the effects occur in rapid succession, continuing outside the focal region due to plasma generation.

For the low pulse energy, the improved model demonstrates laser heating of a relatively large area in the domain. The effects of the Keldysh framework on the local free electron density and the subsequent effect on the lattice temperature distribution is shown, yet leads to negligible material modification.

For the high pulse energy, the improved model displays the effects of plasma generation in and above the focal region, as intensity is sufficient to trigger strong free electron absorption via the Drude model. Strong plasma generation leads to electron shield formation, shielding the material below from incident laser light, expanding the plasma in axial direction. The plasma generation leads to high lattice temperature and determines the lattice temperature distribution, trailing behind the free electron density distribution. Unfortunately the simulations did not converge, limiting the ability to gain further insight into understanding the interaction of phenomena after completion of the laser pulse.

The higher pulse energy did converge, however as the laser pulse extends beyond the domain, the interaction of phenomena are in the plasma region, describing post-processing behaviour below the electron shield. The effect of free electron recombination on the electron and lattice temperature shows that the material returns to the initial electron and lattice temperatures.

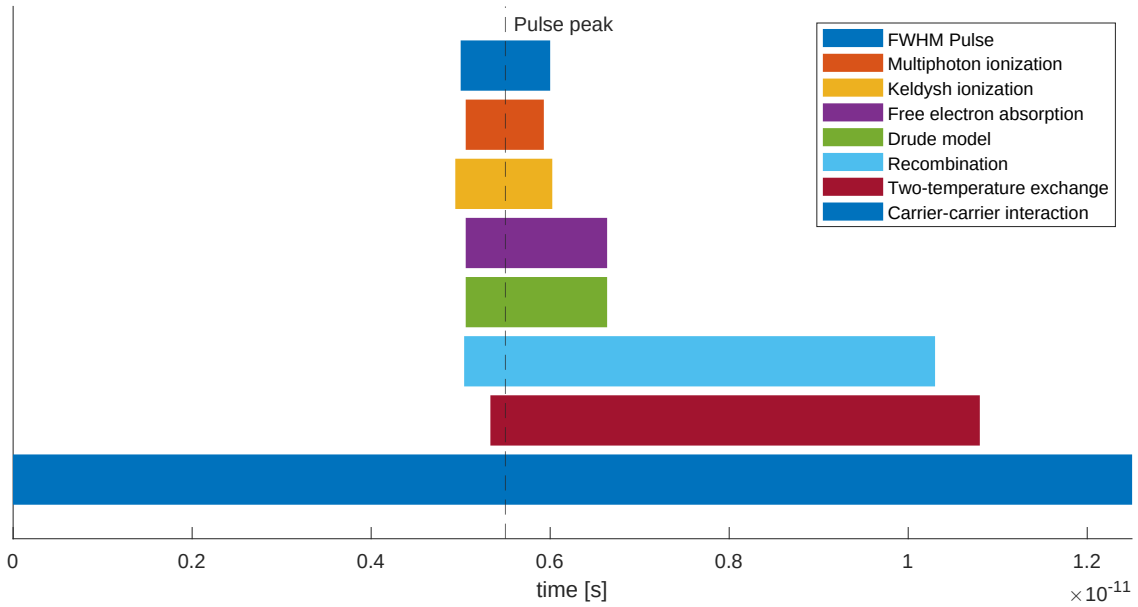

Figure 5.47: Displaying timescales of normalized interaction phenomena (98.75% of each effect) at $(0, z_f)$, $(E_p = 0.025[\mu J])$.

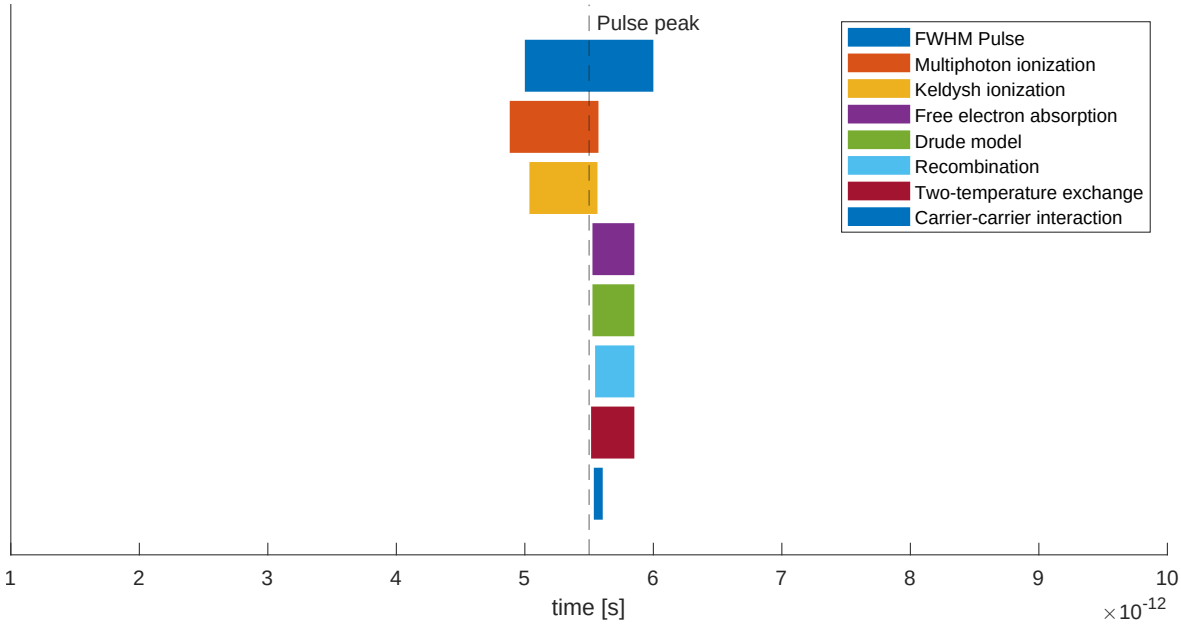

Figure 5.48: Displaying timescales of normalized interaction phenomena (98.75% of each effect) at $(0, z_f)$, $(E_p = 0.06[\mu J])$.

Chapter 6

Thermal stress

6.1 Introduction

The thermal stress studies are performed separately from the intensity, free electron density, free electron temperature and lattice temperature simulation in Chapter 5. The thermal expansion is determined via an extension of the improved model, for each of the scenarios described, using the lattice temperature output.

As indicated in Section 3.4 the temperature effect is modeled to observe if points of peak stress coincide with point of cracks in the processed material, see Figure 1.5. Important to note is the exclusion of other effects, i.e. amorphization and void formation, transferring all energy in the lattice temperature, strengthening the thermal effects.

The thermal stress is determined by the thermal expansion, but the thermal expansion and stress do not affect the system of equations, see Figure 4.1. The separation of the improved variable (I, n_e, T_e, T_l) simulations and of the thermal stress reduces calculation time of the improved model.

Using an additional time-dependent study, the lattice temperature of each time step of the improved model is used as input for calculating the thermal expansion. The time steps have been reduced to provide output each 0.1[ps] or 0.01[ps], depending on the lattice temperature behaviour.

In Chapter 5 the lattice temperature, see Figures 5.13, 5.31, 5.32 and 5.46, before electron shielding show similar temperature distributions, concentrated around the focal point. Whereas, for high and higher pulse energy the electron shielding shapes the lattice temperature, affecting the thermal expansion significantly.

First the low pulse energy effects on thermal expansion and stress are presented and discussed, followed by high and higher pulse energy combined, as the lattice temperature profiles are similar. Out of interest for the anisotropic response, for additional studies the elasticity tensor ($\boldsymbol{C}$), see Equation (3.19), has been modified to determine the anisotropic material response. Criteria for crystals, such as sapphire, are complex therefore to show behaviour the stress displayed is the the equivalent tensile stress or von Mises stress [63,64].

6.2 Low pulse energy - radial expansion

The calculated thermal stress levels for low pulse energy are negligible, remaining below 2[MPa], however it displays the initial effects of thermal expansion leading to thermal stress due to laser induced heating, see Figures 6.1 and 6.2.

The thermal expansion initiates in and around the focal point, see Figures 6.1a and 6.1b,

up to the peak of the pulse ($t = 0$[ps]), due to the local lattice temperature, see Figure 5.13.

However, the electron density ring, shaping the lattice temperature distribution, see Figures 5.7 and 5.13, counteracts the thermal expansion in the focal point, see Figures 6.1c and 6.1d.

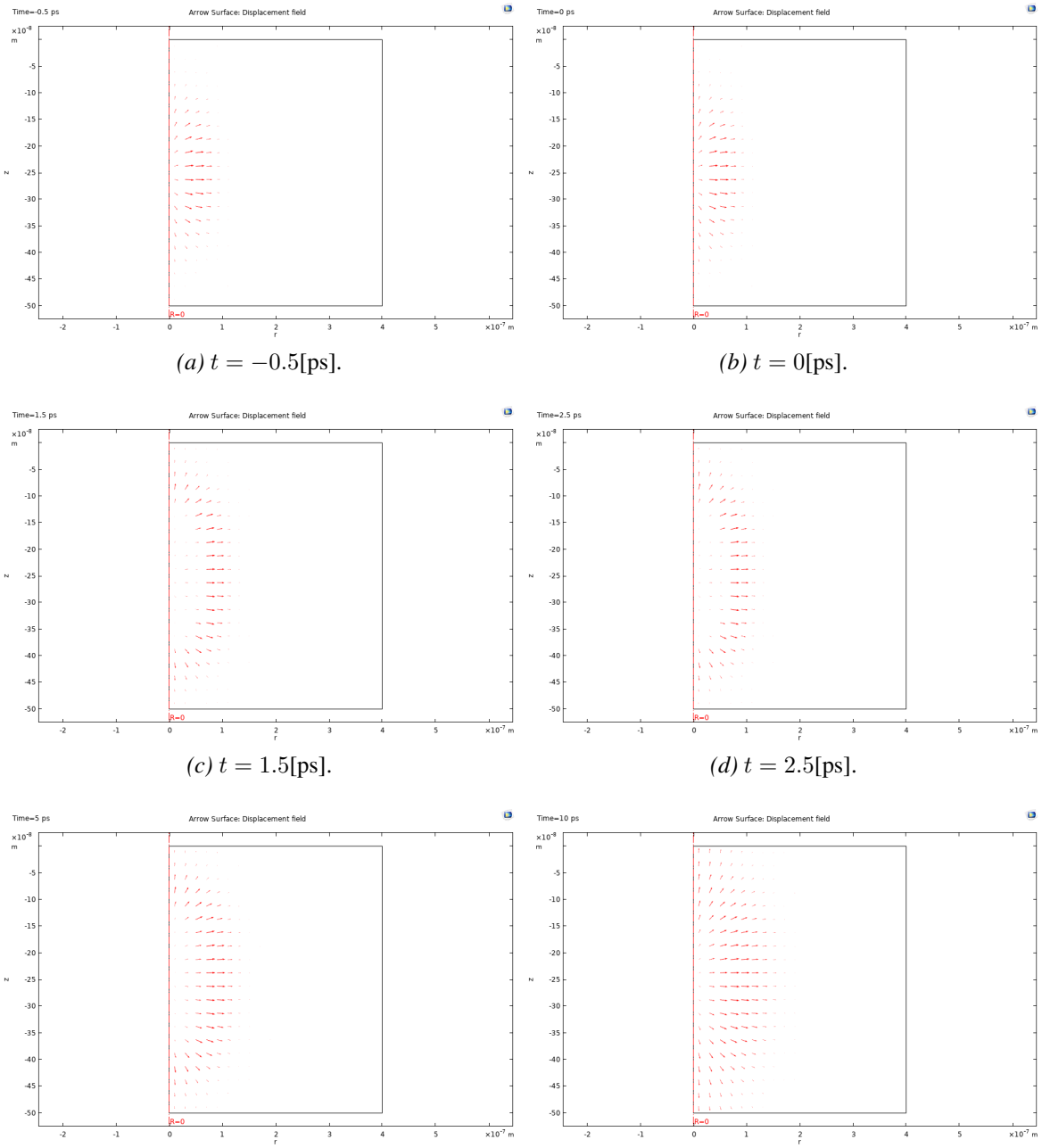

(a) $t = -0.5$[ps]. *(b)* $t = 0$[ps].

(c) $t = 1.5$[ps]. *(d)* $t = 2.5$[ps].

(e) $t = 5$[ps]. *(f)* $t = 10$[ps].

Figure 6.1: Displacement ($\boldsymbol{u}$) in time, low energy pulse ($E_p = 0.025$[µJ]).

Due to lattice temperature diffusion, the ring dissipates, the temperature distribution in and around the focal point homogenizes, see Figure 5.13h, leading to a continuous displacement field, see Figure 6.2f.

The thermal expansion brings about minimal thermal stress, yet presents the resulting stress of laser heating. Initially, the stress in and around the focal point is highest, see Figures

6.2a and 6.2b, due to expansion, up to the peak of the pulse.

The counteracting effect of thermal expansion in the ring reduces the displacement and subsequently the stress in the focal point, see Figures 6.2c and 6.2d. However, displacement in the radial direction as a result of the ring continues to cause stress, see Figure 6.2e, until the effect dissipates, see Figure 6.2f.

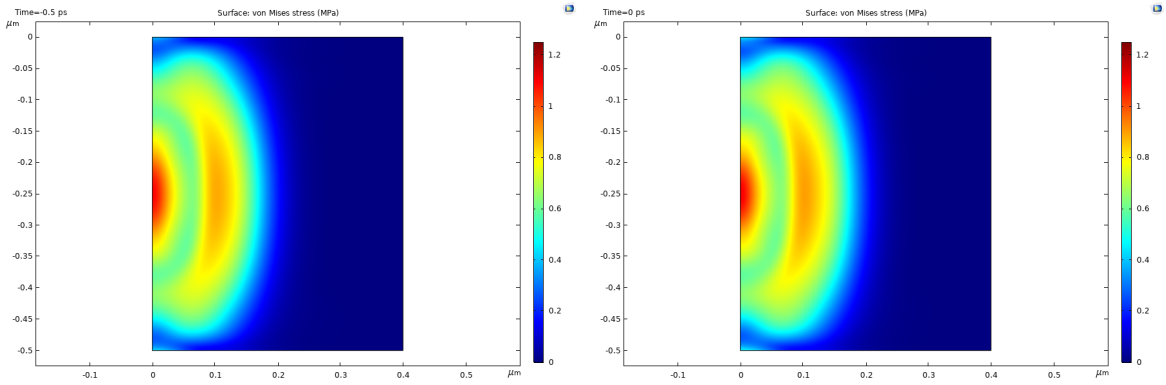

(a) $t = -0.5$[ps]. *(b)* $t = 0$[ps].

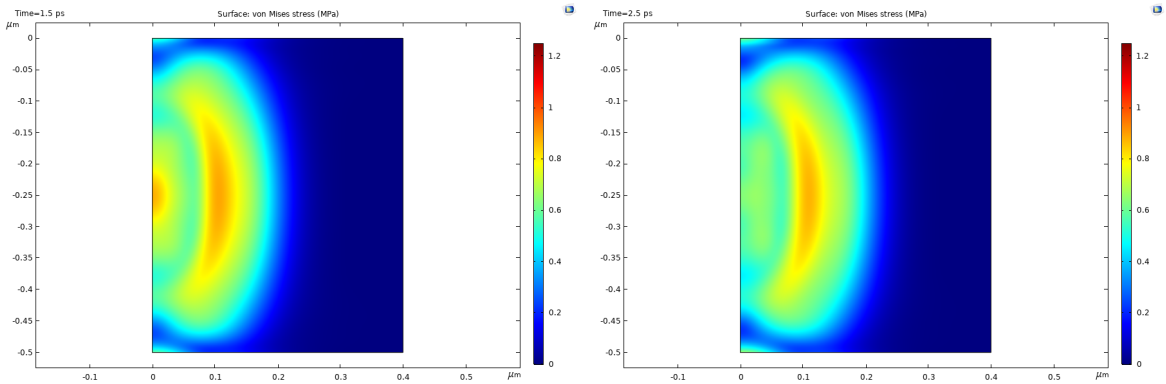

(c) $t = 1.5$[ps]. *(d)* $t = 2.5$[ps].

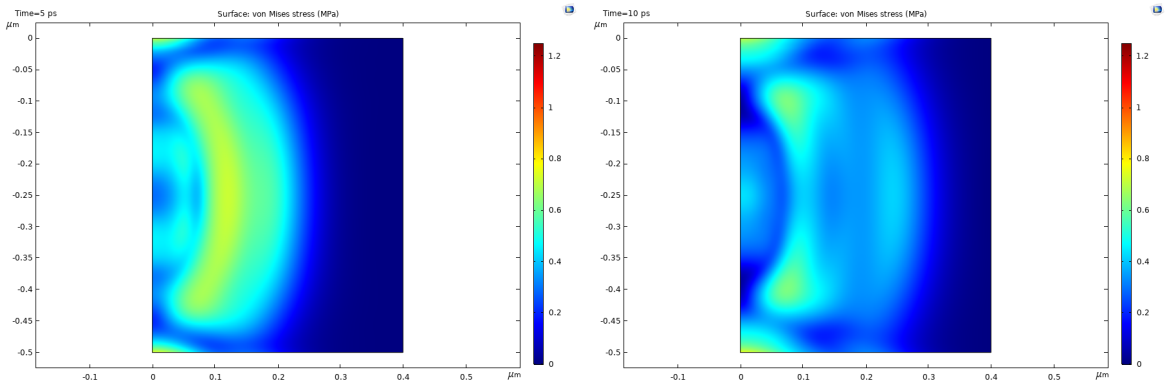

(e) $t = 5$[ps]. *(f)* $t = 10$[ps].

Figure 6.2: Von Mises stress (σ_v) in time, low energy pulse ($E_p = 0.025$[µJ]).

An artefact of the model is the stress concentrations near the optical axis, at the top and bottom boundary, see Figures 6.2e and 6.2f. Due to the limited modeled domain and expansion in axial direction, the stress concentrates in the corners of the domain.

6.3 High pulse energy - isotropic

The high and higher pulse energy effects on thermal expansion and subsequent thermal stress are presented using both high pulse energy simulations, 0.05[μJ] and 0.06[μJ], from Chapter 5. The effects of higher pulse energy are similar, however the rapid expansion and displacement of the plasma region, generating an electron shield before the FWHM, $-0.5 < t < 0.5$[ps], obscures the effects of thermal expansion on resultant stress, as the lattice temperature distribution exceeds the domain.

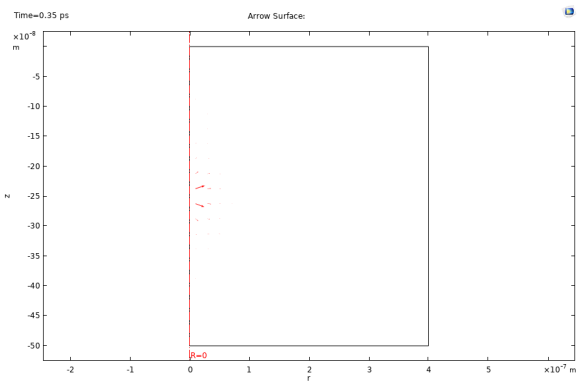

(a) $t = 0.35$[ps].

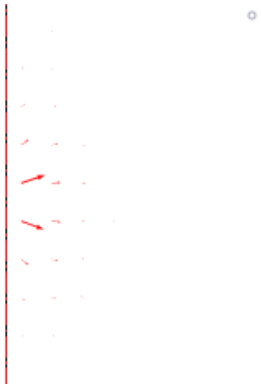

(b) $t = 0.35$[ps], detailed.

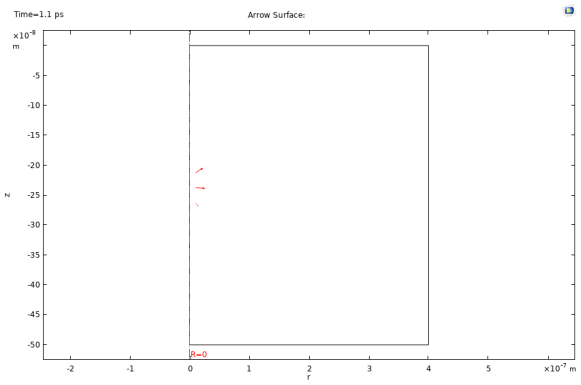

(c) $t = 1.1$[ps].

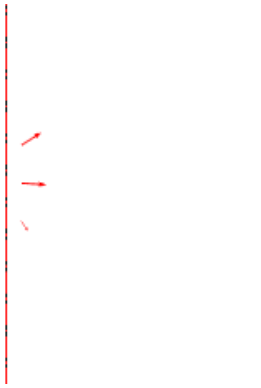

(d) $t = 1.1$[ps], detailed.

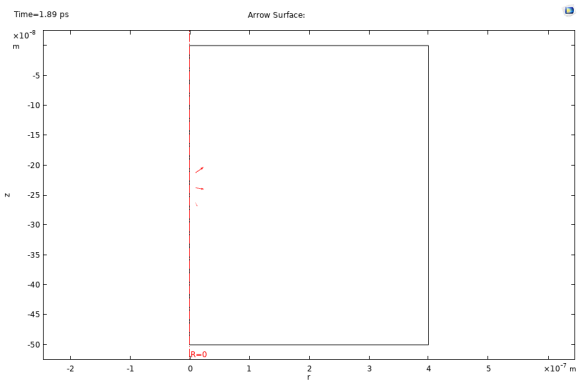

(e) $t = 1.9$[ps].

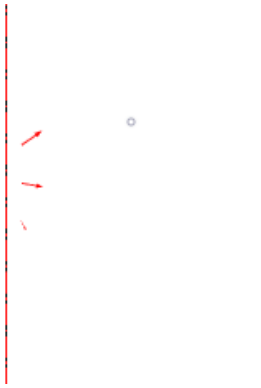

(f) $t = 1.9$[ps], detailed.

Figure 6.3: Displacement ($\boldsymbol{u}$) in time, high energy pulse ($E_p = 0.05$[μJ]).

The initial thermal expansion for both 0.05[µJ] and 0.06[µJ], see Figures 6.3a and 6.4a, is similar to the low pulse energy, see Figures 6.1a and 6.1b, concentrated at the focal point and surrounding area. The displacement occurs in a small region, as the lattice temperature increases significantly in and around the focal spot, see Figures 5.31 and 5.32.

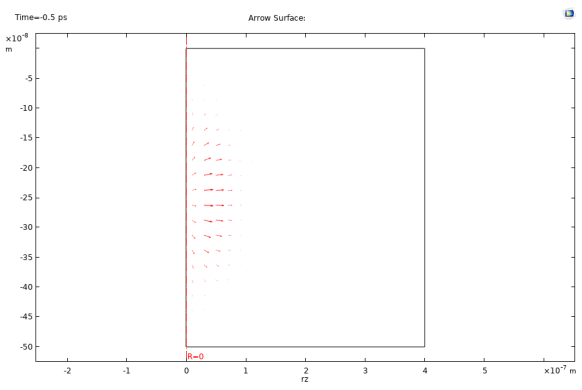

(a) $t = -0.5$[ps].

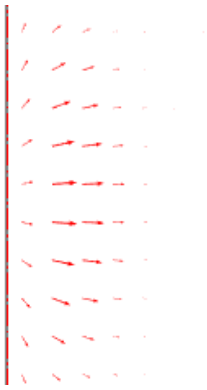

(b) $t = -0.5$[ps], detailed.

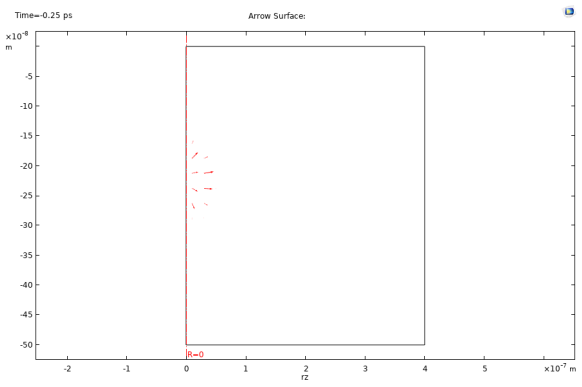

(c) $t = -0.25$[ps].

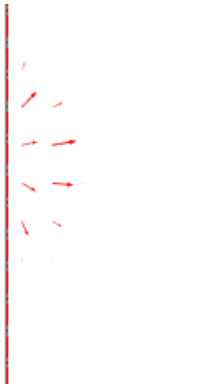

(d) $t = -0.25$[ps], detailed.

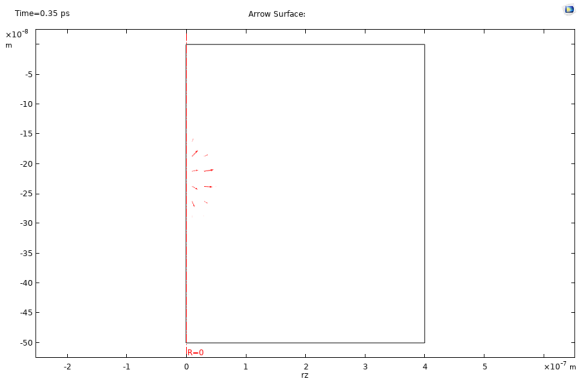

(e) $t = 0.35$[ps].

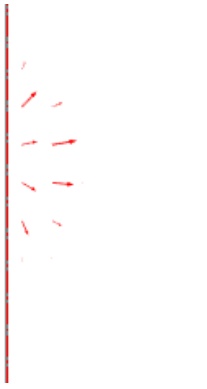

(f) $t = 0.35$[ps], detailed.

Figure 6.4: Displacement ($\boldsymbol{u}$) in time, high energy pulse ($E_p = 0.06$[µJ]).

The displacement field is modified due to the initiation of plasma generation, see Figures 6.3c, 6.3d, 6.4c and 6.4d. The outer layer of the plasma absorbs the incident pulse energy, i.e. the electron shield, increasing the free electron density, see Figures 5.16 and 5.19, expanding the plasma region in axial direction, towards the incident laser pulse. However, the difference in rate of expansion results in differences in stress.

The stress is concentrated in and around the focal point, see Figure 6.5, where the maximum of the stress bar is $1.1 \cdot 10^3$[MPa]. Significantly higher than for low pulse energy and in a smaller region due to high local lattice temperature, see Figure 5.31b.

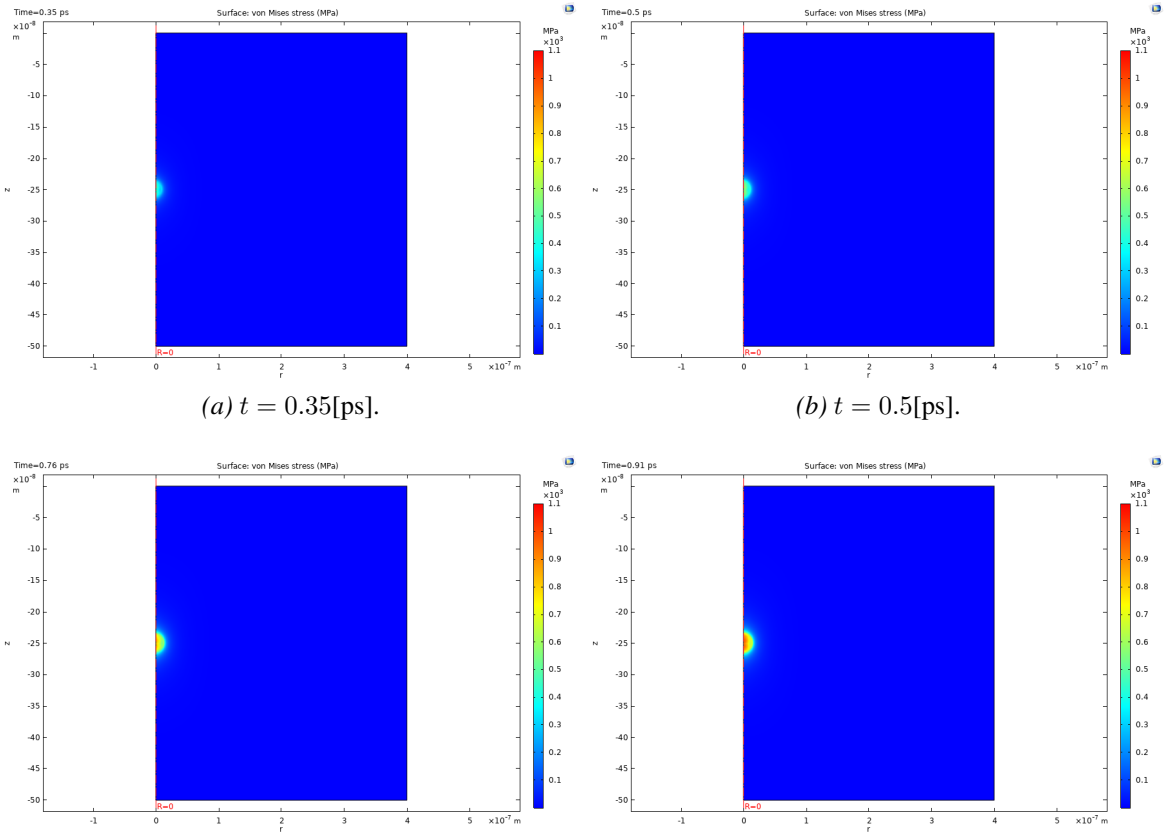

(a) $t = 0.35$[ps]. *(b)* $t = 0.5$[ps].

(c) $t = 0.75$[ps]. *(d)* $t = 0.9$[ps].

Figure 6.5: Von Mises stress (σ_v) in time, high energy pulse ($E_p = 0.05$[µJ]).

Due to plasma generation and electron shield formation, see Figures 5.31d and 5.31e, the stress outside the focal region becomes significant, see Figure 6.6a, where the maximum of the stress bar is $1.1 \cdot 10^3$[MPa]. The lattice temperature distribution trails the plasma region as it expands further in axial direction, see Figures 5.23 and 5.31.

The electron shield, absorbs the incident pulse energy, generating free electrons, maintaining a high free electron density, see Figure 5.16, determining the electron-phonon coupling coefficient (G_{TTM}), increasing the local lattice temperature. Due to the subsequent displacement, the stress at the electron shield is highest, see Figure 6.6b.

The shape of plasma region is maintained, due to incident laser energy decreasing ($t > 0$[ps]). The stress increases in the electron shield, as the high free electron density is maintained longest, see Figures 6.6c and 6.6d, where the maximum of the stress bar is $2.5 \cdot 10^5$[MPa].

Furthermore, the high free electron density in the plasma below the shield continues to interact with phonons. The lattice temperature below the electron shield increases, see Figure 5.31, leading to an increase in stress below the electron shield, see Figures 6.6e and 6.6e, here the maximum of the stress bar is $2.5 \cdot 10^5$[MPa].

For the 0.06[µJ] pulse energy, as mentioned, the effects are similar, see Figure 6.7. How-

ever, due to the higher incident pulse energy the effects occur during the FWHM of the pulse, $-0.5 < t < 0.5$[ps], thus the plasma region continues to expand.

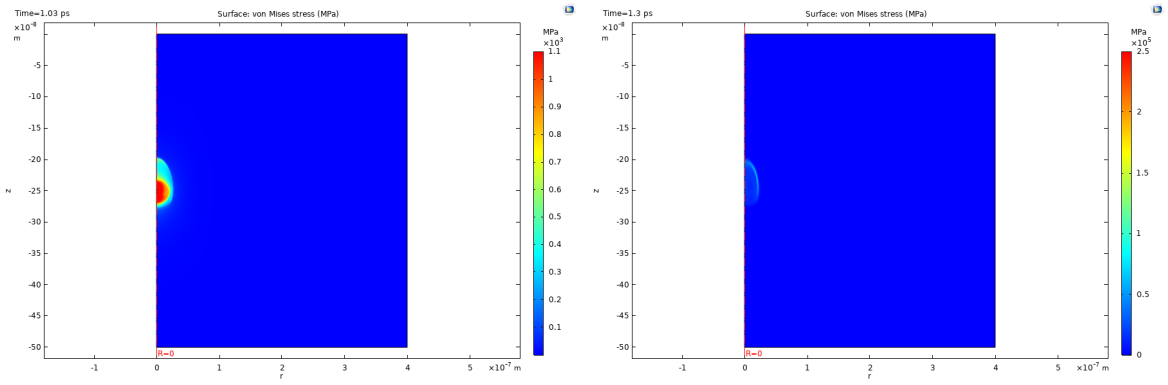

(a) $t = 1.03$[ps]. *(b)* $t = 1.3$[ps].

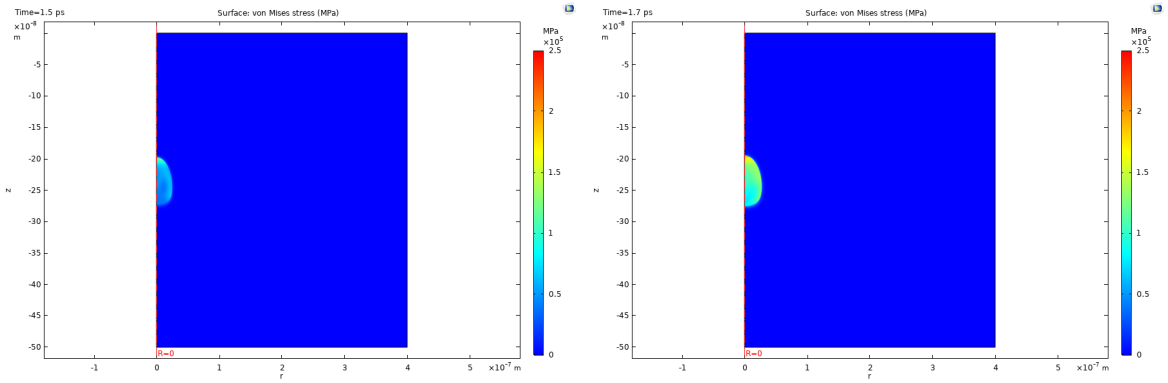

(c) $t = 1.5$[ps]. *(d)* $t = 1.7$[ps].

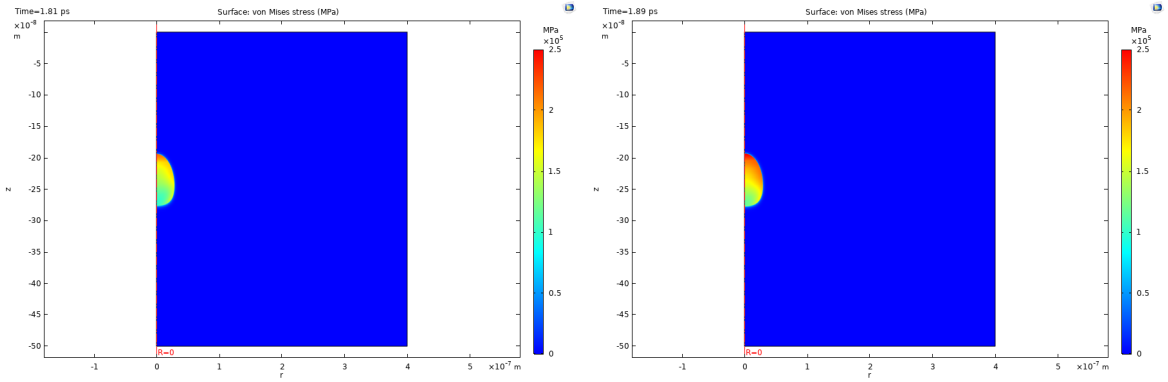

(e) $t = 1.8$[ps]. *(f)* $t = 1.9$[ps].

Figure 6.6: Von Mises stress (σ_v) in time, high energy pulse ($E_p = 0.05$[µJ]).

Due to the rapid expansion of the plasma region the free electron density in the focal region and at the electron shield is highest, leading to a discontinues stress, unlike 0.05[µJ], see Figures 6.6, 6.7e and 6.7f.

The convergence issues occur before completion of the FWHM of the pulse, therefore the maximum of the stress bar is only $1.7 \cdot 10^3$[MPa]. The stress is expected to increase, as for 0.05[µJ] the highest stress is observed at the last time instant, see Figure 6.6f.

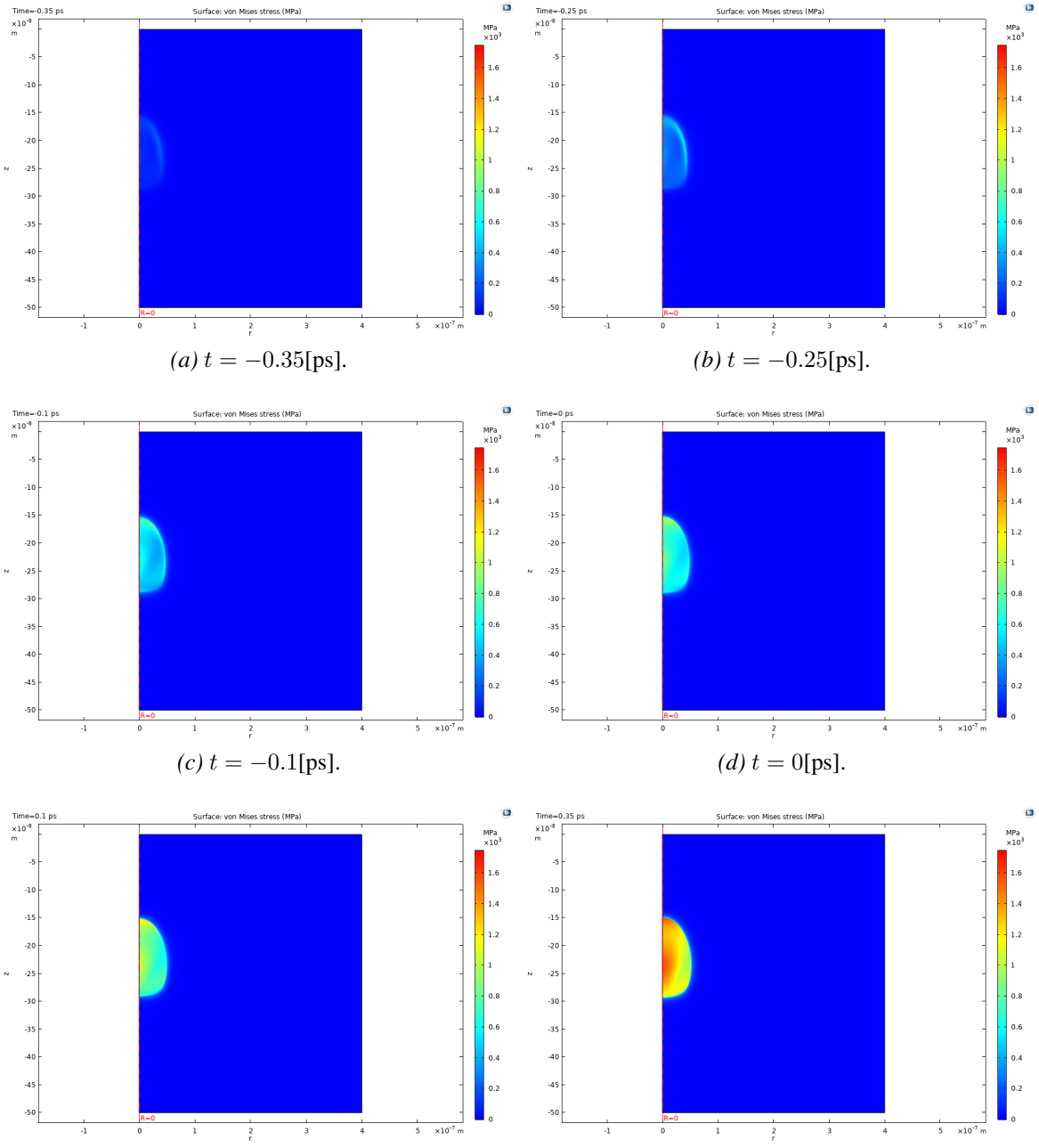

(a) $t = -0.35$[ps]. *(b)* $t = -0.25$[ps].

(c) $t = -0.1$[ps]. *(d)* $t = 0$[ps].

(e) $t = 0.1$[ps]. *(f)* $t = 0.35$[ps].

Figure 6.7: Von Mises stress (σ_v) in time, high energy pulse ($E_p = 0.06$[µJ]).

6.4 High pulse energy - anisotropic

The isotropic stress response to the thermal expansion displays high stress in the focal region and at the front of the electron shield. The thermal expansion and elasticity tensor is anisotropic and nonlinear, yet assumed isotropic and linear in Sections 2.2 and 6.3.

Adjusting the thermal expansion coefficient leads to an altered displacement field, leading to stronger expansion parallel to the C-axis, as compared to perpendicular to the C-axis, see Figure 3.3, elongating the current shape of the displacement field, see Figures 6.3e, 6.3f, 6.4e and 6.4f.

The implementation of an anisotropic elasticity tensor improves the prediction of stress concentrations of the modified region, however amorphization and void formation is neglected. The amorphization and void formation occurs at the focal region, where intensity is highest, leading to the strongest modifications [12,13].

Yet, at the edge of the plasma region thermal effects become more significant, therefore the anisotropic elasticity tensor is implemented to observe the stress response for anisotropic, crystalline sapphire. The elasticity tensor for a rhombohedral (trigonal-6) material, see Section 2.2, the elasticity tensor ($\boldsymbol{C}$) in Section 3.4 is modified to [65,66]:

$$\begin{bmatrix} C_{11} & C_{12} & C_{13} & C_{14} & 0 & 0 \\ C_{12} & C_{11} & C_{13} & -C_{14} & 0 & 0 \\ C_{13} & C_{13} & C_{33} & 0 & 0 & 0 \\ C_{14} & -C_{14} & 0 & C_{44} & 0 & 0 \\ 0 & 0 & 0 & 0 & C_{44} & C_{14} \\ 0 & 0 & 0 & 0 & C_{14} & C_{66} \end{bmatrix}, \tag{6.1}$$

where $C_{66} = \frac{1}{2}(C_{11} - C_{12})$, giving the values of the elasticity tensor in Table 6.1. C_{33} is the stiffness in axial direction, whereas the C_{11} components of the elasticity tensor describe distortion in radial direction. When neglecting C_{14} the material becomes transversely isotropic [67].

Table 6.1: Elasticity tensor component rhombohedral (trigonal-6) sapphire [66].

Symbol	Value	Unit
C_{11}	497	GPa
C_{12}	163	GPa
C_{13}	116	GPa
C_{33}	501	GPa
C_{14}	22	GPa
C_{44}	147	GPa

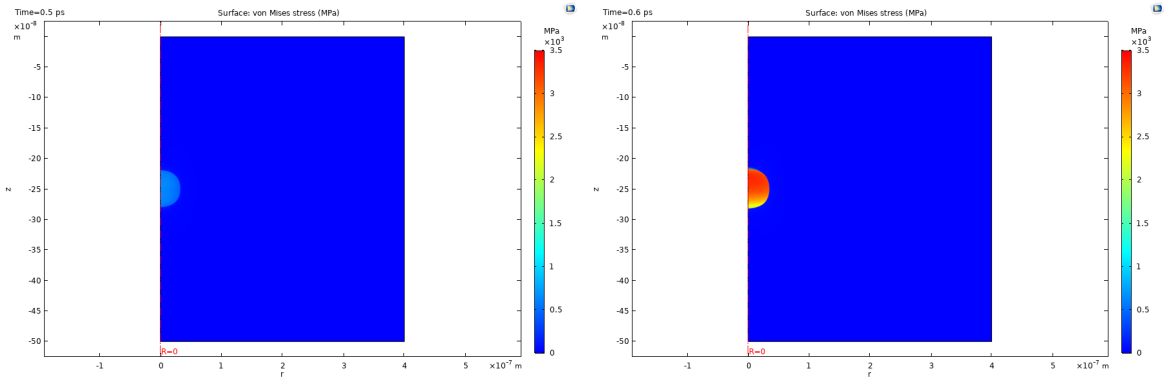

(a) $t = 0.5$[ps]. *(b)* $t = 0.6$[ps].

Figure 6.8: Von Mises stress (σ_v) in time, anisotropic, high energy pulse ($E_p = 0.05$[µJ]).

The displacement field for both 0.05[μJ] and 0.06[μJ] is identical due to unmodified thermal expansion coefficient. However, the anisotropic elasticity tensor leads to notable differences in the stress results, see Figures 6.8 and 6.9, where the maximum of the stress bar is $3.5 \cdot 10^3$[MPa] and $2.5 \cdot 10^4$[MPa] respectively.

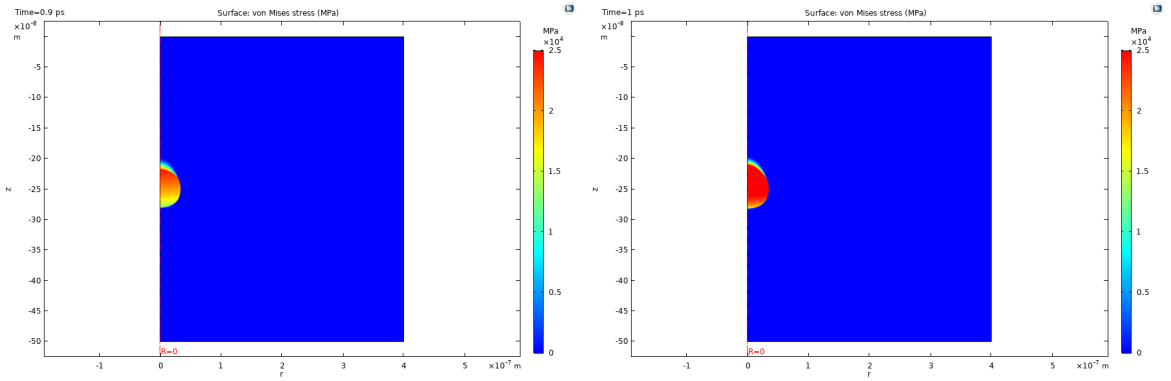

(a) $t = 0.9$[ps]. *(b)* $t = 1$[ps].

Figure 6.9: Von Mises stress (σ_v) in time, anisotropic, high energy pulse ($E_p = 0.05$[μJ]).

The stress observed, comparing to the isotropic material, is higher and uniformly distributed in the focal region. Due to electron shielding the shape of the stress distribution displaces in axial direction, yet is obscured by the existing stress in the focal region, see Figure 6.9. Similarly, for 0.06[μJ] the stress results are obscured and remain uniform, as the FWHM of the pulse is not completed, see Figure 6.10, therefore no notable effects are observed.

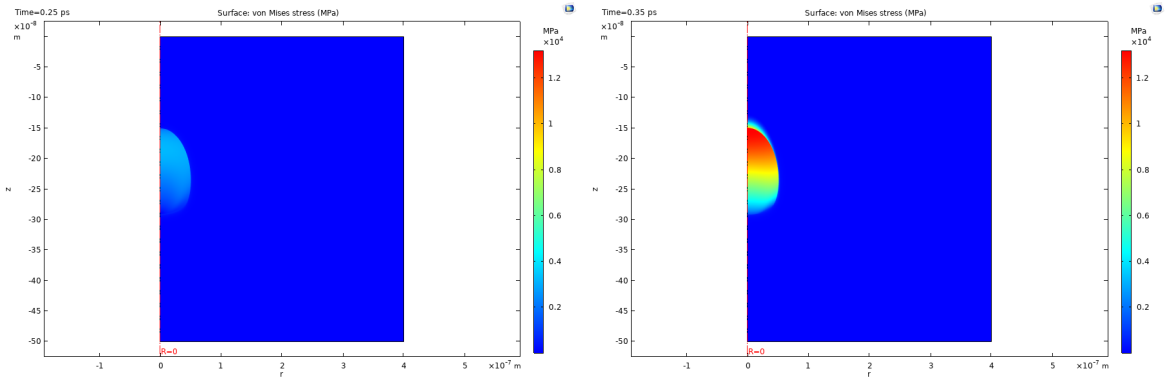

(a) $t = 0.25$[ps]. *(b)* $t = 0.35$[ps].

Figure 6.10: Von Mises stress (σ_v) in time, anisotropic, high energy pulse ($E_p = 0.06$[μJ]).

However, the effects of anisotropy become apparent when the FWHM of the pulse is completed, see Figure 6.11, where the maximum of the stress bar is $1.5 \cdot 10^5$[MPa]. Similarly to the isotropic case, see Figure 6.6, the stress concentrations are at the top of the electron shield and in the focal region, see Figures 6.11a and 6.11b.

Subsequently, see Figures 6.11c and 6.11d, unlike for isotropic material, the stress in the focal region reduces. Yet the stress in the electron shield increases significantly at two locations, see Figure 6.11e, at the top of the shield and at the bottom, away from the optical

axis. The stress concentrations at these locations coincide with experimental observations of crack formation, see Figures 1.2, 1.4 and 1.5.

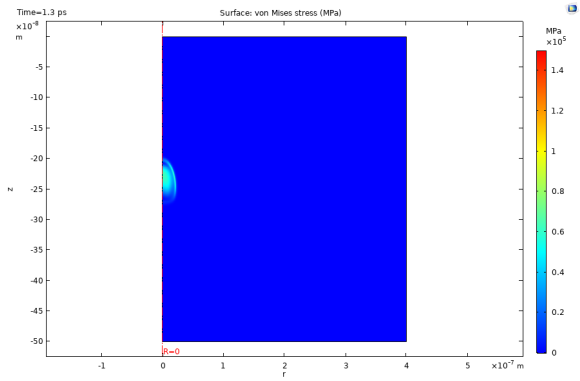

(a) $t = 1.3$[ps].

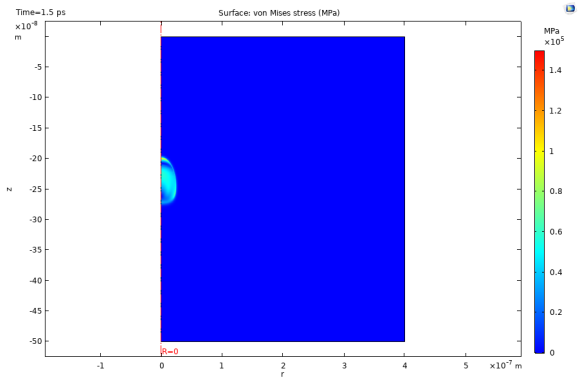

(b) $t = 1.5$[ps].

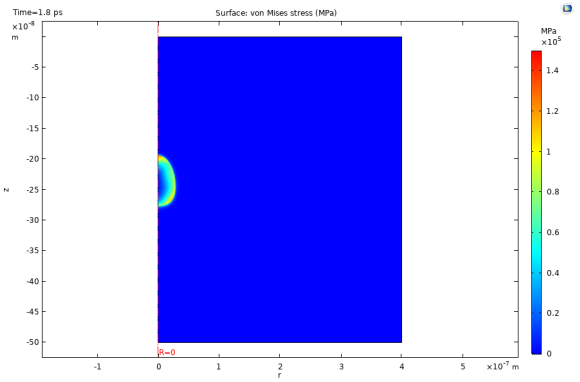

(c) $t = 1.8$[ps].

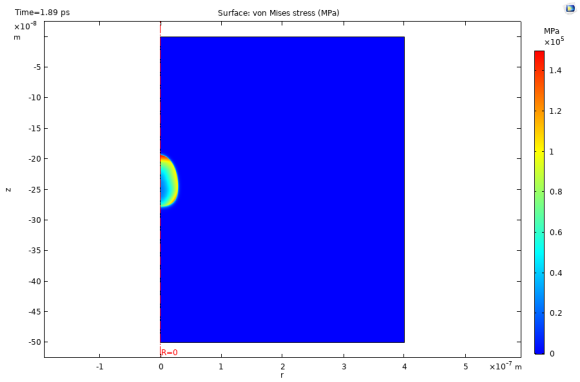

(d) $t = 1.9$[ps].

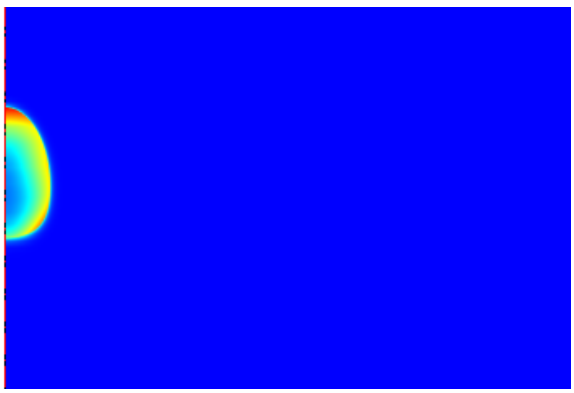

(e) $t = 1.9$[ps], detailed.

Figure 6.11: Von Mises stress (σ_v) in time, anisotropic, high energy pulse ($E_p = 0.05$[µJ]).

Despite the correlation between the observed stress concentrations in the model and experiments, the thermal stress only gives an initial insight into crack formation. The formation of cracks depends on a number of factors, e.g. pre-existing cracks and shock waves due to plasma formation [59,67].

Chapter 7

Conclusions and future work

7.1 Introduction

For each of the primary objectives: (1) to improve the existing model, (2) run several simulation scenarios of the improved model to understand model behaviour and (3) extend the model output by describing thermally induced stress; and the secondary objective, to resolve convergence issues, conclusions are drawn. The limitations of the improved model lead to a number of options, presented as future work.

7.2 Conclusions

The implementation of improvements was successful and resulted in a focusing laser beam profile at the focal point, able to describe the subsurface irradiation and subsequent interaction of phenomena. Furthermore, the boundary conditions implemented allow diffusion of heat into the bulk sapphire, reducing the lattice temperature.

The scenarios simulated in COMSOL Multiphysics®, using the improved model, shows a complex interaction of phenomena. The low pulse energy scenario results in minimal laser-induced heating of the material. This was expected, considering the transparency of sapphire for the wavelength and the low intensity is insufficient to initiate multiphoton ionization. For the high pulse energy, thanks to the improvements in the mesh and solver configurations, the performed studies maintained stability after the peak of the pulse ($t = 0$), unlike the base model. However, the studies did not converge at a later time instance, again large gradients affected model behaviour. The higher pulse energy studies extended beyond the domain, due to rapid plasma expansion, allowing for studying of post-processing effects.

The free electron density distribution is shaped by the intensity dependent Keldysh ionization framework, leading to local differences in density. The free electron absorption, including impact and avalanche ionization, dependent on the intensity and the local free electron density, leads to plasma formation and a subsequent shielding effect. The electron shield absorbs the incident pulse energy, leading to rapid free electron generation expanding the plasma region towards the top of the domain, displacing the electron shield. Thus, the importance of the free electron density distribution for laser processing sapphire is undeniable.

In addition to shield formation, the lattice temperature distribution trails the free electron density distribution due to the dependence of the electron-phonon coupling coefficient on the free electron density. The rapid expansion of the free electron temperature profile in the domain leads to an uniform free electron temperature distribution, where minimal local

differences and minimal energy diffuses into the bulk, due to the dependence on the free electron density. Yet, the connection between free electron density and free electron temperature is clear, the temperature is the total energy of the free electrons, when free electron recombination occurs the temperature increases, however the total energy remains the same. When all free electron have recombined the free electron temperature reduces rapidly, as the system returns to the initial free electron density. Clearly showing the strong influence of free electron density and negligible influence of free electron temperature on the lattice temperature.

The extension of the model, describing the temperature dependent displacement field and subsequent thermal stress, again shows significant dependence on the free electron density, as it determines the lattice temperature distribution. For low pulse energy the resultant stress is insignificant, yet displays the initial expansion in radial direction. For high and higher pulse energy plasma generation, expanding in the direction of the incident laser pulse, results in high free electron density at the electron shield, leading to large displacements in axial direction. The stress initially concentrates in the focal region, then after the electron shield is formed, it follows the electron density distribution and accumulates towards the top of the sample. After the peak of the pulse, the free electron density in the electron shield is maintained, raising the lattice temperature locally, subsequently leading to development of stress concentrations. Due to convergence issues, the determined stresses are occurring during processing. The implementation of an anisotropic elasticity tensor clearly shows that the stress during the FWHM of the pulse is obscured by the still increasing lattice temperature, whereas when the FWHM is completed the stress concentrations coincide with observed experimental results.

The improvements have provided an understanding of the model behaviour, the significance of each variable and individual phenomena. The thermal stress extension indicates agreement between modelling and experimental results, despite exclusion of other stress inducing effects.

7.3 Future work

Several limitations and model aspects are viable for further improvement:

Firstly, to improve ease of use of the model and allow for increase of complexity the computational capabilities require an upgrade, to reduce computational time, as the high pulse energy modelling time is over 72 hours. Furthermore, updating COMSOL Multiphysics® to the latest version gives additional options to model physics, better visualization and increased accuracy.

Secondly, the modelling domain needs to be extended, allowing for size comparison to experimental work. Comparing the simulation and experimental results determines the current degree of model accuracy of the shape of the plasma region, resulting in subsurface structures. Additionally, equivalent size requires processing parameters, i.e. pulse time and pulse energy, used in experimental work, leading to an accurate evaluation of the model accuracy.

Implementation of electromagnetic or wave optics is required, see Section 3.2, to describe relevant optical effects. First an analysis of linear optical effects, to describe light propagation in bulk sapphire, followed by an analysis of nonlinear optical effects, selecting effects relevant to determine the intensity distribution in the bulk and absorption of the pulse energy. Träger and Couairon et al. [68,69] could serve as guides to model pulse propagation,

however possible challenges for this approach could be the complexity of optical theory and the capabilities of COMSOL Multiphysics®.

Next, the priority should be given to the inclusion of plasma physics, as plasma is generated for high intensity pulses. Plasma has different properties from solid sapphire (see Xia et al. [70]), affects laser pulse propagation and subsequently the resultant subsurface structure as the amorphization and void formation occur in the plasma region. A simplified approach to model the effects within the plasma region would be to include additional loss terms in the free electron temperature PDE, attributed to plasma generation, amorphization and void formation.

Finally, implementation of nonlinear, anisotropic and variable dependent parameters to improve model behaviour, for determining the post-processing morphology. Inclusion of phase transformation through material parameters is an additional option.

References

[1] M. S. Akselrod and F. J. Bruni, "Modern trends in crystal growth and new applications of sapphire," *Journal of Crystal Growth*, vol. 360, no. 1, pp. 134–145, 2012.

[2] E. R. Dobrovinskaya, L. A. Lytvynov, and V. Pishchik, *Sapphire: Material, Manufacturing, Applications*. Springer-Verlag US, 2009.

[3] D. C. Harris, "A century of sapphire crystal growth: origin of the EFG method," *Optical Materials and Structures Technologies IV*, vol. 7425, pp. 215 – 226, 2009.

[4] G. M. Katyba, I. N. Dolganova, K. I. Zaytsev, and V. N. Kulrov, "Sapphire Single-Crystal Waveguides and Fibers for THz Frequency Range," *Journal of Surface Investigation*, vol. 14, no. 3, pp. 437–439, 2020.

[5] M. Manninen, H. Piili, and A. Salminen, "An overview of the conventional micro-processing and laser assisted techniques for fabricating microscale features," *ICALEO 2009 - 28th International Congress on Applications of Lasers and Electro-Optics, Congress Proceedings*, vol. 102, pp. 1458–1467, 2009.

[6] B. Jeong, H. Han, and C. Park, "Micro- and Nanopatterning of Halide Perovskites Where Crystal Engineering for Emerging Photoelectronics Meets Integrated Device Array Technology," *Advanced Materials*, vol. 32, no. 30, pp. 1–35, 2020.

[7] J. M. Quero, F. Perdigones, and C. Aracil, "Microfabrication technologies used for creating smart devices for industrial applications," *Smart Sensors and MEMS: Intelligent Sensing Devices and Microsystems for Industrial Applications*, pp. 291–311, 2018.

[8] A. Y. C. Nee, *Handbook of Manufacturing Engineering and Technology*. Springer-Verlag London, 2015.

[9] P. Boerner, M. Hajri, T. Wahl, J. Weixler, and K. Wegener, "Picosecond pulsed laser ablation of dielectric rods: Angle-dependent ablation process model for laser micromachining," *Journal of Applied Physics*, vol. 125, no. 23, p. 234902, 2019.

[10] M. Kumkar, M. Kaiser, J. Kleiner, D. Grossmann, D. Flamm, K. Bergner, and S. Nolte, "Ultrafast laser processing of transparent materials supported by in-situ diagnostics," *Laser Applications in Microelectronic and Optoelectronic Manufacturing (LAMOM) XXI*, vol. 9735, p. 97350P, March 2016.

[11] Y. Dogan and C. K. Madsen, "Optimization of ultrafast laser parameters for 3D micromachining of fused silica," *Optics and Laser Technology*, vol. 123, p. 105933, June 2019.

[12] L. Capuano, R. Pohl, R. M. Tiggelaar, J. W. Berenschot, J. G. E. Gardeniers, and G. R. B. E. Römer, "Morphology of single picosecond pulse subsurface laser-induced modifications of sapphire and subsequent selective etching," *Optics Express*, vol. 26, no. 22, p. 29283, 2018.

[13] S. Juodkazis, K. Nishimura, H. Misawa, T. Ebisui, R. Waki, S. Matsuo, and T. Okada, "Control over the crystalline state of sapphire," *Advanced Materials*, vol. 18, no. 11, pp. 1361–1364, 2006.

[14] M. Malinauskas, A. Žukauskas, S. Hasegawa, Y. Hayasaki, V. Mizeikis, R. Buividas, and S. Juodkazis, "Ultrafast laser processing of materials: From science to industry," *Light: Science and Applications*, vol. 5, no. 8, pp. 3–5, 2016.

[15] N. M. Bulgakova, V. P. Zhukov, Y. P. Meshcheryakov, L. Gemini, J. Brajer, D. Rostohar, and T. Mocek, "Pulsed laser modification of transparent dielectrics: what can be foreseen and predicted by numerical simulations?" *Journal of the Optical Society of America B*, vol. 31, no. 11, p. C8, 2014.

[16] S. K. Sundaram and E. Mazur, "Inducing and probing non-thermal transitions in semiconductors using femtosecond laser pulses," *Nature Materials*, vol. 1, no. 4, pp. 217–224, 2002.

[17] N. M. Bulgakova, I. M. Burakov, Y. P. Meshcheryakov, R. Stoian, A. Rosenfeld, and I. V. Hertel, "Theoretical models and qualitative interpretations of fs laser material processing," *Journal of Laser Micro Nanoengineering*, vol. 2, no. 1, pp. 76–86, 2007.

[18] N. M. Bulgakova, V. P. Zhukov, and Y. P. Meshcheryakov, "Theoretical treatments of ultrashort pulse laser processing of transparent materials: Toward understanding the volume nanograting formation and "quill" writing effect," *Applied Physics B: Lasers and Optics*, vol. 113, no. 3, pp. 437–449, 2013.

[19] K. I. Popov, C. McElcheran, K. Briggs, S. MacK, and L. Ramunno, "Morphology of femtosecond laser modification of bulk dielectrics," *2011 Conference on Lasers and Electro-Optics: Laser Science to Photonic Applications, CLEO 2011*, vol. 19, no. 1, pp. 271–282, 2011.

[20] P. C. Verburg, G. Römer, and A. J. Huis In 'T Veld, "Two-temperature model for pulsed-laser-induced subsurface modifications in Si," *Applied Physics A: Materials Science and Processing*, vol. 114, no. 4, pp. 1135–1143, 2014.

[21] L. Capuano, D. de Zeeuw, and G. Römer, "Towards a numerical model of picosecond laser-material interaction in bulk sapphire," *Journal of Laser Micro Nanoengineering*, vol. 13, no. 3, pp. 166–177, 2018.

[22] D. de Zeeuw, "Towards a model of pulsed laser material interaction in sapphire," Master's thesis, University of Twente, Enschede, the Netherlands, November 2017.

[23] C. Moon, S. Kanehira, M. Nishi, K. Miura, T. Nakaya, E. Tochigi, N. Shibata, Y. Ikuhara, and K. Hirao, "Crack propagation in a ruby single crystal by femtosecond laser irradiation," *Journal of the American Ceramic Society*, vol. 92, no. 12, pp. 3118–3121, 2009.

[24] COMSOL, *COMSOL Multiphysics® Reference Manual v. 5.3a*, accessed 2020. [Online]. Available: www.comsol.com

[25] Kyocera, *Sapphire | Fine Ceramics | (Advanced Ceramics) | Kyocera*, accessed Aug. 2020. [Online]. Available: https://global.kyocera.com/prdct/fc/list/material/sapphire/sapphire.html

[26] O. Svelto, *Principles of Lasers*. Springer Science, 1998.

[27] G. R. B. E. Römer, *Laser Material Processing*. University of Twente, Enschede, the Netherlands, 2018.

[28] R. Paschotta, *Field Guide to Laser Pulse Generation*. SPIE, 2009, vol. FG14.

[29] G. L. Squires, *Practical Physics*, 4th ed. Cambridge University Press, 2001.

[30] R. Paschotta, "Gaussian beams," accessed Sept. 2020. [Online]. Available: https://www.rp-photonics.com/gaussian_beams.html

[31] B. van Zeghbroeck, *Principles of Semiconductor Devices*. Prentice Hall PTR, 2007. [Online]. Available: https://ecee.colorado.edu/~bart/book/book/title.htm

[32] P. Balling and J. Schou, "Femtosecond-laser ablation dynamics of dielectrics: Basics and applications for thin films," *Reports on Progress in Physics*, vol. 76, no. 3, 2013.

[33] L. V. Keldysh, "Ionization in the field of a strong electromagnetic wave," *Soviet Journal of Experimental and Theoretical Physics*, vol. 20, no. 5, 1965.

[34] A. Vogel and V. Venugopalan, "Mechanisms of pulsed laser ablation of biological tissues," *Chemical Reviews*, vol. 103, pp. 577–644, March 2003.

[35] X. Jing, Y. Tian, J. Zhang, S. Chen, Y. Jin, J. Shao, and Z. Fan, "Modeling validity of femtosecond laser breakdown in wide bandgap dielectrics," *Applied Surface Science*, vol. 258, no. 10, pp. 4741–4749, 2012.

[36] B. Rethfeld, D. S. Ivanov, M. E. Garcia, and S. I. Anisimov, "Modelling ultrafast laser ablation," *Journal of Physics D: Applied Physics*, vol. 50, no. 19, p. 193001, 2017.

[37] M. Lundstrom, *Fundamentals of carrier transport*, 2nd ed. Cambridge University Press, 2000.

[38] B. E. A. Saleh and M. C. Teich, *Fundamentals of Photonics*. John Wiley & Sons, Inc., 2013, vol. 5.

[39] Y. H. Lee, *Introduction to Engineering Electro-magnetics*. Springer-Verlag, 2013.

[40] J. N. Damask, *Polarization optics in telecommunications*. Springer, 2004.

[41] A. E. Siegman, *Lasers*. Mill Valley, California, 1986.

[42] R. Paschotta, "Gouy phase shift," accessed Sept. 2020. [Online]. Available: https://www.rp-photonics.com/gouy_phase_shift.html

[43] L. C. Andrews and R. L. Phillips, *Laser Beam Propagation through Random Media*, 2nd ed. SPIE - The International Society for Optical Engineering, 2005.

[44] P. Farrell, N. Rotundo, D. H. Doan, M. Kartner, J. Fuhrmann, and T. Koprucki, *Handbook of Optoelectronic Device Modeling and Simulation: Drift-Diffusion Models*, 1st ed. CRC Press, 2017.

[45] B. Raftari, N. Budko, and K. Vuik, "A modified and calibrated drift-diffusion-reaction model for time-domain analysis of charging phenomena in electron-beam irradiated insulators," *AIP Advances*, vol. 8, no. 1, 2018.

[46] J. B. J. Fourier, *The Analytical Theory of Heat*, ser. Cambridge Library Collection - Mathematics, A. Freeman, Ed. Cambridge University Press, 2009.

[47] R. B. Hetnarski and M. R. Eslami, *Thermal Stresses – Advanced Theory and Applications*, ser. Solid Mechanics and its Applications. Springer, 2009.

[48] M. Nesser, O. Maloberti, J. Dupuy, E. Salloum, S. Panier, J. Fortin, and P. Dassonvalle, "Correlation between laser energetic parameters and magnetic properties of GO laminations under surface treatments with long, short or ultra-short pulsed lasers," *Journal of Magnetism and Magnetic Materials*, vol. 504, September 2019.

[49] A. K. Harman, S. Ninomiya, and S. Adachi, "Optical constants of sapphire (α-Al2O3) single crystals," *Journal of Applied Physics*, vol. 76, no. 12, pp. 8032–8036, 1994.

[50] M. Eldlio, F. Che, and M. Cada, "Drude-Lorentz model of semiconductor optical plasmons," *Lecture Notes in Electrical Engineering*, vol. 247 LNEE, pp. 41–49, 2014.

[51] I. F. Almog, M. S. Bradley, and V. Bulovi, "The Lorentz Oscillator and its Applications," *Lecture notes*, pp. 1–34, 2011.

[52] O. Ratiba, M. Kadi, A. Smaali-Lafane, and R. Outemzabet, "Analysis of optical and related properties of tin oxide thin films determined by Drude-Lorentz model," *Surface and Coatings Technology*, vol. 211, pp. 45–49, October 2012.

[53] S. I. Azzam and A. V. Kildishev, "Time-domain dynamics of saturation of absorption using multilevel atomic systems," *Optical Materials Express*, vol. 8, no. 12, p. 3829, 2018.

[54] A. S. Rao, "Nonlinear spectroscopy of three-level cascade systems in the act of saturable and reverse saturable absorption," *Optik*, vol. 185, no. March, pp. 14–19, 2019.

[55] Y. J. Zhang, Y. Z. Song, and C. K. Wang, "Variation of two-photon absorption cross sections and optical limiting of compounds induced by static electric field," *Chinese Journal of Chemical Physics*, vol. 27, no. 3, pp. 259–264, 2014.

[56] F. J. Duarte, *Chapter 3 - The Uncertainty Principle in Optics*. Academic Press, 2003.

[57] "MUMPS: A parallel sparse direct solver," accessed Aug. 2020. [Online]. Available: http://mumps.enseeiht.fr/

[58] N. M. Bulgakova, R. Stoian, A. Rosenfeld, I. V. Hertel, and E. E. B. Campbell, "Electronic transport and consequences for material removal in ultrafast pulsed laser ablation of materials," *Phys. Rev. B*, vol. 69, p. 054102, February 2004.

[59] K. Pallav, I. Saxena, and K. F. Ehmann, "Laser-induced plasma micromachining process: Principles and performance," *Journal of Micro and Nano-Manufacturing*, vol. 3, no. 3, pp. 1–8, 2015.

[60] M. Wang, W. Mei, and Y. Wang, "Simulation of femtosecond laser ablation sapphire based on free electron density," *Optics and Laser Technology*, vol. 113, no. September 2018, pp. 123–128, 2019.

[61] D. Puerto, J. Siegel, W. Gawelda, M. Galvan-Sosa, L. Ehrentraut, J. Bonse, and J. Solis, "Dynamics of plasma formation, relaxation, and topography modification induced by femtosecond laser pulses in crystalline and amorphous dielectrics," *Journal of the Optical Society of America B*, vol. 27, no. 5, p. 1065, 2010.

[62] X. Jia and X. Zhao, "Numerical investigation of ultrashort laser interaction with dielectric materials based on a plasma-temperature combined model," *Journal of Manufacturing Processes*, vol. 28, pp. 508–514, 2017.

[63] R. Brenner, R. A. Lebensohn, and O. Castelnau, "Elastic anisotropy and yield surface estimates of polycrystals," *International Journal of Solids and Structures*, vol. 46, no. 16, pp. 3018–3026, 2009.

[64] J. D. Clayton, *Nonlinear Elastic and Inelastic Models for Shock Compression of Crystalline Solids*. Springer International Publishing, 2019.

[65] J. M. Winey, Y. M. Gupta, and D. E. Hare, "R-Axis Sound Speed and Elastic Properties of Sapphire Single Crystals," *Journal of Applied Physics*, vol. 90, no. 6, pp. 3109–3111, 2001.

[66] M. Grundmann, "Elastic theory of pseudomorphic monoclinic and rhombohedral heterostructures," *Journal of Applied Physics*, vol. 124, no. 18, pp. 0–10, 2018.

[67] T. Vodenitcharova, L. C. Zhang, I. Zarudi, Y. Yin, H. Domyo, T. Ho, and M. Sato, "The effect of anisotropy on the deformation and fracture of sapphire wafers subjected to thermal shocks," *Journal of Materials Processing Technology*, vol. 194, no. 1-3, pp. 52–62, 2007.

[68] F. Träger, *Springer Handbook of Lasers and Optics*, ser. Springer Handbooks. Springer Berlin Heidelberg, 2012.

[69] A. Couairon, E. Brambilla, T. Corti, D. Majus, O. De, and M. Kolesik, "Practitioner's guide to laser pulse propagation models and simulation," *European Physical Journal: Special Topics*, vol. 199, no. 1, pp. 5–76, 2011.

[70] X. Xia, Z. Qin, B. Xu, and Z. Cai, "Dielectric constant and laser beam propagation in an underdense collisional plasma: Effects of electron temperature," *Physica Scripta*, vol. 84, no. 1, 2011.